AD-A172 005 APPLICATION OF NONDESTRUCTIVE TESTING TECHNIQUES TO MATERIALS TESTING(U) STANFORD UNIV CA EDWARD L GINZTON LAB OF PHYSICS G S KINO FEB 86 AFOSR-TR-86-0635 1/1

UNCLASSIFIED AFOSR-84-0063 F/G 14/2 NL

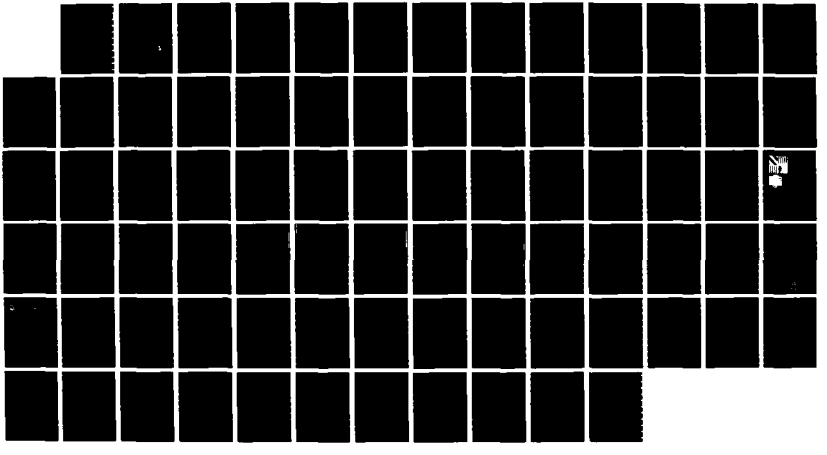

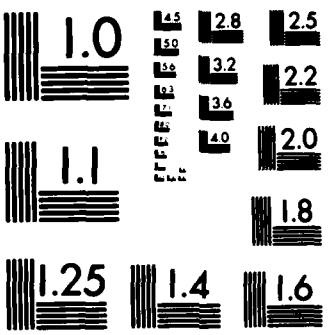

MICROCOPY RESOLUTION TEST CHART

SECURITY CLASSIFICATION OF THIS PAGE (When Data Entered)

REPORT DOCUMENTATION PAGE

READ INSTRUCTIONS BEFORE COMPLETING FORM

1. REPORT NUMBER: AFOSR-TR- 86-0635
2. GOVT ACCESSION NO.
3. RECIPIENT'S CATALOG NUMBER

4. TITLE (and Subtitle): "APPLICATION OF NONDESTRUCTIVE TESTING TECHNIQUES TO MATERIALS TESTING"
5. TYPE OF REPORT & PERIOD COVERED: ANNUAL, 01JAN85 - 31DEC85
6. PERFORMING ORG. REPORT NUMBER

7. AUTHOR(s): G.S. KINO
8. CONTRACT OR GRANT NUMBER(s): AFOSR-84-0063

9. PERFORMING ORGANIZATION NAME AND ADDRESS:
STANFORD UNIVERSITY
EDWARD L. GINTZON LAB, W.W. HANSEN LAB OF PHYSICS
STANFORD CA 94305
10. PROGRAM ELEMENT, PROJECT, TASK AREA & WORK UNIT NUMBERS: 61102F 2306/A2

11. CONTROLLING OFFICE NAME AND ADDRESS: AFOSR
12. REPORT DATE: Feb 1986
13. NUMBER OF PAGES

14. MONITORING AGENCY NAME & ADDRESS(if different from Controlling Office):
AFOSR/NE
Bolling AFB DC 20332-6448
15. SECURITY CLASS. (of this report): Unclassified
15a. DECLASSIFICATION/DOWNGRADING SCHEDULE

16. DISTRIBUTION STATEMENT (of this Report):
Approved for public release; distribution unlimited.

17. DISTRIBUTION STATEMENT (of the abstract entered in Block 20, if different from Report)

18. SUPPLEMENTARY NOTES

DTIC ELECTE SEP 17 1986 A

19. KEY WORDS (Continue on reverse side if necessary and identify by block number)

20. ABSTRACT (Continue on reverse side if necessary and identify by block number)

A range of fundamentally new optical nondestructive techniques has been demonstrated for measurements of surface defects, range, surface profiles and acoustic and thermal displacements of a surface. A wide aperture acoustic beam has been demonstrated to measure range to a far greater accuracy than with conventional NDT systems using short pulses. The range resolution of such a lens is comparable to a wavelength while that for a short pulse system is, at best, two or three wavelengths. Optical methods, developed during the program, have been successful in measuring film thicknesses to an accuracy of an order of 200A.

DD FORM 1 NOV 65 IS OBSOLETE

U/C

SECURITY CLASSIFICATION OF THIS PAGE (When Data Entered)

AD-A172 005

DTIC FILE COPY

AFOSR.TR. 86-0635

AFOSR-84-0063

Interim Scientific Report

to

AIR FORCE OFFICE OF SCIENTIFIC RESEARCH

for a program of research

entitled

APPLICATION OF NONDESTRUCTIVE TESTING TECHNIQUES TO MATERIALS TESTING

for the Period of
~~August 1, 1985~~ Jan01 85 through ~~January 31, 1986~~ DEC 31, 85

February 1986

Principal Investigator:
G. S. Kino

Approved for public release;
distribution unlimited.

Edward L. Ginzton Laboratory
W. W. Hansen Laboratories of Physics
Stanford University
Stanford, California 94305

TABLE OF CONTENTS

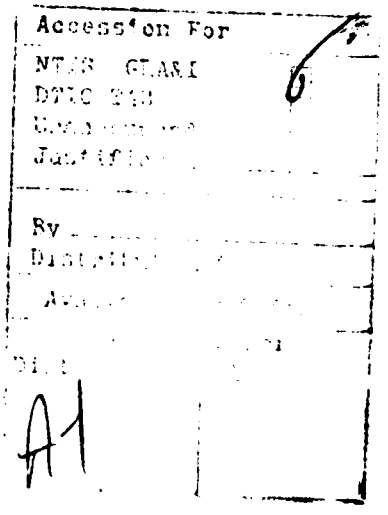

APPLICATION OF NONDESTRUCTIVE TESTING TECHNIQUES TO MATERIALS TESTING

G. S. Kino

INTRODUCTION

During the last year, we have demonstrated a range of fundamentally new optical nondestructive techniques for measurements of surface defects, range, surface profiles, and acoustic and thermal displacements of a surface. We believe that these will be of great importance both for nondestructive testing and for manufacturing technology.

During our initial research on this contract on the scanning acoustic microscope, we developed several new quantitative measurement techniques. We have now shown these same techniques can be applied to optical microscopy and to optical range sensing. Much to our surprise, coherent optics has not been used in this way before. We have therefore decided to exploit the advantages of optics, its relative insensitivity to environmental conditions, its very good resolution, and no contact with the sample. We also plan to develop a new range of tools for range sensing, profile measurements, flaw detection, and nondestructive testing where the optical probe is used as a thermal wave or acoustic wave sensor.

In our acoustic microscope work, we have demonstrated that, by using a wide aperture acoustic beam, we can measure range to a far better accuracy than with conventional NDT systems using short pulses. The range resolution of such a wide aperture scanning microscope lens is comparable to a wavelength; the range resolution of a short pulse system is, at best, two or three wavelengths. This fundamental breakthrough made it possible, in the work of

Khuri-Yakub,* to measure the properties of near-surface flaws without interference from surface reflections. Khuri-Yakub has exploited these techniques for NDT of composites and of near surface flaws in metals, glass, and ceramics.

Normally, optical systems do not give very good range resolution, but the use of this same phenomenon has made it possible to develop new optical microscopy tools for measuring the thickness of thin films. Since we can also measure amplitude and phase of such coherent waves, we can in fact measure the distance of a surface from the lens with accuracies of the order of .001 λ . In our acoustic microscope work, operating at a wavelength of 30 μm , we were able to measure film thicknesses to an accuracy of an order of 200 A . In our optical microscope work, working at a wavelength of 5100 A , we are able to measure film thicknesses to an accuracy of a few Angstroms.

These basic developments have led to a seed program supported by SIMA, the Stanford Institute for Manufacturing and Automation, for measurements on a much larger scale. We have demonstrated a range sensor for robotics with a range accuracy of the order of 0.5 mm at 20 cm , and another type of more accurate range sensor with accuracies of the order of a few microns at distances of 10-20 cm . This latter type of range sensor should be of great importance in applications to precision machining. We now envisage the possibility of carrying out measurements with the accuracy of a high-quality micrometer by using noncontacting, nondestructive optical methods. Furthermore, the fundamental tools that we are developing will not only enable us to measure range directly, but also to measure such parameters as the slope of a

*P. Reinholdtsen and B. T. Khuri-Yakub, "The Effects of Surface Roughness on Subsurface Defect Detection Using Acoustic Microscopy," Presented at the DARPA/AF Review of Progress in Quantitative NDE, Williamsburg, VA (July 1985).

surface, surface roughness, and surface curvature, all without making contact with the sample.

A few examples may point out the importance of these possible breakthroughs in nondestructive testing technology. Consider the problem of measuring the inside of an engine cylinder during manufacture and at a later stage when testing it in the field. We envisage making optical measurements of the cylinder radius, how much out of round it is, its surface finish, and whether there are flaws in the surface. We also envisage carrying out measurements during the machining process itself without touching the object. The same technique could also be used to make profile measurements of large structures like an automobile or a complicated engine component. On the other hand, this kind of profiling measurement can be made on a small scale on semiconductors and integrated circuits.

Most of our concentration in this work has been on techniques suitable for measuring small electronic components, precision mirrors, or magnetic recording disks. The basic principles we are developing, however, apply both to small and large structures, and we have carried out enough demonstrations to show that the principles are universal.

We use laser sources for the purpose because of their high intensity. In many of the techniques we have developed, however, incoherent light of high enough intensity would do as well. The implication of this statement is that the surfaces we are looking at need not be mirror smooth. In the larger scale applications, the techniques should work with machined surfaces and materials which are not necessarily lapped to a fine finish. We have made basic demonstrations to show that these conclusions are valid.

Thus, in this work, we are developing a range of new techniques based on our original work with the acoustic microscope, which have now proven to be

very useful in optical applications. In these applications, we can measure range, curvature, electronic properties, and material properties, and we can scan an optical beam at will. The mere fact that we can scan the optical beam and produce many optical spots at once also leads to possible new techniques for photolithography and for semiconductor processing with optical beams. The range of possible applications is very large, but they are based on the development, in every case, of nondestructive techniques which do not need any contact with the sample and which can be used at high speed.

We believe that these techniques are major breakthroughs in the field of nondestructive testing.

ACOUSTIC MICROSCOPY

This work is now finished. Three papers published on the work are given as Appendix I (332,333 C-H paper) in this report. They describe the results that we obtained.

There were two basic developments in this research. The first was, for the first time, to measure both the amplitude and phase of the received signal in an acoustic microscope. Since we could measure phase to a tenth of a degree, this made it possible to measure heights to an accuracy of a few thousandths of a wavelength. Thus, we were able to measure film thicknesses to accuracies of the order of 200 Å using an acoustic wavelength of 30 μm in water. More important still, for the first time we were able to make stress measurements in glass samples with a resolution of the order of one or two millimeters over the surface of a tempered glass sample. This technique may prove to be of great importance for measuring near-surface stress variations in ceramics and other materials in which there are inhomogeneities present.

The second major development was based on the use of the so-called V(z) measurement. As the lens of an acoustic microscope is moved towards the sample being examined, the focus moves from the point above the surface of the substrate to a virtual point below the surface. If the distance from the surface to the focus is called z , the return signal amplitude at the detector is called V(z) . If we plot V(z) as a function of z , we typically obtain a quasi-periodic curve with the distance between minima dependent on the Rayleigh wave velocity of waves along the surface of the substrate. We developed a theory which showed: (1) the relation between V(z) and the reflectivity of the sample as a function of angle of incidence of a plane wave, and (2) that the V(z) plot could be inverted to determine the reflection function of a plane wave from a surface.

These results made it possible to use an acoustic microscope to directly measure not only the surface wave velocity, but the shear wave and longitudinal wave velocities of waves along the surface. Thus, we could use the microscope to investigate the material properties in a small region and put the results on a quantitative basis. The theory and experiments were in excellent agreement.

The results were very well received by the acoustic microscope community, for this was the first demonstration that a complete inversion of the V(z) plots could be obtained. Now the theory is being further developed for use with optical microscopy and range sensing.

OPTICAL MEASUREMENTS

Introduction

The scanning acoustic microscope used coherent acoustic waves to produce images free of speckle, and is capable of quantitative phase and amplitude measurements. These results have led us to investigate how these techniques

might be employed in optics. Interestingly enough, quantitative optical measurement techniques of this type have not been carried out before. The optical projects on this contract have therefore been aimed at investigating how we could improve optical systems by employing modern electronic techniques within the optical system. Our purpose has been to make accurate profile measurements with better transverse resolution than is presently obtainable with the optical microscope, and to make quantitative measurements of height rather than just produce a qualitative phase contrast image.

We demonstrated an electronically-scanned optical microscope which could, for the first time, measure both optical phase and amplitude simultaneously. We used these results to obtain vertical resolutions of the order of 10 Å or better and profiles with a transverse resolution of 0.27 μm . Because we had optical phase and amplitude information available, we were able to demonstrate that, by Fourier transform processing, we could improve the transverse resolution to 0.13 μm .

These results were an important breakthrough because improvement in the resolution of the optical microscope and its accuracy for quantitative measurements are badly needed for measuring small components, such as those used in electronics. They are also needed for precision machining applications, such as the machining of optical mirrors and the determination of small surface defects in a wide range of precision machined parts.

With these early results in hand, we were then able to go on and incorporate other electronic components in an optical system which could be used for optical range sensing, for slope measurements, and for edge measurements. It would also be feasible to use the system for measurements of curvature and other parameters. Later, we realized that the basic ideas here were much broader than just their applications to microscopy. For the first time, we

could produce a simple optical range sensor for robotics. We could also use these techniques to carry out nondestructive measurements of machined parts during and after manufacture and to determine the presence of imperfections. In the next two sections, we will describe some of these results and point out their importance to nondestructive testing and to manufacturing technology.

Range Sensor

We are developing two types of type II scanning optical microscopes. The first mechanically scans the object or the lens, the second uses electronic scanning and direct phase and amplitude measurements of the optical signal.

The purpose of the first system is to develop and demonstrate a number of new types of measurement techniques which should enable us to measure range, film thicknesses of films a few wavelengths thick, profiles of films and structures, surface roughness and slope, and the curvature of a surface. We belive that, at a later stage, these techniques will enable us to measure the presence and size of dust particles, internal material properties of transparent materials, and the presence and size of surface and near-surface defects, such as cracks and dislocations.

The system we have set up is illustrated in Fig. 1. A laser illuminates a microscope objective lens with a collimated beam. The collimated beam is obtained by expanding the laser beam in a telescope and passing it through a hole in a diaphragm. The beam is focused to a point by the microscope objective lens and an image of the point illuminated on the object is imaged through a further microscope objective lens onto a pinhole. A detector is placed behind the pinhole. The object can be scanned in all directions, and scans of the output can be passed into a computer. At the present time, line scans in any direction can be obtained. A Bragg cell can be placed in the path to amplitude modulate or deflect the beam, as illustrated in Fig. 1.

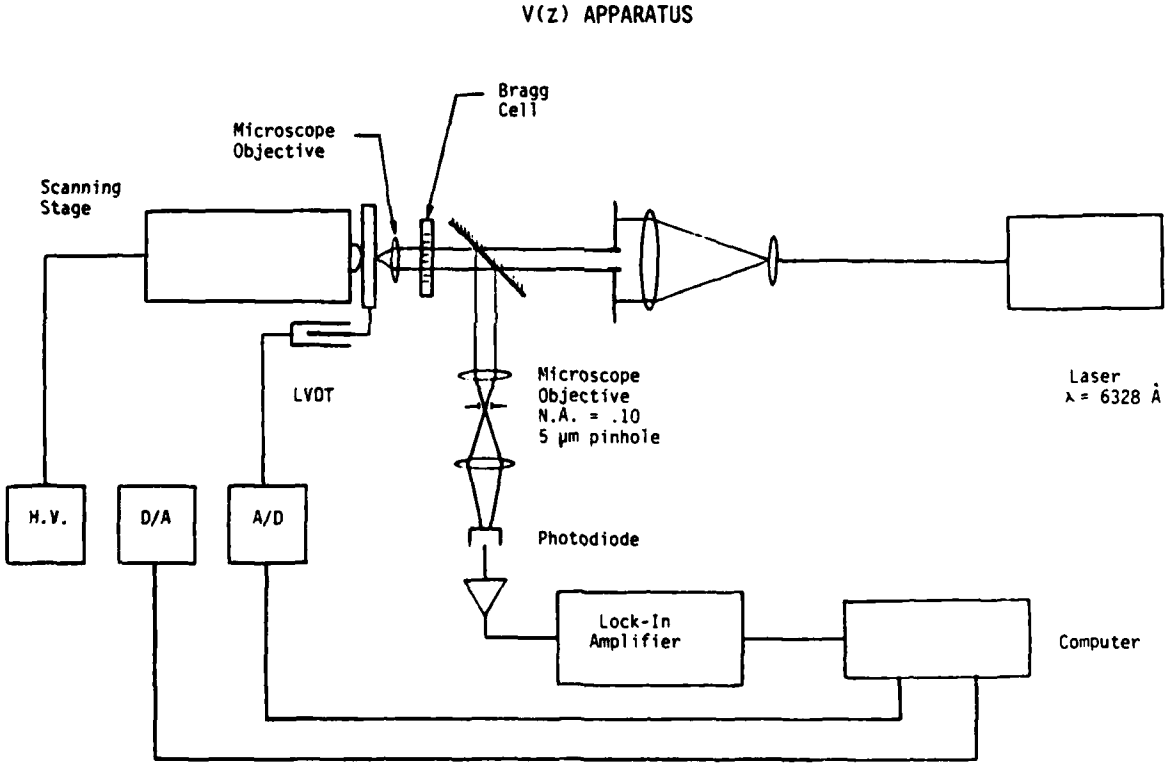

Fig. 1. Mechanically-scanned optical microscope used for optical depth profiling, or V(z) .

In this system, we can insert various electronically-controlled components. At the present time, we have used a Bragg cell to give partial electronic scanning and for phase contrast imaging. We have employed a new type of electronically-controllable phase contrast Zernike system. In addition, we have moved the object up and down periodically with a ceramic transducer to give an rf output at the detector, and we have tried out the concepts with a flexible, electronically-controllable mirror to obtain the position of the focus with extreme accuracy.

Optical Range Sensor

The basic principle of the type II microscope is shown in Fig. 2. Light is passed through a pinhole through the objective lens to the reflecting object. An image of the pinhole is obtained on the reflecting object; this image is in turn imaged back on the pinhole and a detector is placed behind the pinhole. If the reflecting plane is at the focus, a well-focused image is obtained at the pinhole and a strong signal is obtained at the detector. If the reflecting plane is displaced, a defocused image is obtained at the pinhole, and relatively little light passes through it. Thus, a strong maximum output is obtained at the detector when the beam is focused on the reflecting plane.

The system is therefore capable of very good range resolution and does not need a sharp edge to obtain the range resolution as does a self-focusing camera. This system is an analog to the scanning acoustic microscope which uses a coherent detector in the back focal plane of the lens. We have developed a nonparaxial theory of this measurement and have shown that the range resolution of the system is

$$d_z(3\ \mathrm{dB}) = \frac{0.45\ \lambda}{1 - \cos\ \theta_0}$$

OPTICAL RANGE SENSORS

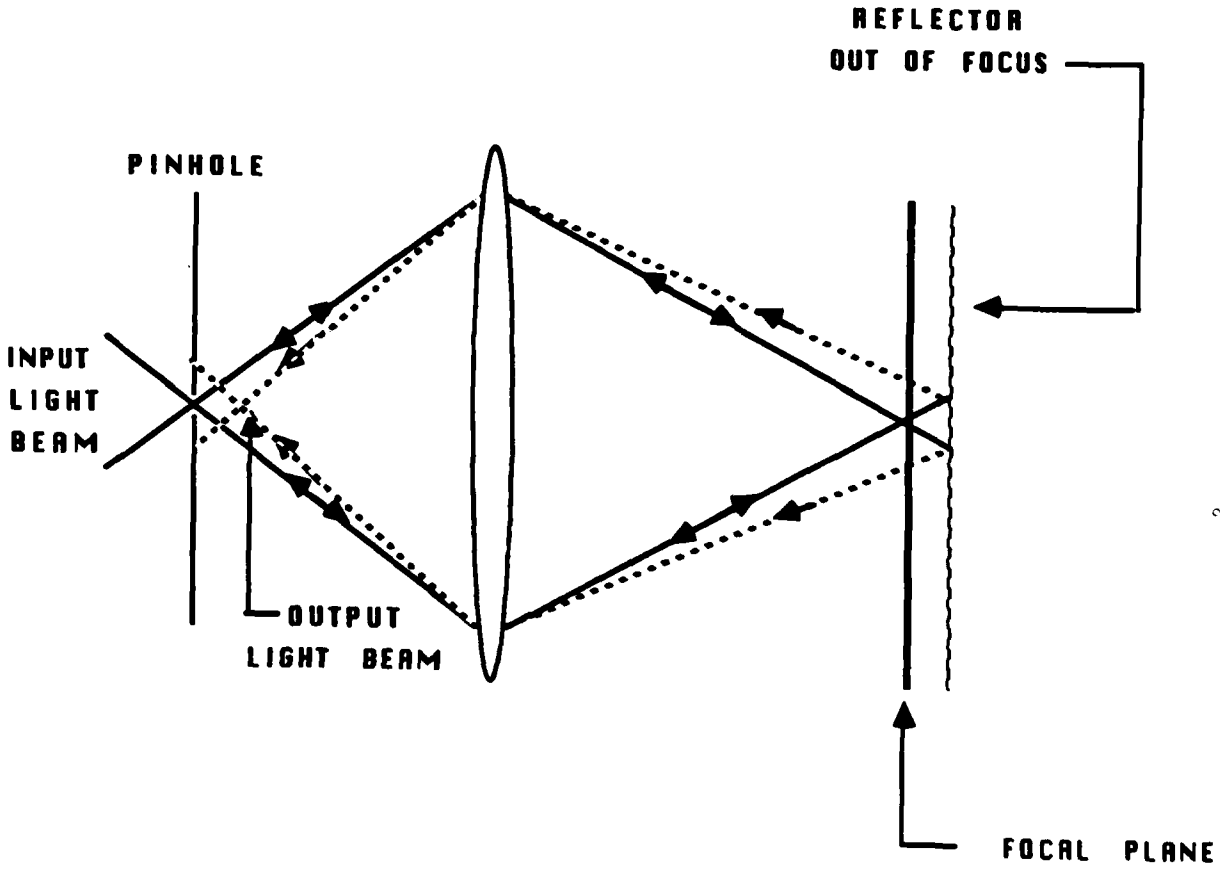

Fig. 2. A diagram illustrating the range definition of a type II microscope.

where θ_0 is the half-angle of the aperture of the lens. The nonparaxial theory which we have developed implies 3 dB range resolutions of the order of .7 μm with a 5100 Å argon beam. Results obtained with this system are shown in Fig. 3. The comparison between theory and experiment is excellent. The theory which we have developed is given in the papers in the appendix. Recently, we have begun to develop the theory for polarized optical waves, and we are beginning to take account of aberrations in thin films.

The advantage of this type of range sensor is that it can be used over a fairly large range by placing the system in a feedback circuit so that the lens can be moved mechanically to follow the surface of the object. This requires detecting where the maximum amplitude occurs, but it would be better and more accurate to look for a zero. We have done this in a demonstration experiment by vibrating the object back and forth at a frequency Ω with a piezoelectric pusher. An rf signal at frequency Ω is obtained at the detector. This signal is zero when the dc output is maximum, i.e., we obtain a differential of the output signal. We have developed the theory to show that with a wide aperture lens, we should be able to measure the position of the surface to an accuracy of .001 Å with a measurement time of the order of 1 msec . We appear to be within a factor of ten of this accuracy, and are encouraged by the early results. An illustration of this type of differential measurement is given in Fig. 4. There is a sharp minimum in the ac output, as shown in the lower figure. We are also beginning to develop the technique to measure the thickness of thin films. In this case, we observe a maximum when the focus is placed on the top surface and the lower surface of a transparent thin film. Early results on a ZnO film, 1.6 μm thick, confirm the basic ideas. We are now developing the theory to account for the aberrations of the

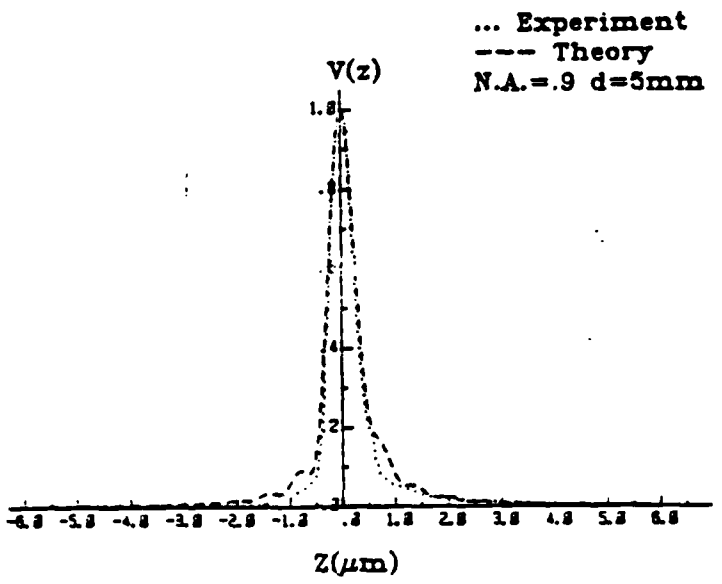

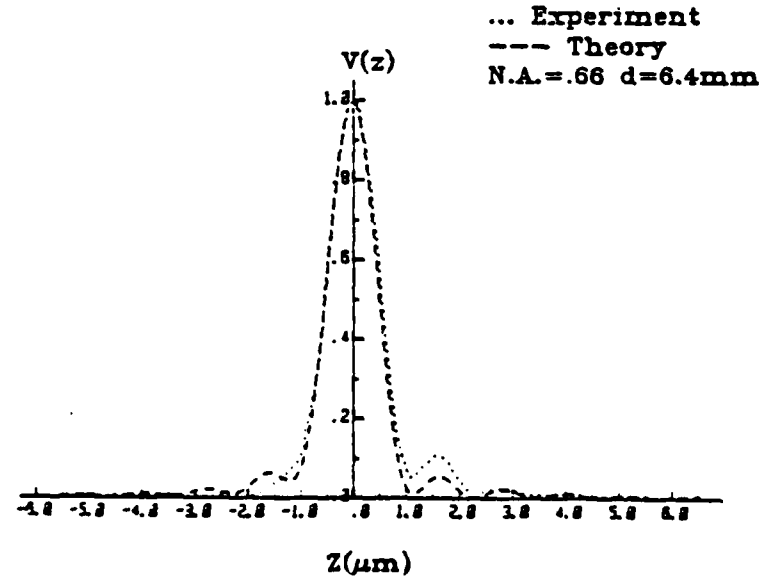

Fig. 3. Plots of the output signal V(z) as a function of z , the distance from the focus of a reflecting plane mirror in a type II scanning microscope. The top figure has a numerical aperture of 0.9 ; the lower figure has a numerical aperture of 0.66 .

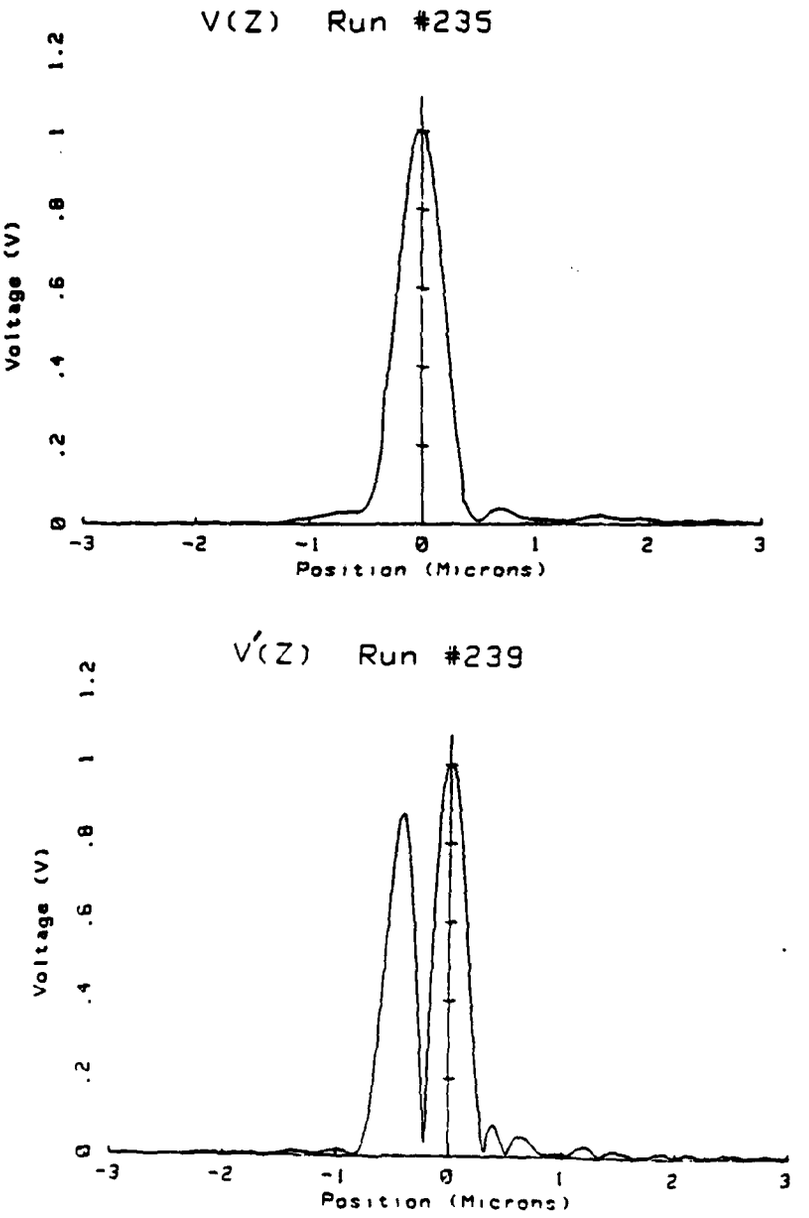

Fig. 4. Differential measurement V'(z) of V(z) curve.

optical system when a wide-angle beam passes into a thin film. So far, the results, theory, and experiments appear to be within a few percent. We are further working on the theory to take account of aberrations and to eliminate errors.

The same basic idea applies to range sensing at large distances. On another project, not supported on this contract, we have tried out these ideas for measuring range at distances of the order of 20 cm . They appear to work well. One of the questions that arises there is whether the same techniques can be used on rough surfaces, such as machined surfaces. It was convenient to test the principles in the microscope. We did this with a deliberately roughened surface. Fig. 5 shows the V(z) curve from a surface roughened with 5 μm grit. The surface was tilted at an angle of 5° in a plane normal to the z-axis of the system. This tilt was sufficient to assure that no directly reflected wave re-entered the optical system.

Clearly, the V(z) behavior in specular reflection is identical to the coherent reflection from the mirror, although the amplitude is 66 dB down. This curve also illustrates the very high signal-to-noise ratio of this technique, approximately 90 dB .

The results illustrate that the basic technique is applicable to rough surfaces because we are imaging only one point on a surface at a time. We have worked out the theory on this subject which predicts the decrease in amplitude from a perfectly random surface. Our results appear to be in fairly good agreement with this theory.

We would prefer, of course, to vary the focal position of the beam on an rf basis rather than use a vibrating object. We are presently examining two techniques for this purpose. The first involves a variable Zernike phase plate placed in the optical path (Fig. 6). The system is different from a

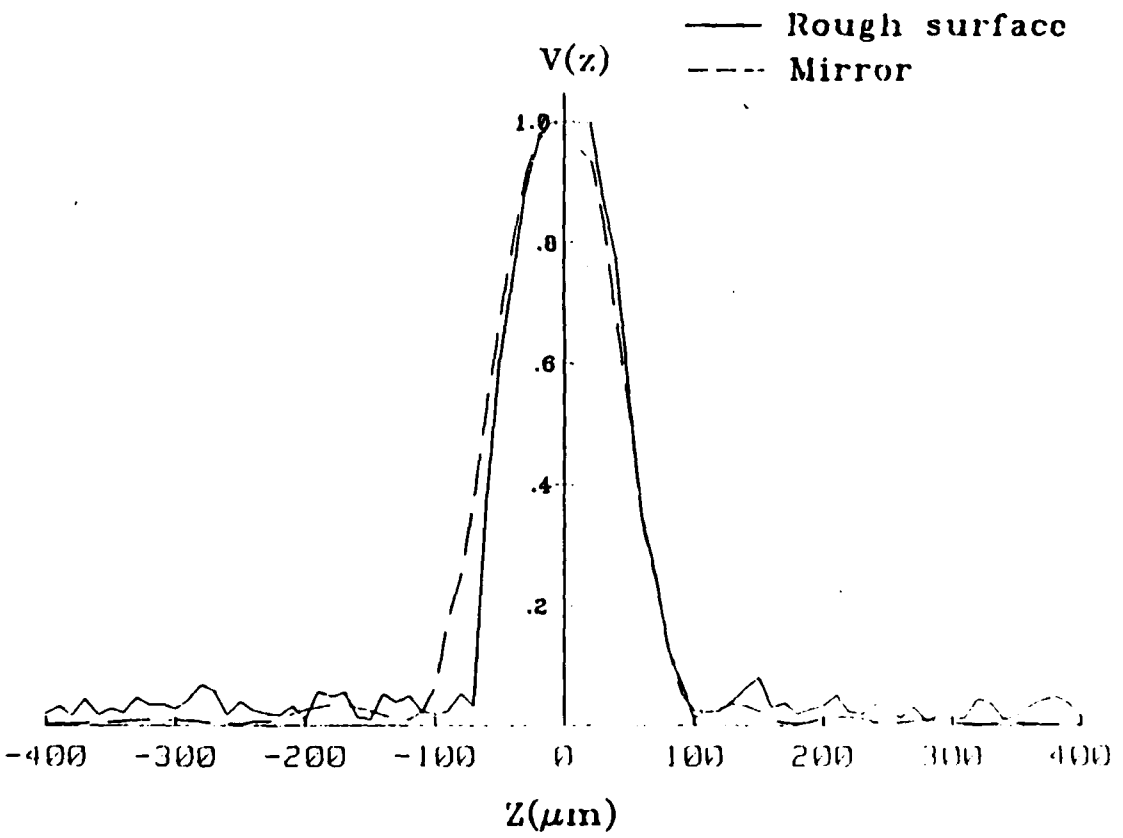

Fig. 5. V(z) response of a roughened surface tilted at an angle.

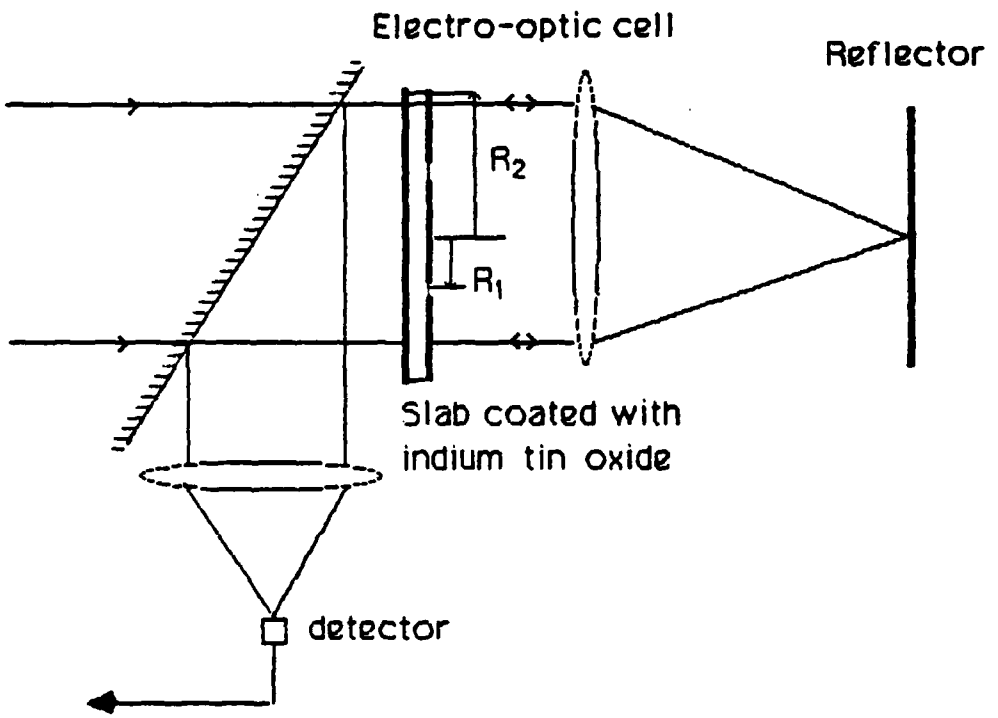

Fig. 6. Phase contrast system.

conventional phase contrast microscope because it gives an rf signal output which is directly proportional to phase change with a sign that reverses with phase, and is zero for zero phase change. We have also shown that it has much better transverse resolution. The phase plate is constructed on transparent PLZT ceramic. When a voltage is applied to the transparent electrodes on the plate, the phase of the optical beam passing through it is changed. If the plate is divided into two parts, the phase of the central portion of the beam can be varied relative to the outer portion. If the phase plate itself is placed in the back focal plane of the lens, as illustrated in Fig. 6, the output of the detector is of the form

$$\cos(\phi_0 + A \cos \Omega t)$$

where A is proportional to the amplitude of the voltage applied to the center electrode at a frequency Ω and ϕ_0 is proportional to the displacement of the reflecting plane z from the focus. If A is small, the signal obtained at the output of the detector has a term that varies as $A \cos \Omega t \sin \phi_0$. Thus an ac signal is obtained which is zero when the focus is at the surface of the reflecting object. We have made crude demonstrations of an early version of this device; it works. We are now constructing a version of it which is more precisely made to make measurements with better sensitivity and accuracy.

Spherical Mirror

A second system has been constructed using a flexible spherical mirror in the path; it is illustrated in Fig. 7. This mirror is composed of two pieces of PZT ceramic bonded together with a microscope cover slip on which a metal film is deposited and bonded to them. When voltages are applied, as shown in the figure, one PZT disk expands and the other contracts, thus causing the

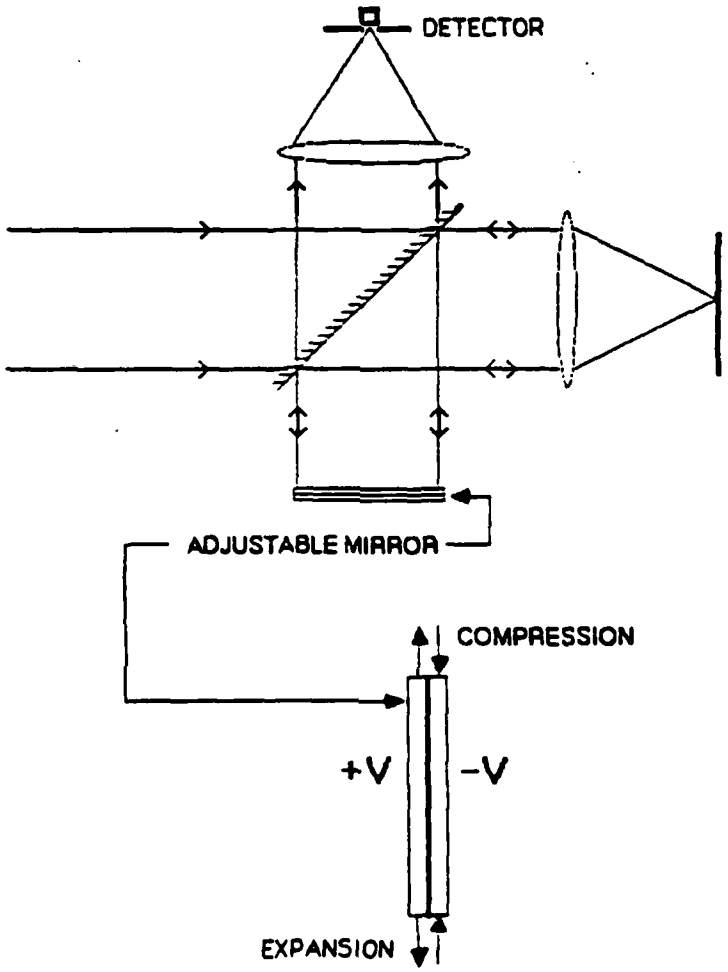

Fig. 7. A schematic of the adjustable mirror system.

mirror to adopt a spherical shape. This moves the focus in and out so that if rf signals are applied to the mirror configuration, an rf output is obtained in much the same manner as the phase contrast Zernike system.

We have tried this system out on our large-scale range sensor with excellent results. In that situation we were able to obtain a sensitivity of the order of 50 μm at a distance of 20 cm . This definition should improve with time. Our theory indicates that the definitions in the microscope, using either this system or the Zernike phase contrast system, should be of the order of 0.001 A .

Transverse Resolution

The transverse resolution of these kinds of systems is also very good. This is because the lens is used twice, both for transmission and reception, so that the response of the system is the square of that of the conventional microscope. This implies that sidelobe levels are low and the 3 dB definition in the transverse direction is improved by about a factor of 1.4 . We will deal with some of these basic results when we describe the electronically-scanned microscope.

We are also concerned with the use of these techniques to measure slope and curvature. When the Bragg cell in the system is driven with a signal of the form $e^{j\omega_0 t}\cos \Omega t$, i.e., with two signals at frequencies $\omega_0 - \Omega$ and $\omega_0 + \Omega$, respectively, it generates two closely-spaced spots on the sample (Figs. 1 and 8). The signals corresponding to the two spots pass along the same path, through the pinhole, to the detector. If the spots strike surfaces with different heights, they will generate a phase signal of the form $\cos(4\Omega t + \phi)$, where $\phi = 2kz$ is the phase difference corresponding to a displacement z of one surface with respect to the other and $k = 2\pi/\lambda$ where

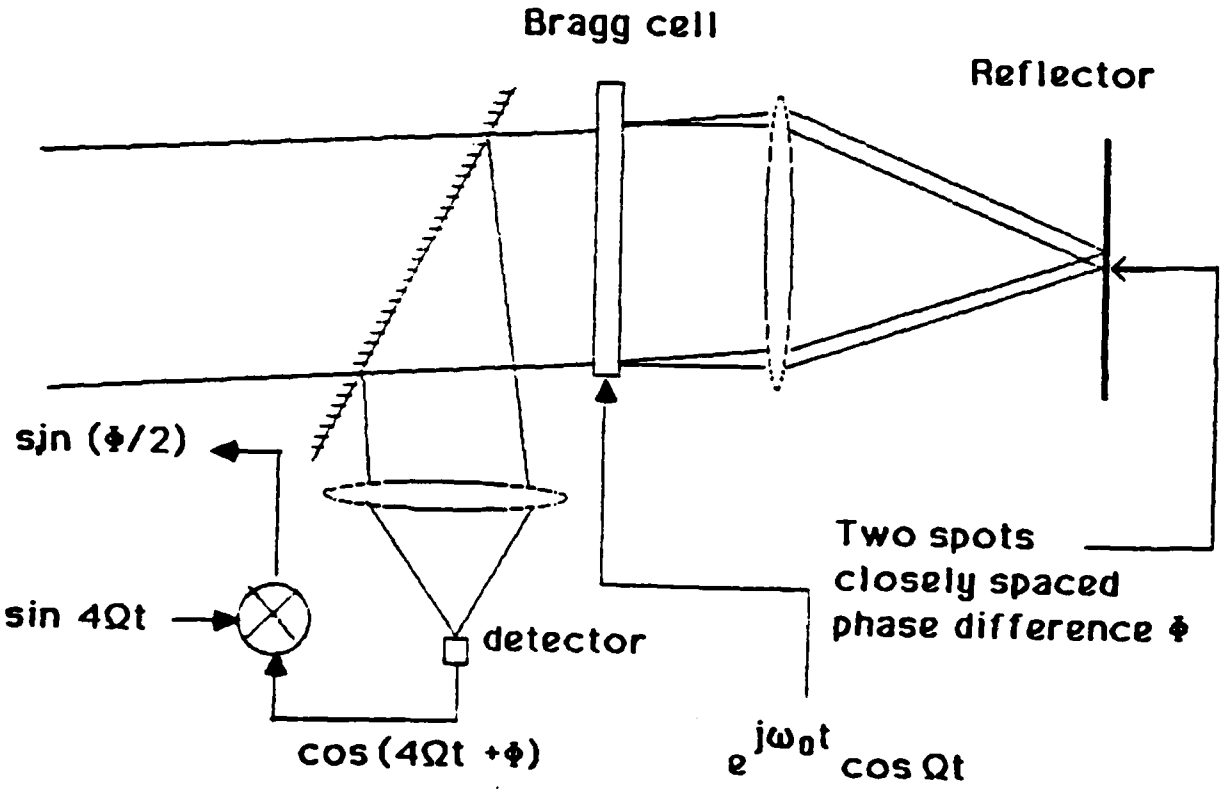

Fig. 8. Differential phase measuring device using a Bragg cell.

λ is the wavelength of the optical beam. Thus, the output obtained is the derivative of the phase variation along the sample, i.e., it is the slope of the surface. If the beams pass over a sharp step, a large peak in output is obtained when they are equally spaced from the step. This makes it possible to locate an edge with great accuracy. An illustration of such results is shown in Fig. 9.

We suggest that, by using a modulated signal with three frequencies in it, we can produce three spots and therefore use the system to measure curvature rather than slope. This could be extremely useful for measuring the diameter of a hole, the eccentricity of a round object, or the wear of an engine cylinder.

We are trying yet other techniques which involve measurements of ac fluctuations associated with photoacoustic modulation by a modulated laser beam using these methods. They are very powerful for measuring thermal bonds and internal defects.

ELECTRONICALLY-SCANNED OPTICAL MICROSCOPE

During the last six months we have made preliminary measurements on the system built into a Leitz microscope. The Leitz Company has loaned us, on indefinite loan, a modified orthoplan microscope with provision made to image the back focal plane of the objective lens on a plane outside the microscope where the Bragg cell can be mounted. The light from an argon laser is passed through a fiber-optic delay line to the Bragg cell.

The basic system is illustrated in Fig. 10. Transfer lenses are mounted inside the microscope, as shown in Fig. 11. At the same time, it is possible to use the microscope in the normal manner with a separate light source and look at the object being measured. This is a major improvement because it

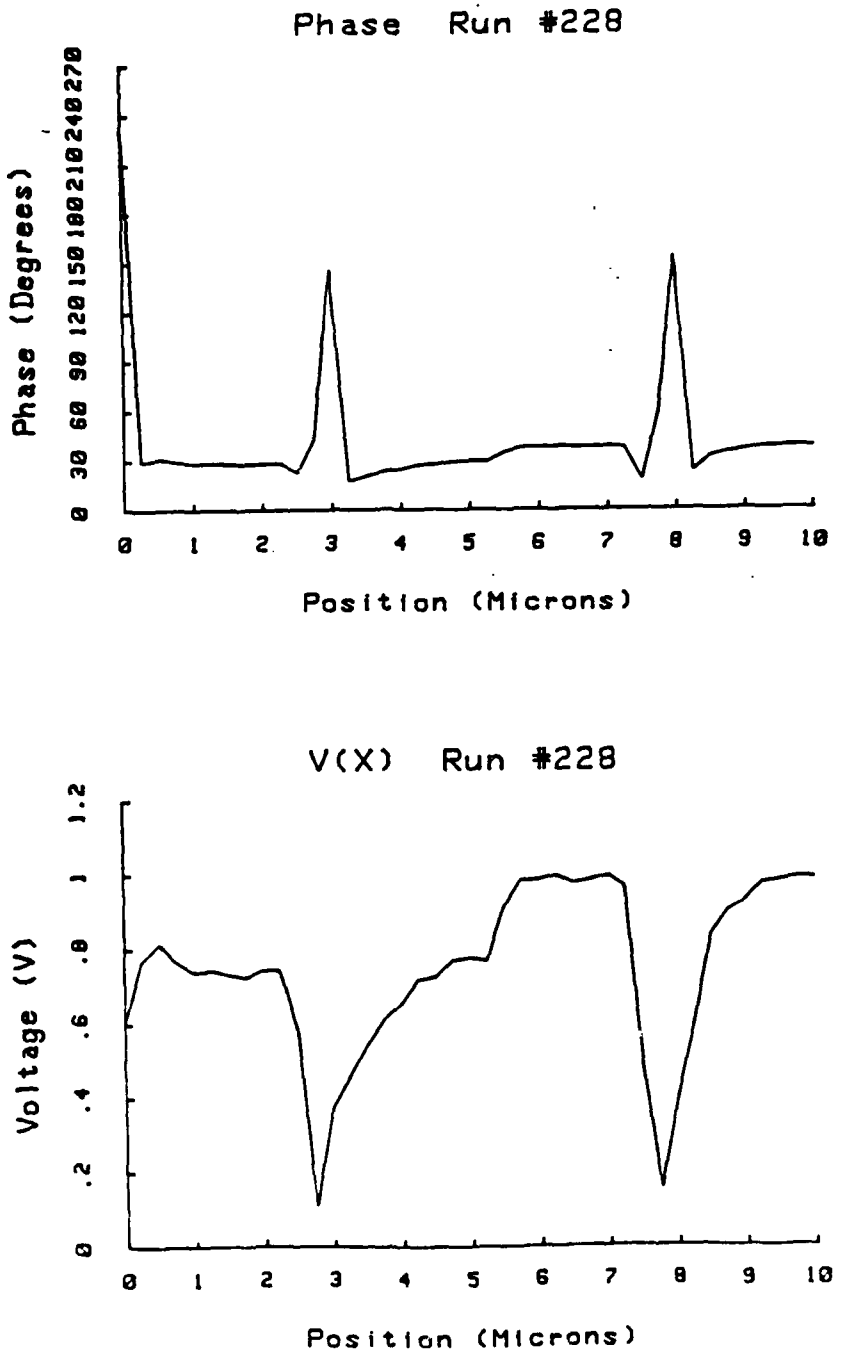

Fig. 9. Differential edge response to a periodic structure.

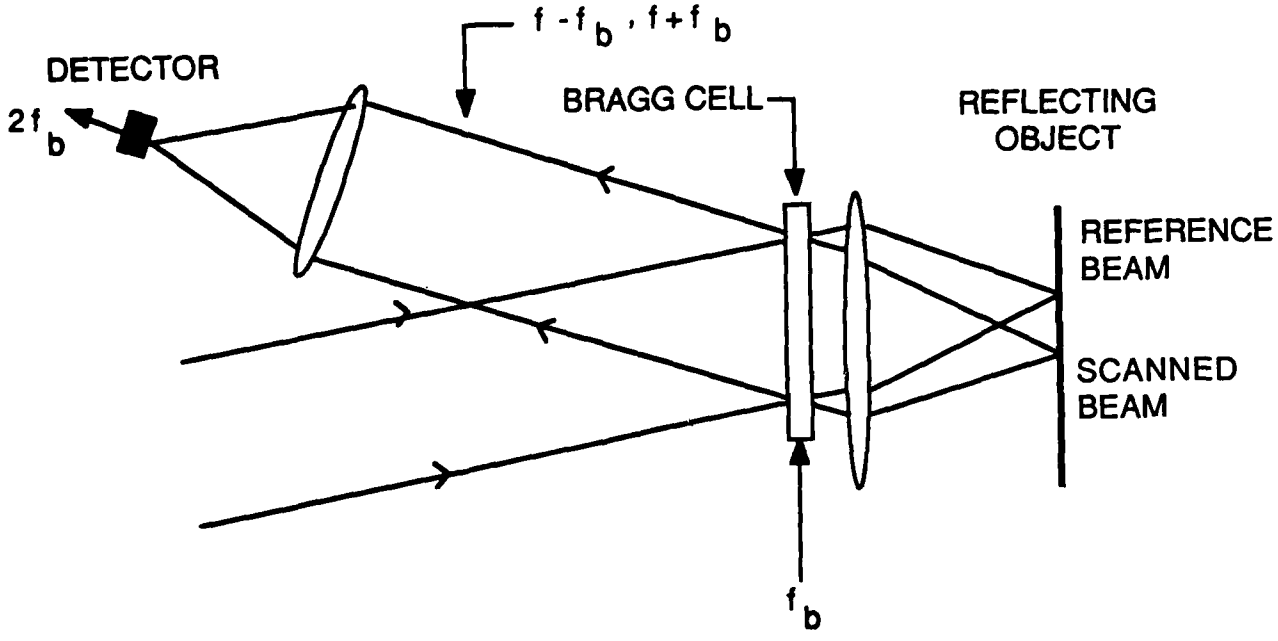

Fig. 10. Basic configuration of the electronically-scanned microscope.

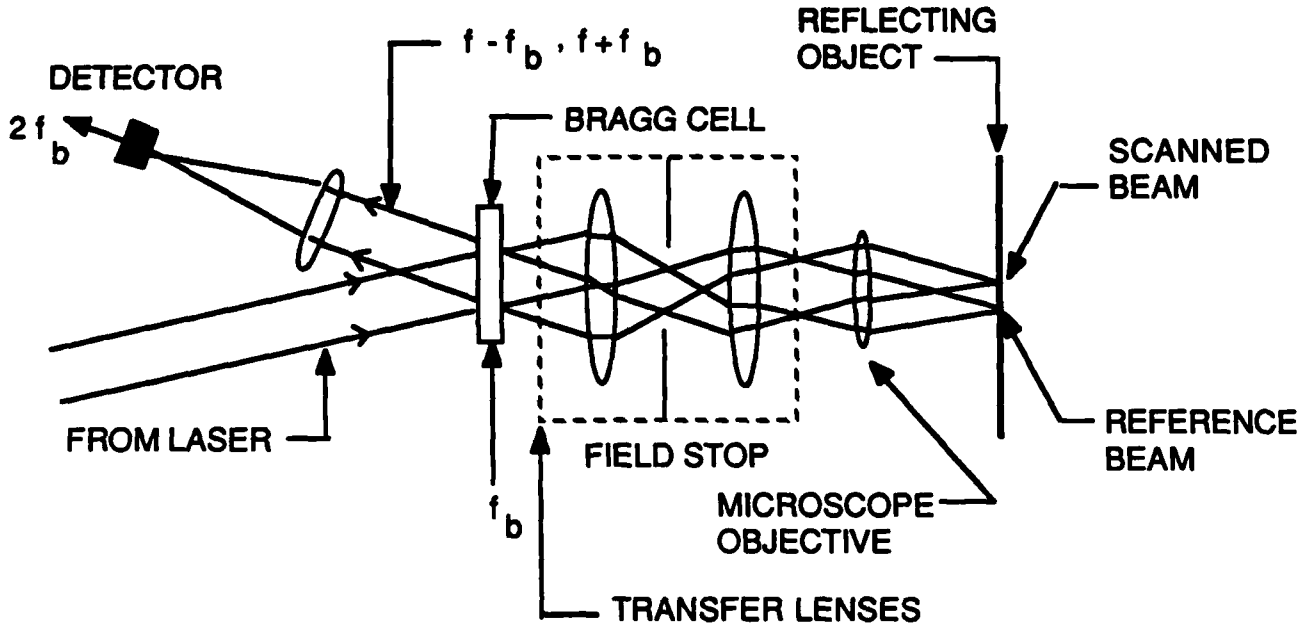

Fig. 11. Schematic of electronically-scanned microscope with transfer lenses and a field step. The second set of beams (tilted into the paper) is not shown.

makes the problems of lining up the system and deciding on a region of interest on a sample far simpler.

Fast Data Acquisition

We have recently completed the construction and testing of an advanced data acquisition system. Completely computer controlled, it includes a digitally programmable VCO to provide scanning on a random access basis (we can access any points on a line in any order we want to), a logarithmic amplitude detector with 12-bit accuracy, 80 dB dynamic range, and most prominently, a successive-approximation phase digitizer with an accuracy of 1/10 degree (corresponding to an uncertainty in sample height of about one Angstrom). All three are capable of operating together at a rate of 50,000 to 70,000 points per second.

This represents an improvement of 500 times in speed and 3-10 times in accuracy over our previous system, which was based on a lock-in amplifier. With improved computer hardware and software, in particular DMA transfer of instructions and data, we could take 512 point lines at 100-140 lines per second.

Submicron Lines

We have made preliminary measurements with the Leitz microscope while building the fast data acquisition system. The worst problem that we have encountered with the present system is a poor signal-to-noise ratio. This is mainly due to loss of light in the beam splitters inside the microscope. The one-way loss of each beam is of the order of 7 dBs , but since the beams are used in a reflection mode and their product is taken in the detector, the output power from the detector is decreased by 28 dB , a serious loss. This will be remedied by replacement of one of the beam splitters, the main source

of loss, and by improvement in the broadband detector matching circuit. We expect to obtain a 30 dB improvement in signal-to-noise ratio with these stratagems.

We have carried out scans of 900 A thick step of aluminum on aluminum. The measured phase variation across this step is shown in Fig. 12. A theoretical curve is plotted on top of the experimental results. The agreement between experiment and theory is relatively good. In these results, the distance between the 10-90% height points is approximately 0.25 μm (0.5 wavelengths); thus, the resolution of the system is already very good, and better than with the standard optical microscope.

Because we have both amplitude and phase information available, we can inverse filter the data to obtain better transverse resolution. When we do this using different choices for the deconvolution filter, we obtain the results shown in Fig. 12. The choice of deconvolution filter is dictated by how much ripple we wish to obtain at the edges of the step: the worse the ripple, the worse the resolution. An intermediate curve shown gives a 10-90% edge definition of the order of 0.15 μm after post-processing. We have carried out similar measurements on a 1000 A thick metal film 0.97 μm (1.8 wavelengths) wide. Referring to Fig. 13, the upper figure shows the uncorrected measurement of the film; we observe both its height and its width. After inverse filtering, the shape becomes almost rectangular, and the height of the curve is almost at its full value for a step. Therefore, this procedure enables us to measure simultaneously both height and width of the film, a major improvement over most current metrology systems.

The high performance is further illustrated by the sharp image of the 0.61 μm (1.2 wavelengths) wide line, shown in Fig. 14. Micron and submicron line widths are generally measured by fitting a model to the observed data and

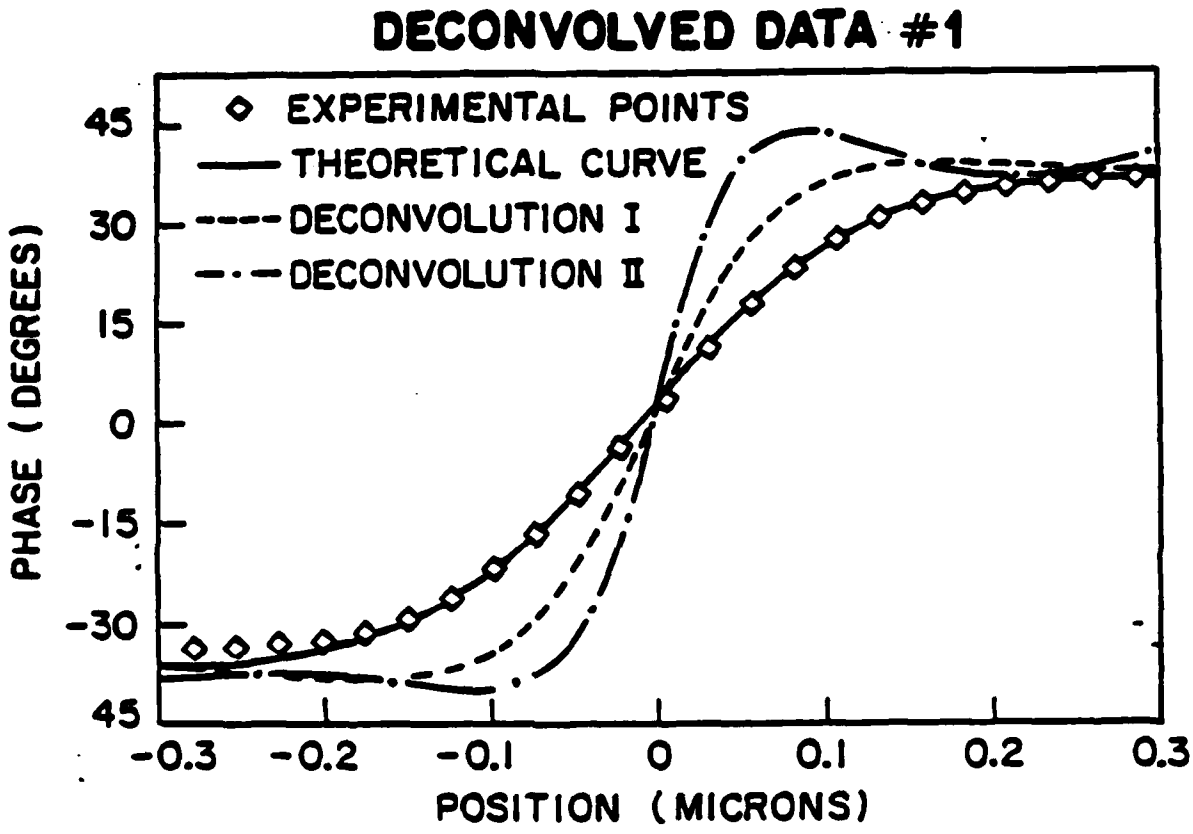

Fig. 12. A comparison of three results taken on a 900 Å step of aluminum on aluminum with the electronically-scanned microscope. The experimental results are compared with theory, along with improvements in the step response made by using two different inverse filters.

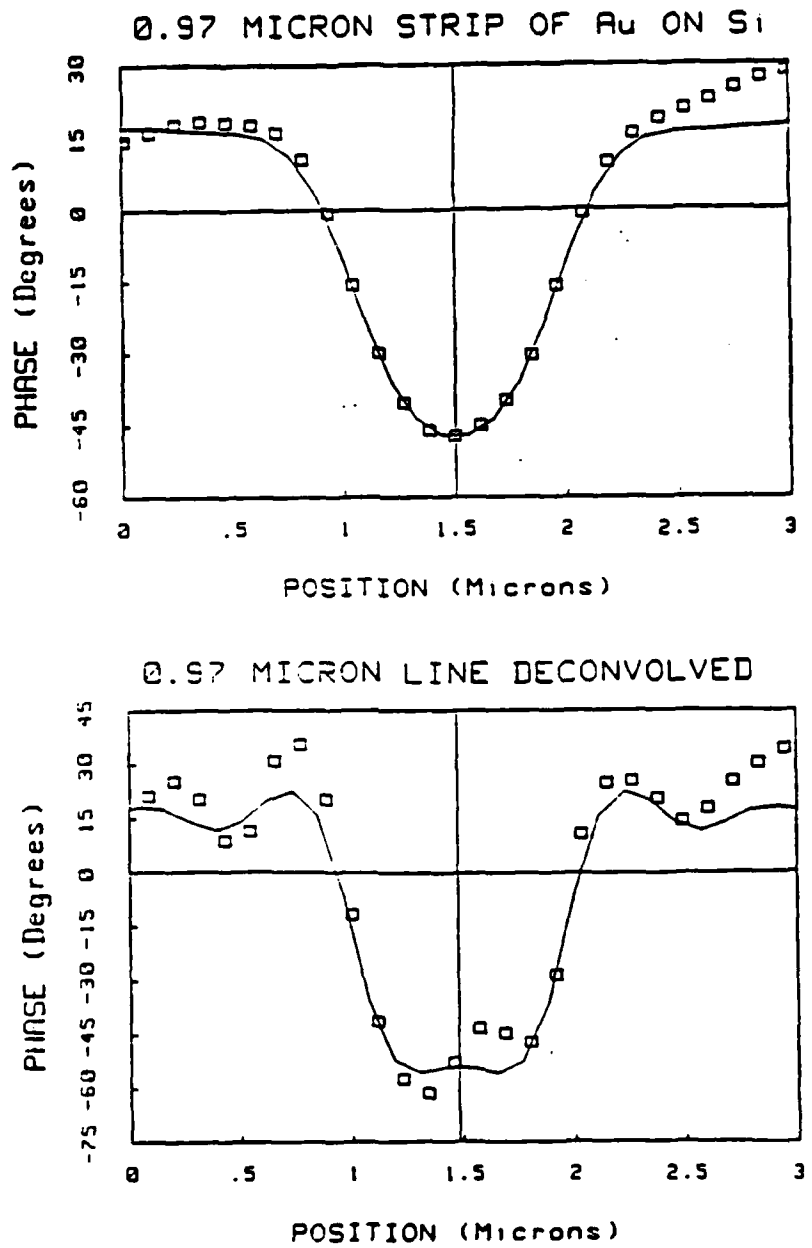

Fig. 13. A comparison of phase measurements taken on a 1000 Å thick metal film 0.97 μm wide (upper figure), with the results (lower figure) after inverse filtering.

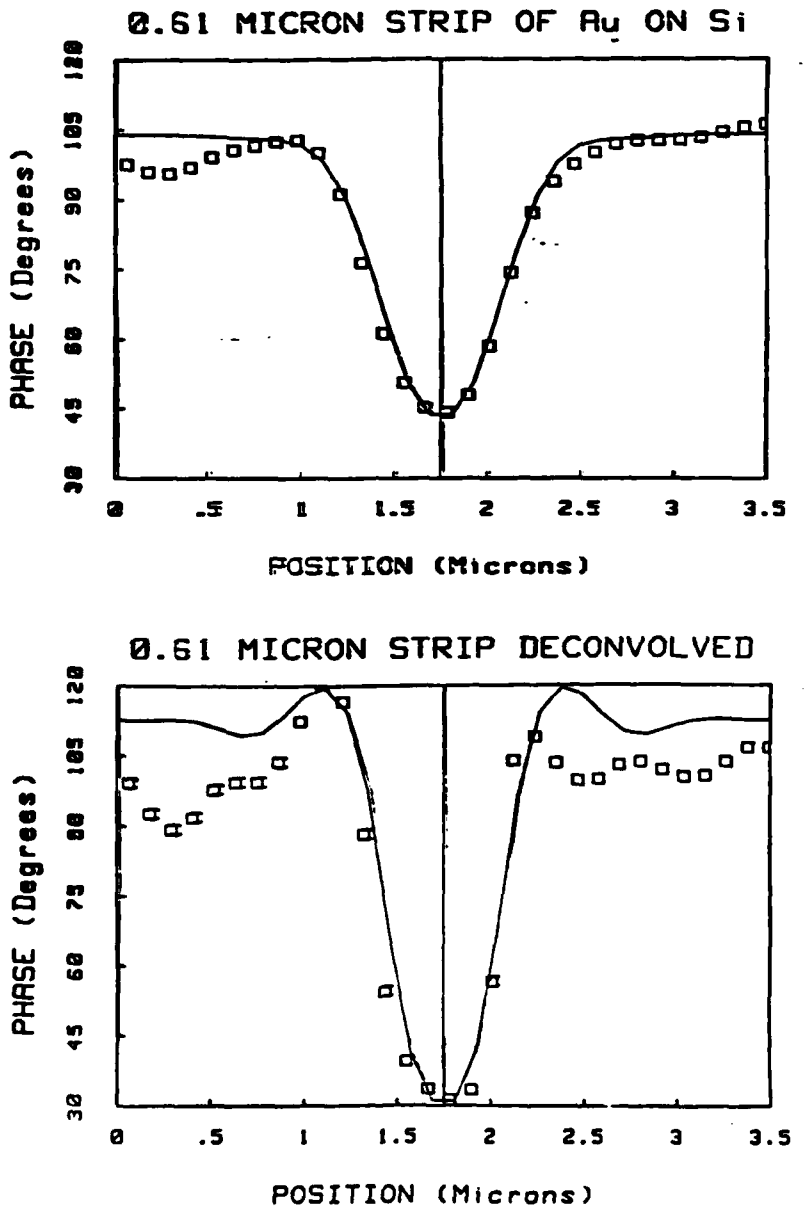

Fig. 14. A comparison of phase measurements taken on a 1000 A thick metal film 0.61 μm wide (upper figure), with the results (lower figure) after inverse filtering.

extracting height and width from the model parameters. The great sharpness and the amplitude/phase capabilities of our system make possible much more accurate measurements by presenting more information to the model.

Further Developments

In the next few weeks, we plan to make two improvements in the optics of the system. The present system has four beams incident on the sample, which necessitates the use of special samples containing a featureless, flat, mirrored area for two of the beams. The second set of beams is used to produce a reference electronic signal. We plan to reflect this second pair of reference beams from a removable plane mirror located at an internal field stop of the microscope, located at an image plane of the object, as shown in Fig. 11. This mirror duplicates the function of the special samples without their difficulties.

In addition, we plan to introduce a second, fixed acoustic frequency into the Bragg cell. This will produce a second stationary spot near one edge of the scanned region which will take over the function of the undiffracted spot in the present system without the attendant loss of field-of-view. In addition, the extra frequency shift will greatly simplify the rf signal processing.

CONCLUSION

We have demonstrated a number of new measurement systems suitable for long-distance range sensing as well as microscopic range and transverse resolution sensing. The systems are applicable for use with photolithography, for material measurements, and for measurements during manufacture, as well as in applications in nondestructive testing of small and large samples in the field.

PUBLICATIONS

1. C-H. Chou and G. S. Kino, "The Evaluation of V(z) in a Type II Reflection Microscope," submitted to IEEE Trans. on Sonics and Ultrasonics (November 1985).
2. K. K. Liang, S. D. Bennett, and G. S. Kino, "Precision Phase Measurement with Short Tone Burst Signals in Acoustic Microscopy," Submitted to Review of Scientifc Instruments (April 1985).
3. P. C. D. Hobbs, R. L. Jungerman, and G. S. Kino, "A Phase Sensitive Scanning Optical Microscope," presented at SPIE's Annual International Technical Symposium, San Diego, California (August 1985).
4. P. C. D. Hobbs, "A Simple Expression for the Line Spread Function of a Confocal or Incoherent Microscope," Submitted to J. Opt. Society of America (September 1985).

Appendix I

Precise Phase Measurements with the Acoustic Microscope

KENNETH K. LIANG, SIMON D. BENNETT, MEMBER, IEEE, BUTRUS T. KHURI-YAKUB, MEMBER, IEEE, GORDON S. KINO, FELLOW, IEEE

***Abstract*—The measurement and the use of phase in acoustic microscopy are discussed. It is demonstrated that in many applications phase can be used to provide sensitivity and information unparalleled by amplitude-only measurement methods. A technique capable of high-accuracy measurement of the phase of short RF acoustic pulses is described. The power of this phase measurement technique is illustrated in a number of applications. Surface material property measurements such as the Rayleigh-wave velocity and the inversion of the complex $V(z)$ to obtain the reflectance function of a liquid-solid interface are considered. Surface topography mapping based on phase measurement is examined. A Fourier transform approach for precision determination of linewidths comparable to the resolution spot size is also presented.**

I. Introduction

THE SCANNING acoustic microscope is a high-resolution imaging system in which, unlike conventional optical microscopes, it is relatively straightforward to measure the phase of the return signal. With only a few exceptions [1]-[3], attention has centered only on the use of intensity information. In some of the main areas of application of the acoustic microscope, the phase of the received signal plays an important role. For example, in the so-called $V(z)$ measurements [4]-[7], the amplitude of the received signal $V(z)$ as a function of the separation between the lens and the substrate exhibits periodic peaks and nulls. This phenomenon is due to the beating between a specularly reflected signal from the substrate and a delayed leaky Rayleigh-wave signal, which reemits to the lens while propagating along the surface of the substrate. The phase difference between these two signal components is therefore of great importance, and in fact it controls the contrast of reflectional images. In addition, it has been shown that the independent measurement of phase and amplitude can be very useful in the determination of the elastic constants of tissue [8], [9]. However, little effort has been made to extract the phase of the return signal separately.

One reason for the reluctance to make use of the phase is that it is not generally trivial to measure the phase of a high-frequency tone burst with sufficient accuracy. We will describe here an approach that is relatively easy to implement and capable of yielding high-precision phase data, even from very short tone bursts. The details of the phase measurement technique will be published elsewhere, and we will concentrate here on some of the applications of the system to acoustic microscopy.

There are many motivations for making measurements of this type. Firstly, they offer a direct indication of material properties as in the measurement of Rayleigh-wave velocity. Also, the results of the phase measurement can be used to infer the width and the height of surface features. Finally, the combination of amplitude and phase measurements can be used in the reconstruction processes in which complete information about the interaction between acoustic field and material is required, as in the inversion of $V(z)$ data to find the reflection coefficient as a function of angle [10].

II. Phase Measurement Scheme

A. Acoustic Lens Configuration

In making precise phase measurements that are related to physical properties, it is generally important to ensure that the reference signal, against which the phase of the probing signal is to be compared, and the probe itself share as many of the instrumental and environmental phase disturbances as possible. In other words, precise measurements are best done in an interferometer, where the two arms are closely matched.

In this work we have made use of two acoustic measurement configurations that largely satisfy this general condition. The first (Fig. 1(a)) is reminiscent of the defocused condition used in $V(z)$ measurements, except that here a fixed separation between the lens and the sample surface is maintained. Two components of the acoustic field returned to the lens contribute most significantly to the output signal: the on-axis specular reflection of the longitudinal wave in the water (L in Fig. 1a); and the off-axis rays (R), which satisfy the condition $v_W/v_R = \sin\theta_R$ for the conversion of longitudinal waves with velocity v_W in the water to leaky Rayleigh waves with velocity v_R on the surface of the sample [4], [5].

These two signals, L and R, differ slightly in path length in water but otherwise experience much the same environ-

Manuscript received September 1984; revised December 1984. This work was supported by the Air Force Office of Scientific Research under Contract F49620-79-C-0217.

K. Liang, B. T. Khuri-Yakub, and G. S. Kino are with the Edward L. Ginzton Laboratory, W. W. Hansen Laboratories of Physics, Stanford University, Stanford, California 94305, USA.

S. D. Bennett is with Datasonics Corp., 911 Del Avenue, Campbell, CA 95008, USA.

0018-9537/85/0300-0266$01.00

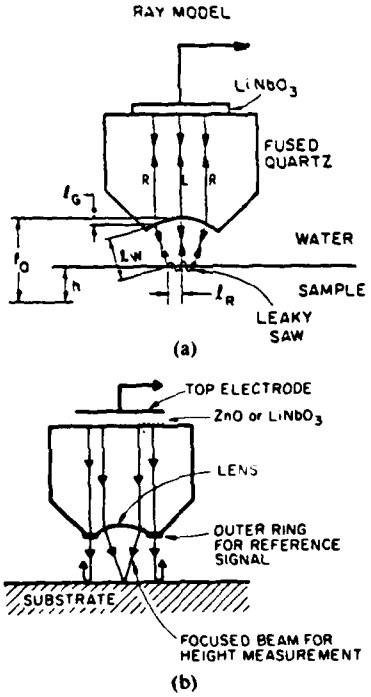

Fig. 1. Acoustic lens configurations. (a) Rayleigh-wave velocity perturbation measurement. (b) Topography mapping.

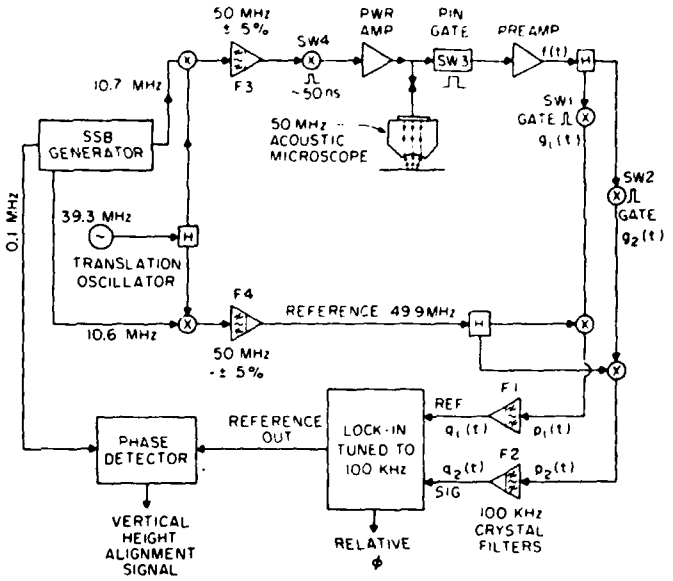

Fig. 2. Schematic for the phase measurement system.

mental disturbances. However, the Rayleigh-wave component acquires substantial phase delay at the surface of the specimen, hence the effective path length for the R signal is longer than that of the specular reflection. Indeed in our experiments we use the different arrival time of these two return signals to facilitate their separation and subsequent phase comparison. The excitation signal is two to three cycles in duration, and the defocus distance is sufficient that there is no temporal overlap of the signals. It is clear that changes in the Rayleigh-wave velocity as a function of position along the surface of the specimen may be sensed in this way. By combining a high-accuracy phase measurement scheme with a suitably extended Rayleigh-wave path, remarkably sensitive measurements can be made.

The second configuration that concerns us is illustrated in Fig. 1(b). In this case the lens is positioned so that its focus is at the surface of the specimen or slightly above it so that no Rayleigh wave of importance is excited. A reference path is provided by an annular beam that propagates through the flat outer periphery of the lens. By exciting the lens with a short pulse, and once again using time discrimination to separate the signals from the two different paths, an interferometer is formed. Now small local changes in the surface topography result in large changes in the phase of the focused beam relative to the phase of the large diameter reference beam.

In both measurement configurations it is apparent that the signals of interest arrive at different times, and this would ordinarily make phase comparison impossible. However, the electronic system described in the next section essentially reconstructs two phase-coherent continuous signals that are directly related to the amplitudes and phases of the two time-distinct return signals.

The first configuration is also used where the signal of interest is the transducer output voltage, when the system is operated in the $V(z)$ mode. In this case the exciting signal has a much longer duration so that the return signals (L and R) overlap and interfere at the transducer even for large defocus distances. The idea here is to measure both the amplitude and the phase of the signal relative to some reference as a function of the axial separation z between the acoustic lens and the specimen. The resulting complex $V(z)$ can be inverted [10] to obtain the angular dependence of the reflectance of the liquid–specimen interface. From the reflectance function, various material property parameters can readily be extracted.

In the experiments described here, a center frequency of 50 MHz was used with an acoustic transducer having a bandwidth of 20 percent. The lens material was fused quartz and had a radius of curvature of 3.2 mm, giving a focal length in water of 4.24 mm. The opening aperture of the lens was 5.0 mm in diameter, corresponding to a maximum half angle of 36° or an f-number of 0.85.

Providing the same fractional bandwidth can be maintained, there should be little difficulty in applying the same techniques to a system operating at much higher frequency, perhaps up to 2 GHz. Beyond that frequency, limitations in the electronic-switching components presently available may present difficulties.

B. Electronics

The essential elements of the phase measurement electronics are shown schematically in Fig. 2. The system will be described in detail in a forthcoming paper [18], where various sources of error and an analysis of the ultimate performance are discussed. A more general review of the concepts will suffice here.

The basic scheme involves signal recovery by synchronous detection and subsequent phase measurement with a lock-in amplifier. The key component (Fig. 2) in the signal source is the single sideband generator (SSB) with synchronous outputs at 100 kHz, 10.6 MHz, and 10.7 MHz. The 10.7-MHz output is in fact the upper sideband of the product of the 100 kHz and 10.6-MHz signals. The lower sideband at 10.5 MHz is suppressed by at least 50 dB using a standard FM radio system IF filter. The translation oscillator shifts the operating frequency up to the desired center frequency of the acoustic system, which is 50 MHz in this case. A reference signal at 49.9 MHz is also generated. Again the lower sideband components of the product signals have to be removed. At this point however the filtering requirements are not as stringent as in the SSB generator and tunable bandpass filters (F3 and F4) with five-percent bandwidth are adequate, since the sidebands are now widely separated. This signal generation scheme is flexible in that the operating frequency is tunable over a fairly wide range, which is limited in this case to 100 MHz by the bandpass filters. For much higher frequency of operation, filters with greater selectivity would be needed or, alternatively, successive stages of heterodyning could be used with filtering at each stage to step up incrementally to the desired operating frequency.

As illustrated in Fig. 2 with a 50-MHz acoustic microscope, the 50-MHz continuous wave (CW) signal is time-gated to produce a short tone burst that excites the acoustic transducer. Switch SW3 is used as a time gate to pass the low-level acoustic return signals of interest and to block high-level extraneous ones, which may damage the preamplifier. The acoustic return signals are time-separated RF pulses, and they are electronically separated through time-gating into two channels as shown. Each of the resulting signals is mixed with the 49.9 MHz reference signal, and the product is narrow-band filtered to extract the 100-kHz component.

It can be shown [18] that the 100-kHz signals are essentially low-frequency CW replicas of the pulse modulated RF acoustic signals, bearing identical phase and amplitude information. With a biphase lock-in amplifier tuned to 100 KHz, one can readily measure the phase difference between the two signals and also the amplitude of the signal being fed to the "signal" channel of the lock-in, if it is required. Phase sensitivity is basically limited by the lock-in amplifier because the problem of system noise can in most cases be overcome by increasing the integration time in the lock-in output stage. This effectively reduces the system noise bandwidth, but it also includes the obvious disadvantage of longer data acquisition time. Good-quality lock-in amplifiers routinely have phase resolution of the order of 0.1°, which corresponds to an overall system phase sensitivity of 1/3600 of a wavelength.

In velocity perturbation measurements the measured phase is dependent on the distance between the lens and the specimen. This distance changes with the sample surface topography and is susceptible to thermal drift as well, thus introducing phase error into the measurement. To minimize this error, a feedback mechanism is employed to keep the lens-to-specimen spacing constant. The acoustic lens is mounted on a piezoelectric (PZT) stack so that its vertical position can be adjusted continuously by an electronic control signal. The acoustic on-axis reflection pulse, whose phase is a direct measure of the lens to sample distance, is applied to the reference channel of the lock-in amplifier as shown in Fig. 2. The reference channel generates a 100-kHz constant-amplitude phase-locked replica of the reference input, which is then compared with the 100-kHz output of the SSB generator to produce the control signal for the PZT stack. The acoustic lens automatically tracks the surface topography of the sample during scanning to ensure that the measured phase change is due to material property variation alone. This feedback mechanism is also used effectively in such modes of operation as topography measurement to compensate for thermal effects.

III. Applications

The power of this measurement scheme is illustrated in the following with a number of examples. We will consider both material property measurements, such as Rayleigh-wave velocity and complex reflectivity, and surface topography measurements.

A. Velocity Perturbation Measurements

In this section we will specifically deal with the perturbation to the Rayleigh-wave propagation velocity as a result of material property change and also the presence of surface residual stress.

1) Velocity Perturbation Due to Thin-Film Overlay: The sample in this example is a multiple-thickness indium film deposited on glass. The thicknesses are 240 Å and 620 Å, respectively. The objective was to measure the perturbation of the Rayleigh-wave velocity caused by the indium film. A line scan over the surface of the sample (Fig. 3) exhibits phase changes of 7° and 11° for the 240-Å and 380-Å step changes in film thickness. The spatial resolution of the system is defined by the Rayleigh-wave path length on the substrate and is determined to be about 0.8 mm from the step transition width in the line scan. It can be calculated from first order perturbation theory [11] that the velocity perturbation due to the indium film is 0.18 percent and 0.46 percent for the 240-Å and 620-Å layers, respectively. Based on these estimated parameters, one would expect phase changes of 7.6° and 12° for the 240-Å and 380-Å step transitions. Hence there is fairly good agreement between the experimentally obtained and theoretically predicted phase changes. It should also be noted that in the line scan, the small phase variations in the supposedly flat regions of the indium film are real and repeatable. The fluctuations are less than 0.5° and are due to nonuniformity in the thickness of the indium film. Since the phase sensitivity of the system is limited by the lock-in amplifier to 0.1°, this measurement technique can po-

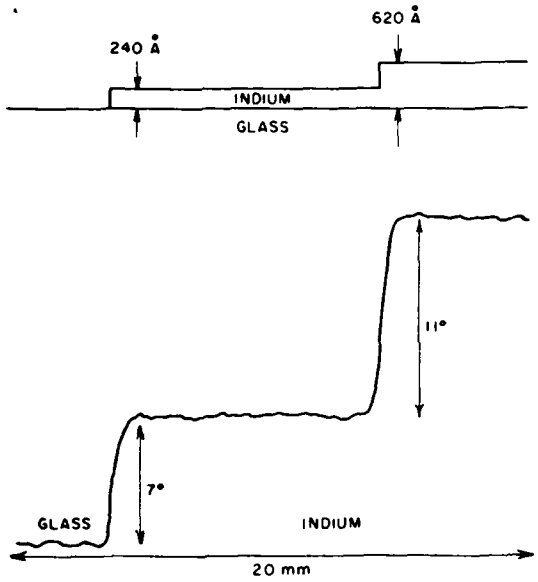

Fig. 3. Measurement of velocity perturbation due to indium film on glass.

tentially detect velocity perturbations on the order of one part in 10^5.

2) Residual Stress Measurement: In nondestructive testing, knowledge of the surface residual stress distribution in a component plays an important role in the prediction of failure modes. One way of characterizing residual stress is by measuring the acoustic wave propagation velocity, which varies linearly with the local stress [12]. With the measurement configuration shown in Fig. 1(a) the measured change in the relative phase between the *L* and *R* signal pulses as the lens is scanned can be shown to be directly proportional to the residual stress on the object surface [13].

The sample used in the experiment is a glass disk of two inches in diameter that was heated and then thermally quenched with air jets to introduce a radial distribution of residual stress. Fig. 4(b) shows the radial variation of the measured phase perturbation. For comparison a destructive test was carried out on a similar sample to determine the actual residual stress distribution. A Vicker's indenter was used at a prescribed load to produce median cracks at different points on the glass disk. By measuring the crack lengths, the residual stress as a function of radial distance was calculated [14]. The result of the destructive test is shown in Fig. 4(a). The variation of the principal stresses are essentially the same, with the radial and tangential components tracking each other to within 20 MPa. Since the phase measurement is omnidirectional in that a spherical lens was used to launch Rayleigh waves propagating in all directions along the surface, the resulting phase perturbation is a measure of the sum of the principal stresses. Comparison of Figs. 4(a) and 4(b) shows that there is fairly good corroboration between the phase perturbation curve and the actual residual stress distribution. From these results we empirically deduce that 40 MPa of stress, which is the change from the center of the sample to the

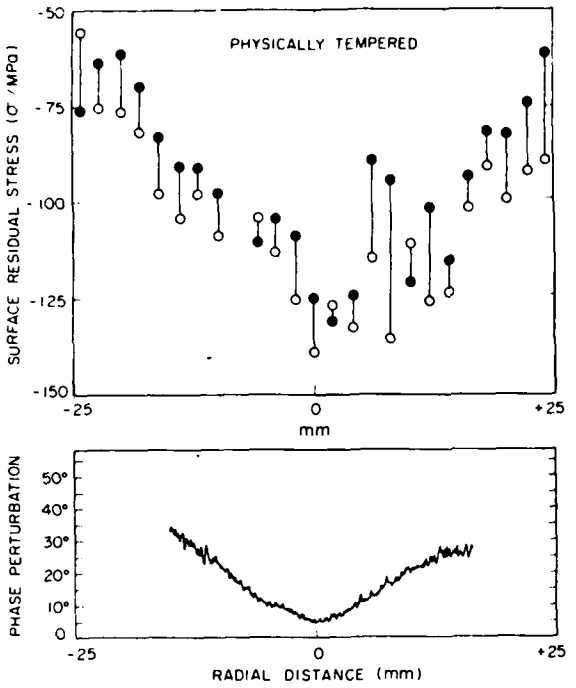

Fig. 4. Residual stress measurements on the surface of a tempered glass disk. (a) Variation of radial (open symbols) and tangential stresses (closed symbols) across a diameter of the glass disk estimated from indentation fracture tests. (b) Radial variation of measured phase perturbation.

limit of the line scan, corresponds to a phase variation of 30°.

B. Surface Topography Measurements

We have used the acoustic microscope in the measurement configuration shown in Fig. 1(b) as a high-resolution noncontacting profilometer [13], [15]. Besides being able to make use of phase profile to map the depth variation, we can also determine with high precision the transverse profile of surface features in special cases. Of particular interest in this regard is the measurement of the widths of long rectangular strips, which is a matter of great concern in the fabrication of semiconductor components. We will show here both experimentally and theoretically the advantages of utilizing phase to determine the linewidth. We will also introduce here a Fourier transform technique for linewidth measurement in cases where the strip width is comparable to the spot size.

1) Depth Profiling: Topography images of metallized stripe patterns on a fused-silica substrate are shown in Figs. 5(a), 5(b), and 5(d). The patterns have progressively finer pitches and the linewidths are 250, 125, and 62.5 μm, respectively. The metallization is gold with a thickness of about 3000 Å. The gold stripes show up as bright areas in the images. At 50 MHz, with an f-number of 0.85 and a uniformly excited aperture, the Rayleigh resolution of the acoustic lens is 1.13 Fλ = 0.96 λ or 29 μm, while the 3-dB resolution is 0.64 Fλ = 0.54 λ or 16 μm. The 62.5-μm line image in Fig. 5(d) is clearly resolved, as would be expected. The amplitude image of the 125-μm stripes is shown in Fig. 5(c) for comparison. There is vir-

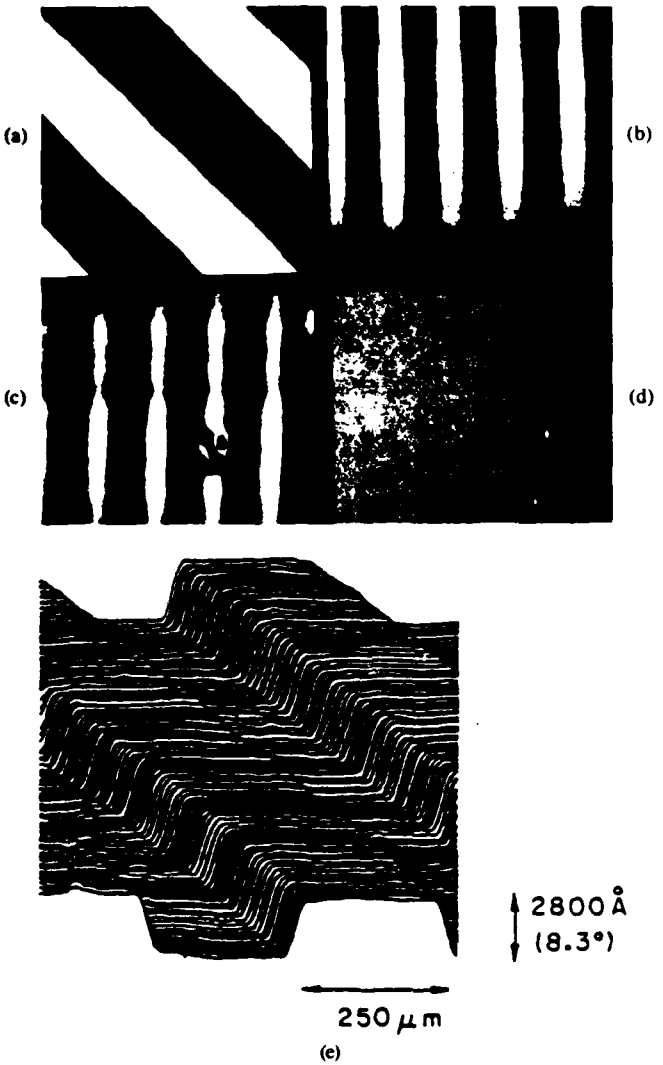

Fig. 5. Topography images of striped metallization patterns on a fused quartz substrate. The metallization is gold and the thickness is about 3000 Å. (a) Phase image of 250-μm lines. (b) Phase image of 125-μm lines. (c) Amplitude image of 125-μm lines. (d) Phase image of 62.5-μm lines. (e) Perspective plot of the measured topography map of the 250-μm line pattern.

tually no contrast to suggest the presence of a striped pattern, clearly illustrating that phase is a far more sensitive means of gauging distances. The measured phase difference between the surface of the metallization and the surface of the fused-silica substrate is 8.3°, which corresponds to a film thickness of 2800 Å after taking into account the angular dependence of the complex reflectance function and the effect of focusing.

We will show here that, based on theoretical considerations, indeed the phase rather than the magnitude of the acoustic microscope output $V(x)$ is a more sensitive measure of the depth profile. Consider the simple case of a rectangular strip of width w on a substrate of identical material. Assume that the reflection coefficient Γ_0 of the surface is real. Then the spatial response of the strip structure is given by

$$R(x) = \Gamma_0 + \Gamma_0 (e^{j\phi} - 1) \text{ rect } (x/w) \tag{1}$$

where ϕ is the phase change due to the thickness of the strip. Let the response of the imaging system to a line source be $h(x)$. Furthermore, suppose that the lens is uniformly illuminated in the back focal plane and the lens is aberration-free so that $h(x)$ is real. The acoustic microscope output is therefore given by

$$V(x) = R(x) * h(x) \tag{2}$$

or

$$V(x) = \Gamma_0 K + \Gamma_0 (e^{j\phi} - 1)\, s(x) \tag{3}$$

where

$$s(x) = h(x) * \text{rect } (x/w) \tag{4}$$

and

$$K = \int_{-\infty}^{+\infty} h(x)\, dx.$$

The first term on the right-hand side of (3) corresponds to the constant background reflection from the substrate, and the second term corresponds to the additional spatially varying contribution that is due to the strip. It can easily be shown that for a thin strip where $\phi << 1$, to second order in ϕ, the magnitude and the phase of $V(x)$ are given respectively by the relations

$$V_{\text{mag}}(x) = \Gamma_0 K + \frac{\Gamma_0\, s(x)}{2} [s(x) - K]\, \phi^2 \tag{5}$$

and

$$V_{\text{phase}}(x) = \frac{\phi}{K} s(x). \tag{6}$$

The $V_{\text{phase}}(x)$ is directly proportional to ϕ, whereas the spatially varying part of $V_{\text{mag}}(x)$ depends on ϕ to the second order. Thus for thin strips, phase is a much more sensitive measure of the depth profile.

2) Linewidth Measurement: A major advantage of scanned confocal imaging systems such as ours is that because the point spread function is always positive and falls off rapidly at large distances, there is hardly any ripple in the amplitude of the step response [16], [17]. A similar smooth transition in the phase of the step response can also be observed in the perspective plot shown in Fig. 5(e). For the purpose of comparison, we have carried out a numerical analysis for the step phase responses of different imaging configurations. For small step heights, or equivalently small phase changes, the normalized phase step response is of the form

$$\beta(x) = \int_x^{\infty} g(r) \cos^{-1} (x/r)\, r\, dr \tag{7}$$

where x is the distance between the center of the beam and the step, and $g(r)$ is the point response function of the imaging system. It is assumed that regions on either side of the step are of equal reflectivity. The step response function is plotted in normalized form in Fig. 6 for two

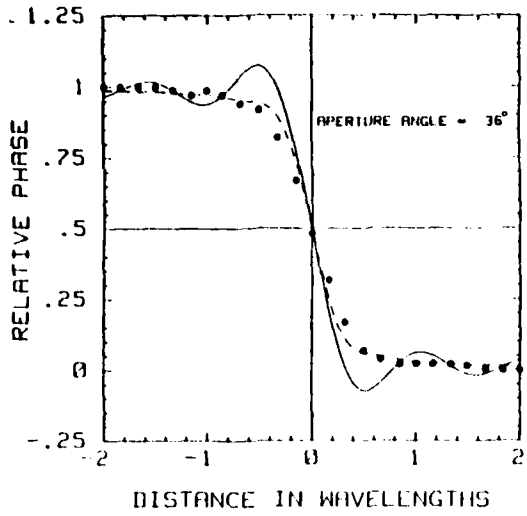

Fig. 6. Step phase response of a normal phase interference microscope (solid curve) and a confocal imaging system (theory in dashed curve, experimental result in closed circles).

different cases. The solid curve corresponds to $g(r) = \text{jinc}\,(2r \sin\theta/\lambda)$, which is the point response of a normal phase interference microscope where the illumination is a plane wave. Here θ is the maximum half angle of the objective lens; λ is the wavelength of the illumination; and jinc (x) is defined as $2J_1(\pi x)/\pi x$. Note that in this case $g(r)$ reverses in sign and its corresponding step phase response does not change monotonically with distance. The dashed curve corresponds to $g(r) = \text{jinc}^2\,(2r \sin\theta/\lambda)$, the point response of a confocal system. The confocal response shows a distinct lack of ripples. The experimentally measured step phase response is also plotted in closed circles showing close agreement with theory. In both imaging configurations, the 50-percent threshold of the phase profile demarcates the location of the edge. It is obvious, however, that the smooth transition of the confocal step phase response enables a straightforward and unambiguous determination of not only the strip thickness but also the strip width.

The 50-percent threshold criterion used to locate the edges of a strip for estimating the linewidth is a valid one for wide strips. For strip widths comparble to the spot size of the imaging system, the step responses of the two edges are in close proximity and tend to interfere with each other, making the establishment of a general criterion for locating the strip edges difficult. We will describe here a Fourier-transform method that circumvents these difficulties.

Applying Fourier transform to (6) and using the definition of $s(x)$ in (4), the spatial frequency spectrum of $\tilde{V}_{\text{phase}}(f_x)$ is given by

$$\tilde{V}_{\text{phase}}(f_x) = \frac{\phi}{K} H(f_x) \cdot w\,\text{sinc}\,(wf_x) \tag{8}$$

where $H(f_x)$ is the Fourier transform of $h(x)$. The term with the sinc function corresponds to the Fourier transform of the spatial variation of the strip and its zeroes are located at

$$f_x = n/w, \qquad n = 1, 2, 3, \cdots. \tag{9}$$

The term $H(f_x)$ represents the angular spectral response of the imaging system. For a confocal system $|H(f_x)|$ is maximum at $f_x = 0$ and generally falls off monotonically, until it becomes zero at the upper cutoff frequency of

$$f_{x_{\max}} = 1/(F\lambda)$$

where F is the f-number of the lens, and λ is the wavelength of the illumination [16], [17]. Hence the zeroes of $\tilde{V}_{\text{phase}}(f_x)$ are those of the strip response within the passband of the imaging system. As long as

$$w > F\lambda \tag{10}$$

the strip width w can be determined using (8) from the locations of the zeroes of $\tilde{V}_{\text{phase}}(f_x)$. In our case $F = 0.85$, so in principle we can determine linewidths as small as 0.85 λ or 25 μm at 50 MHz in water.

The merit of this Fourier-transform technique lies in its simplicity. Given *a priori* knowledge of the strip geometry, one does not need to know the exact nature of imaging system. The mere location of the zeroes for the spectral response of the object suffices for the accurate determination of the linewidth.

Fig. 7 illustrates the experimental $|\tilde{V}_{\text{phase}}(f_x)|$ for w = 76 μm, 43 μm, and 33 μm, respectively. The strips are 5000-Å-thick gold lines on a fused-quartz substrate. The acoustic microscope operates at 50 MHz (λ = 30 μm) with F = 0.85, and the acoustic beam is focused on the surface of the fused-quartz substrate. The $|\tilde{V}_{\text{phase}}(f_x)|$ is plotted on a log scale. The weighting due to the imaging system response $|H(f_x)|$ all the way out to the resolution limit is very much in evidence. The linewidths estimated from the position of the first zero of $V_{\text{phase}}(f_x)$ are 76.3, 43.5, and 31.4 μm, respectively. They agree very well with the optically measured widths. The minor discrepancies are mainly due to the nonuniformity in the widths of the gold lines.

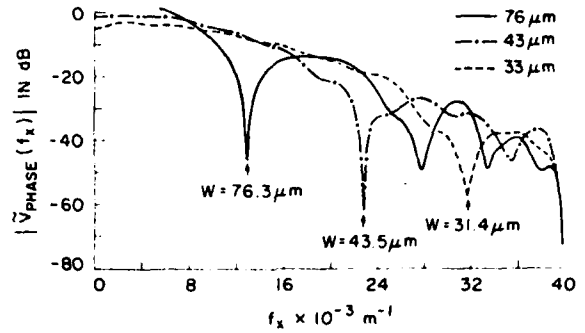

Fig. 7. Spectral responses of 5000-Å-thick gold lines on a fused-quartz substrate. The nominal linewidths are 76 μm, 43 μm, and 33 μm, respectively.

In addition, this Fourier transform approach is essentially insensitive to defocusing. It is obvious from (8) that

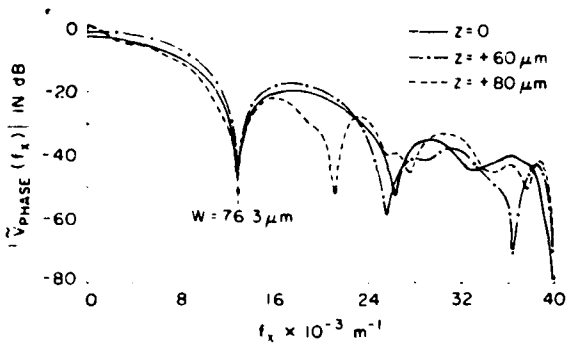

Fig. 8. Spectral responses of 2000-Å-thick 76-μm-wide chrome line on a fused quartz substrate at various defocusing distances: $z = 0$ μm, $+60$ μm, and $+80$ μm, respectively.

defocusing only changes the spectral response of the imaging system $H(f_x)$ slightly and does not introduce any new zeroes to nor does it affect the zeroes of $|\tilde{V}_{phase}(f_x)|$. Fig. 8 shows the experimental $|\tilde{V}_{phase}(f_x)|$ for a 2000-Å-thick and 76-μm-wide chrome line on fused quartz at various defocusing distances. The focus was located on the substrate, and 60 μm and 80 μm above the substrate, respectively. The locations of the first zero in all three cases are essentially coincident, giving a width estimate of 76.3 μm.

3) Independent Measurement of Velocity Perturbation and Topography: In conventional acoustic micrographs, surface topography and material property both contribute to contrast in the image, and their respective effects are generally indistinguishable from one another. With the topography tracking mechanism described in Section II-2 built into our phase measurement system, surface topography and material property change can essentially be obtained independent of each other.

Fig. 9(a) is the topographic line scan of an aluminum film step on glass with a nominal thickness of 5000 Å. The initial and trailing slow phase changes are due to the large spatial extent of the reference signal as it traverses the step, whereas the abrupt phase change is due to the focused beam as it crosses the step. Fig. 9(b) is the same profile on an expanded scale. The phase change caused by the step is 11.25°, which corresponds to a thickness of 4688 Å. With a limiting phase resolution of 0.1°, the ultimate height sensitivity of the system is about 50 Å.

Fig. 9(c) shows a velocity perturbation scan of the same sample. The phase change measured is 7.75°, corresponding to a velocity perturbation of 0.25 percent, which is in fair agreement with the theoretically calculated value of 0.21 percent.

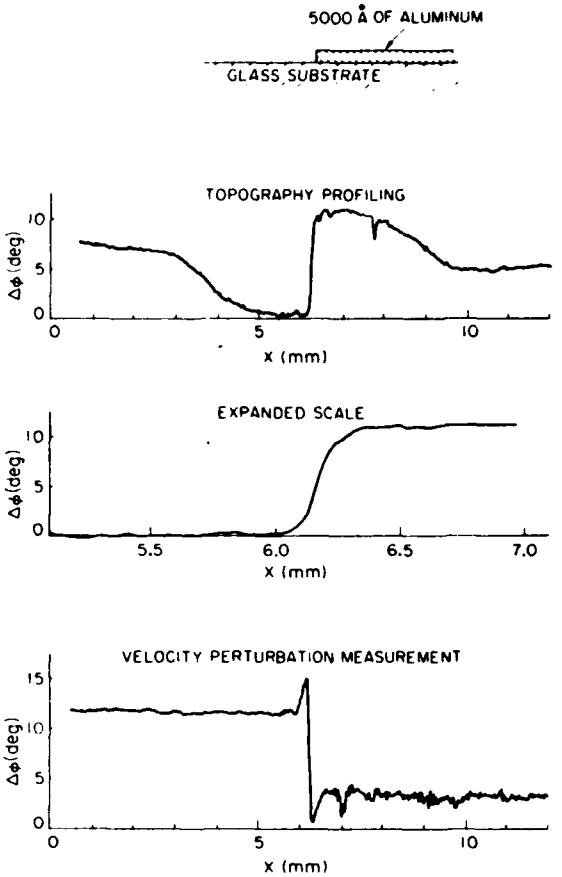

Fig. 9. Independent measurements of velocity perturbation and topography profile due to a 5000-Å aluminum film step. (a) Topography profile scan. (b) Topography profile scan on an expanded scale. (c) Velocity perturbation scn.

C. Reflectance by Inversion of Complex $V(z)$

It has been demonstrated that the reflectance function at a liquid–solid interface can be obtained by inverting the corresponding complex $V(z)$ data [10]. The principle motivation behind this endeavor is that one can obtain much more useful material property information from the reflectance function than the usual and rather limited treatment of measuring the periodicity of the nulls in the $V(z)$ curve to determine only the Rayleigh-wave velocity. The solid curves in Fig. 10 show the magnitude and the phase of the theoretical reflectance function of a water–fused-silica interface. The reflectance function contains information on the longitudinal and shear critical angles, and thus the velocities of propagation of the respective modes in fused silica. Also, the Rayleigh critical angle corresponds to the point at which the phase is π radians in the region, where the phase curve undergoes a rapid 2π radian change.

It can be shown that the relation between $V(z)$ and the reflectance function $R(\theta)$ is essentially one of Fourier transformation [10]. The inversion formula is given by

$$R(t) = \frac{\mathcal{F}\{V(u)\exp[j\pi u/\sin^2(\alpha/2)]\}}{[U_1^+(t)]^2 P^2(t)[1 - 2t\sin^2(\alpha/2)]} \quad (11)$$

where

$$u = \frac{4z\sin^2(\alpha/2)}{\lambda}$$

and

$$t = \frac{\sin^2(\theta/2)}{\sin^2(\alpha/2)}.$$

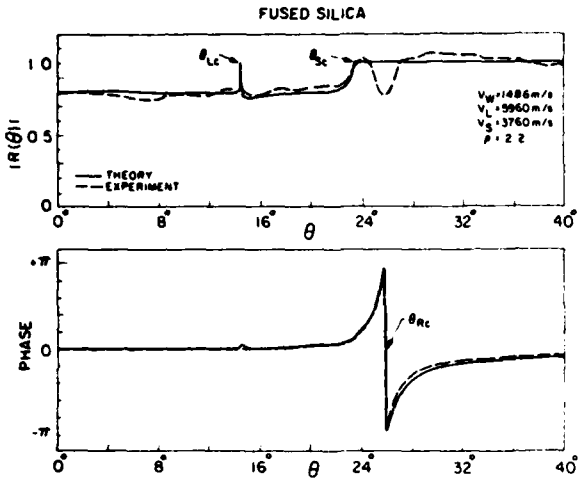

Fig. 10. Theoretical and experimental reflectance function for a water-fused-quartz interface obtained by inversion of the corresponding complex $V(z)$.

The α is the maximum half angle of the lens; θ is the incident angle with respect to the liquid–solid interface; and λ is the wavelength of the acoustic wave in the liquid medium. In addition, U_i^+ is the back focal plane illumination, and P is the pupil function of the lens. Generally these two lens parameters are not known, but $[U_i^+]^2\,P^2$ in the denominator of (11) can be calibrated by measuring the $V(z)$ for a material whose reflectance function has uniform amplitude and phase over the range of angular spectral components excited by the acoustic lens.

The $V(z)$ measurements were conducted at 10 MHz. A water–lead interface, in which the reflectance function is uniform in magnitude and phase out to $\theta = 40°$, was used to calibrate the $[U_i^+]^2\,P^2$ term. The experimental reflectance function of fused silica, obtained from the inversion procedure, is superposed on Fig. 10 in dashed lines. There is good agreement between theory and experiment in both magnitude and phase. The measured shear critical angle at $\theta = 23.5°$ and the Rayleigh critical angle at $\theta = 25.85°$ compare extremely well with theoretical values.

IV. Conclusion

We have demonstrated that phase information is a useful asset in acoustic microscopy. Phase can be used to provide sensitivity and information in surface material characterization unparalleled by amplitude-only measurement techniques. Most of the concepts described in this work have complete generality and can readily be used in other applications. In fact, many ideas presented in this work have been applied to a new scanning optical microscope [19] developed by Jungerman and Kino for surface topography measurement. In the optical case both the amplitude and the phase of the reflected beam can be measured as in the acoustic microscope. Preliminary results from the scanning optical microscope give further confirmation of most of the concepts put forth in this paper.

References

[1] H. K. Wickramasinghe and M. Hall, "Phase imaging with the scanning acoustic microscope," *Electron. Lett.*, vol. 12, pp. 637-638, Nov. 1976.

[2] C. C. Lee, C. S. Tsai, and X. Cheng, "Complete characterization of thin-and thick-film materials using wideband reflection acoustic microscopy," *IEEE Trans. Sonics Ultrason.*, vol. SU-32, no. 2, pp. 248-258, Mar. 1985

[3] S. D. Bennett and E. A. Ash, "Differential imaging with the acoustic microscope," *IEEE Trans. Sonics Ultrason.*, vol. SU-28, pp. 59-69, 1981.

[4] A. Atalar, "An angular spectrum approach to contrast in reflection acoustic microscopy," *J. Appl. Phys.*, vol. 49, pp. 5130-5139, Oct. 1978.

[5] H. K. Wickramasinghe, "Contrast and imaging performance in the scanning acoustic microscope," *J. Appl. Phys.*, vol. 50, pp. 664-668, Feb. 1979.

[6] R. D. Weglein, "Metrology and imaging in the acoustic microscope," in *Scanned Image Microscopy*, E.A. Ash, Ed. London: Academic, 1980.

[7] J. Kushibiki and N. Chubachi, "Material characterization by line-focus-beam acoustic microscopy," *IEEE Trans. Sonics Ultrason.*, vol. SU-32, no. 2, pp. 189-212, Mar. 1985.

[8] I. R. Smith, D. A. Sinclair, and H. K. Wickramasinghe, "Acoustic microscopy of elastic constants," in *Proc. 1980 IEEE Symp. Sonics Ultrason.*, Boston, MA, Oct. 1980.

[9] D. A. Sinclair and I. R. Smith, "Tissue characterization using acoustic microscopy," in *Acoustic Imaging*, vol. 12, E.A. Ash and C.R. Hill, Ed. New York: Plenum, 1982.

[10] J. A. Hildebrand, K. Liang, S. D. Bennett, "Fourier transform approach to material characterization with the acoustic microscope," *J. Appl. Phys.*, vol. 54, no. 12, pp. 7016-7019, Dec. 1983.

[11] B. A. Auld, *Acoustic Fields and Waves in Solids*, vol. 2. New York: John Wiley & Sons, 1973, p. 278.

[12] D. Husson and G. S. Kino, "A perturbation theory for acoustoelastic effects," *J. Appl. Phys.*, vol. 53, p. 7250, Nov. 1982.

[13] K. Liang, S. D. Bennett, B. T. Khuri-Yakub, and G. S. Kino, "Precision measurement of Rayleigh wave velocity perturbation," in "DARPA/AF Review of Progress in Quantitative NDE," La Jolla, CA, Aug. 1982.

[14] D. B. Marshall and B. R. Lawn, "Measurement of nonuniform distribution of residual stresses in tempered glass disks," *Glass Tech.*, vol. 19, no. 3, June 1978.

[15] K. Liang, S. D. Bennett, B. T. Khuri-Yakub, and G. S. Kino, "Precision measurement of Rayleigh wave velocity perturbation," *Appl. Phys. Lett.*, vol. 41, no. 12, pp. 1124-1126, 1982.

[16] R. A. Lemons, "Acoustic microscopy by mechanical scanning," Ph.D. Thesis, Stanford University, Stanford, CA, 1975.

[17] J. W. Goodman, *Introduction to Fourier Optics*. New York: McGraw-Hill, 1968.

[18] K. Liang, S. D. Bennett, and G. S. Kino, "Precision phase measurement for acoustic microscopy," to be submitted to *Rev. Sci. Inst.*

[19] R. L. Jungerman, P. C. D. Hobbs, and G. S. Kino, "Phase sensitive scanning optical microscope," submitted to *Appl. Phys. Lett.*, vol. 45, pp. 846-848, Oct. 1984.

Kenneth K. Liang, for a photograph and biography please see page 223 of the March 1985 issue of this TRANSACTIONS.

Simon D. Bennett (S'73-M'78), for a photograph and biography please see page 131 of this TRANSACTIONS.

Butros T. Khuri-Yakub, (S'70-M'76) for a photograph and biography please see page 224 of the March 1985 issue of this TRANSACTIONS.

Gordon S. Kino (S'52-A'54-SM'63-F'66), for a photograph and biography please see page 224 of the March 1985 issue of this TRANSACTIONS.

Material Characterization by the Inversion of $V(z)$

KENNETH K. LIANG, GORDON S. KINO, FELLOW, IEEE,
AND BUTRUS T. KHURI-YAKUB, MEMBER, IEEE

Abstract—**It is demonstrated that the reflectance function $R(\theta)$ of a liquid–solid interface can be obtained by inverting the complex $V(z)$ data collected with an acoustic microscope. The inversion algorithm is based on a nonparaxial formulation of the $V(z)$ integral, which establishes the Fourier transform relation between $R(\theta)$ and $V(z)$. Examples are given to show that with this measurement technique, the acoustic phase velocities of the propagating modes in the solid medium can easily be determined and material losses can be estimated. The same technique is also used for characterizing imaging performance of focused systems. Applications in thin-film measurement are also discussed.**

I. Introduction

A NEW TECHNIQUE for measuring and interpreting the acoustic material signature or the so-called $V(z)$ in acoustic microscopy will be presented in this paper. $V(z)$ refers to the variation of the normalized voltage output of an acoustic microscope as a function of the separation distance z between the focal point of the acoustic lens and the plane surface of a reflecting object [1]–[4]. This variation of voltage response with distance is characteristic of the material being examined and is an important source of contrast in acoustic micrographs. The $V(z)$ effect is a well-understood phenomenon, and various models have been put forth to explain how it is related to acoustic material properties [1], [2], [5], [6], [9]. So far, practical application revolves around the inverse process of determining acoustic-property-dependent parameters by interpreting selective features of the magnitude of the $V(z)$ function. For example, the leaky surface acoustic wave velocity can be obtained directly from the periodicity of the interference peaks and nulls of the magnitude of the $V(z)$ function in the negative z region [4]–[7], where the object surface is located between the focal point and the lens. Another approach involves the Fourier transform of the negative z portion of the magnitude of the $V(z)$ function in order to identify propagating modes at the liquid–solid interface and to determine their respective phase velocities [8].

The basic theory and experimental result of a more general Fourier transform technique, which utilizes both the magnitude and phase of the $V(z)$ function for material property characterization, will be given in this paper. The theoretical treatment is a combination of angular spectra and ray optics formalisms. It is carried out specifically for the case where the acoustic transducer is a spherical shell that radiates directly into the liquid coupling medium and hence forms a focusing lens by itself. An integral expression relating the complex $V(z)$ and the reflectance $R(\theta)$ of the liquid–solid specimen interface as a function of the angle θ between the direction of an incident plane wave and the normal to the interface surface is derived. It will be shown that by a suitable transformation of variables, $R(\theta)$ can be obtained by an inverse Fourier transform of $V(z)$.

The primary motivation behind this work is that the complex reflectance function $R(\theta)$ contains a wealth of readily available acoustic material property information. The solid curves in Fig. 7 show the theoretical magnitude and phase of the reflectance function of a water–fused-silica interface. The longitudinal and shear critical angles, θ_{Lc} and θ_{Sc}, show up as distinctive features on the magnitude curve and their locations give the propagation velocities of the respective modes directly. In addition the Rayleigh critical angle θ_{Rc} corresponds to the point where the phase curve becomes π in a region where it undergoes a rapid 2π radian change. Also, as will be shown in Section IV, the effect of loss in the solid medium can readily be observed in and estimated from the reflectance function $R(\theta)$. There are other potential areas of application involving film thickness measurement and the thin-film acoustic matching between two media of vastly different impedances, which will also be explored in Section IV.

II. Nonparaxial Formulation of the $V(z)$ Integral

The derivation of the relation between $V(z)$ and $R(\theta)$ in the literature [1], [2], [6], [9] can be classified into two general categories: those involving Fourier spectral decomposition [1], [2], [6] and those based on ray optic models [9]. The angular spectrum approach is more amenable to inversion since $V(z)$ can be expressed as an integral involving $R(\theta)$, and the integral can easily be manipulated to establish a Fourier transform relation between $V(z)$ and $R(\theta)$. The ray optic approach essentially regards $V(z)$ as the interference between a family of specularly reflected rays and a family of laterally displaced leaky surface acoustic wave rays. It is not complete in that it neglects the contributions from regions near the longitudinal and shear critical angles. Also, since it does not take diffraction into account, it is not valid near the focal plane. In addition, the ray optic formalism in the form usually given is incompatible with inversion procedures for finding $R(\theta)$. A common drawback to both kinds of formula-

Manuscript received November 1984; revised November 1984.
This work was supported by the Air Force Office of Scientific Research under Contract AFOSR-84-0063.
The authors are with Edward L. Ginzton Laboratory, W. W. Hansen Laboratories of Physics, Stanford University, Stanford, CA 94305, USA.

0018-9537/85/0300-0213$01.00 © 1985 IEEE

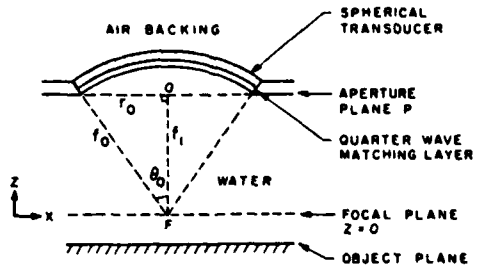

Fig. 1. Schematic of spherical focused transducer used in $V(z)$ measurements.

tions is that they both make use of the paraxial approximation.

An alternative hybrid formulation of the relation between $V(z)$ and $R(\theta)$ will be given in the following treatment. This approach combines features from the angular spectrum as well as the ray optic models and is valid for all z including the focal plane. Moreover, no paraxial assumption has to be made in its development. The special case of a focused spherical transducer radiating directly into water with no buffer medium, as shown in Fig. 1, is considered. The practical significance of this acoustic lens configuration will be discussed in Section IV. The elimination of the buffer rod simplifies the derivation. However, the final solution is valid for any lens configuration that generates a converging spherical wave, and can be generalized for use with other systems.

Using the notation given in Fig. 1, the potential or pressure field emitted by a transducer of diameter $2r_0$ is equivalent to that produced by a perfect converging spherical wave impinging on a circular aperture of radius r_0. All acoustic field terms will be assumed to vary as $\exp(j\omega t)$. Referring to the aperture plane P in Fig. 1, the potential field distribution in cylindrical coordinates is given by the relation

$$\phi(r) = P(r)\frac{\exp\left[jk\sqrt{r^2 + f_1^2}\right]}{\sqrt{r^2 + f_1^2}} \tag{1}$$

where $f_1 = \sqrt{f_0^2 - r_0^2}$ or $f_1 = f_0 \cos\theta$; f_0 is the focal length; θ_0 is the maximum half angle subtended by the aperture at the focus; and k is the propagation constant in the liquid medium. $P(r)$ is the pupil function of the lens, which in the most general case takes into account the nonuniform excitation of the transducer and any aberration effects. In the simplest case for an ideal lens

$$P(r) = \begin{cases} 1 & 0 < r < r_0 \\ 0 & r < r_0 \end{cases} \tag{2}$$

Making use of the circular symmetry of the field distribution, $\phi(r)$ can be decomposed into cylindrical radial waves of wave number k_r by applying the Hankel transform

$$A(k_r) = \int_0^\infty P(r)\frac{\exp\left[jk\sqrt{r^2 + f_1^2}\right]}{\sqrt{r^2 + f_1^2}} J_0(k_r r)\, r\, dr. \tag{3}$$

Here $k^2 = k_z^2 + k_r^2$. Since the transducer diameter is normally many wavelengths wide and the integrand is weighted by r, the contribution to the integral by $J_0(k_r r)$ comes mainly from regions where $k_r r$ is large. Therefore $A(k_r)$ can be approximated by replacing $J_0(k_r r)$ with its large argument asymptotic form

$$J_0(k_r r) \sim \frac{\exp\left[-j\left(k_r r - \frac{\pi}{4}\right)\right] + \exp\left[j\left(k_r r - \frac{\pi}{4}\right)\right]}{\sqrt{2\pi k_r r}}. \tag{4}$$

Thus, it follows that

$$A(k_r) \sim \int_0^\infty P(r)\frac{\exp[j\psi_1(r)] + \exp[j\psi_2(r)]}{\sqrt{2\pi k_r r(r^2 + f_1^2)}}\, r\, dr \tag{5}$$

where

$$\psi_1(r) = \left(k\sqrt{r^2 + f_1^2} - k_r r + \frac{\pi}{4}\right)$$

$$\psi_2(r) = \left(k\sqrt{r^2 + f_1^2} + k_r r - \frac{\pi}{4}\right).$$

The method of stationary phase will now be applied to evaluate (5) [10]. Consider the phase of the first term of the integrand $\psi_1(r)$. The contribution to the integral comes from the region near where $\psi_1'(r) = 0$

$$\psi_1'(r) = \frac{kr}{\sqrt{r^2 + f_1^2}} - k_r = 0$$

or where $r = r'$

$$r' = \frac{k_r}{\sqrt{k^2 - k_r^2}} f_1 = \frac{k_r}{k_z} f_1. \tag{6}$$

Note that r' is positive in this case.

Next, consider the phase of the second term of the integrand $\psi_2(r)$. Setting $\psi_2'(r)$ to zero yields the result

$$\frac{kr'}{\sqrt{r'^2 + f_1^2}} = -k_r \tag{7}$$

which implies that r' is negative. Since in a cylindrical coordinate system r is always positive, there is no contribution to $A(k_r)$ from the second term of the asymptotic form of $J_0(k_r r)$.

Equation (5) therefore becomes

$$A(k_r) = \left(\frac{2\pi}{|\psi_1''(r')|}\right)^{1/2} P(r')\frac{\exp[jk\psi_1(r')]}{\sqrt{2\pi k_r r'(r'^2 + f_1^2)}}\frac{k_r}{k_z} f_1 \tag{8}$$

where r' is given by (6) and

$$\psi_1''(r') = \frac{k}{\sqrt{r'^2 + f_1^2}} - \frac{kr'^2}{(r'^2 + f_1^2)^{3/2}} = \frac{k_z^3}{k^2 f_1}.$$

Substituting (6) into (8) gives the result

$$A(k_r) = P(k_r)\, k \exp[jk_z f_1]/k_z \tag{9}$$

where

$$k_z = \sqrt{k^2 - k_r^2}. \tag{10}$$

To find the corresponding angular spectrum at a plane of distance $z + f_1$ from the aperture plane P, each spectral component is multiplied by the propagation factor $\exp[-jk_z(z + f_1)]$. For instance, at the focal plane $z = 0$

$$A(k_r; 0) = P(k_r)\, k/k_z \tag{11}$$

which simply means that with an ideal pupil function all angular spectral components arrive in phase at the focal point. In general, for any arbitrary z

$$A(k_r; z) = P(k_r)\, k \exp[-jk_z z]/k_z. \tag{12}$$

Suppose the plane reflector specimen is placed at z, and the reflectance function of the liquid-specimen interface is $R(k_r)$. The reflected angular spectrum at z is

$$B(k_r; z) = R(k_r)\, A(k_r; z). \tag{13}$$

The reciprocity principle of Kino and Auld given in the Appendix is employed to find the normalized voltage response $V(z)$ of the focused transducer to the reflected wave in which the spectrum is given by (13). $V(z)$ is equal to the scattering coefficient s_{11}

$$V(z) = s_{11} = \frac{j}{2} \frac{\int (\phi^r u_z^i - \phi^i u_z^r)\, dS}{\int \phi^i u_z^{i*}\, dS} \tag{14}$$

where u_z is the normal displacement at the liquid-solid interface, and the integration is evaluated over the same. The superscripts i and r designate the incident and the reflected fields respectively, and

$$u_z^i = \frac{\partial \phi^i}{\partial z}$$

$$u_z^r = \frac{\partial \phi^r}{\partial z}. \tag{15}$$

For the circularly symmetric incident and reflected radial wave components, the Hankel transforms of the u_z components are

$$U_z^i(k_r) = -jk_z A(k_r)$$

$$U_z^r(k_r) = jk_z B(k_r). \tag{16}$$

By applying Parseval's Theorem and substituting in (16), (14) can be written in the form

$$V(z) = \frac{\int A(k_r; z)\, B(k_r; z)\, k_z k_r\, dk_r}{\int A(k_r; z)\, A^*(k_r; z)\, k_z k_r\, dk_r}. \tag{17}$$

Substituting (12) and (13) into (17), the final result is

$$V(z) = \frac{\int P^2(k_r)\, R(k_r) \dfrac{\exp[-j2k_z z]}{k_z} k_r\, dk_r}{\int \dfrac{P^2(k_r)}{k_z} k_r\, dk_r} \tag{18}$$

By making the following substitution of variables, a comparison can be made between (18) and Atalar's paraxial angular spectrum formulation of the $V(z)$ integral [1]. Let

$$k_r/k = r/f_0. \tag{19}$$

Equation (18) can be written in the form

$$V(z) = \frac{\int P^2(r/f_0)\, R(r/f_0) \dfrac{\exp[-j2kz\sqrt{1 - (r/f_0)^2}]}{\sqrt{1 - (r/f_0)^2}} r\, dr}{\int P^2(r/f_0) \dfrac{r\, dr}{\sqrt{1 - (r/f_0)^2}}} \tag{20}$$

which differs from Atalar's solution by the factor $1/\sqrt{1 - (r/f_0)^2}$ in the denominator of each integrand. In the limit of the paraxial approximation where $(r/f_0)^2$ is assumed to be small, this additional factor tends to unity, and (18) becomes the expression derived by Atalar.

III. Fourier Transform Relation Between $V(z)$ and $R(\theta)$

The possibility of obtaining $R(\theta)$ by inverting $V(z)$ has been alluded to in optical microscopy [11], and the inversion has been demonstrated in acoustic microscopy [12] based on Atalar's paraxial $V(z)$ integral. The Fourier transform relation between $V(z)$ and $R(\theta)$ for the nonparaxial formulation given in (18) can be established as follows. Since $k_z^2 = k^2 - k_r^2$, it follows that

$$k_z dk_z = -k_r\, dk_r. \tag{21}$$

Equation (18) becomes

$$V(z) = C \int_k^{k\cos\theta_0} P^2(k_z) R(k_z) \exp(-j2k_z z)\, dk_z \tag{22}$$

where C is the normalization factor given by

$$C = \left[\int_k^{k\cos\theta_0} P^2(k_z)\, dk_z\right]^{-1} \tag{23}$$

Noting that $k_z = k\cos\theta$, where $k = 2\pi/\lambda$, and making the following change of variables

$$u = \frac{z}{\lambda}$$

$$t = 2\cos\theta \tag{24}$$

we obtain the result

$$V(u) = C \int_2^{2\cos\theta_0} P^2(t)\, R(t) \exp(-j2\pi ut)\, dt. \tag{25}$$

In short-hand notation

$$V(u) = \mathfrak{F}\{P^2(t)\, R(t)\} \tag{26}$$

where $\mathfrak{F}\{\ \}$ denotes the Fourier transform. The inversion to obtain $R(t)$ is given by

$$R(t) = \begin{cases} \dfrac{\mathfrak{F}^{-1}\{V(u)\}}{P^2(t)}, & 2 > t > 2\cos\theta_0 \\ 0, & \text{otherwise.} \end{cases} \tag{27}$$

Note that $R(t)$ is only determined for the angular range of insonification covered by the pupil function of the lens. In general $P(t)$ is not known *a priori*. However, $P^2(t)$ can conveniently be calibrated by inverting the $V(z)$ function for a liquid–solid interface in which the reflectance has uniform magnitude and phase over the angular extent of the lens pupil function. In particular, if a perfectly reflecting surface with $R(t) \equiv 1$ is used

$$P^2(t) = \mathfrak{F}^{-1}\{V_0(u)\} \tag{28}$$

where $V_0(u)$ is the $V(z)$ of the "ideal" reflector.

This inversion approach to material characterization is different in that it requires the measurement of $V(z)$ in both amplitude and phase whereas previous work [1]–[8] utilized only the amplitude or intensity of $V(z)$. It is generally not trivial to conduct high-accuracy phase measurement in acoustic microscopy. A special phase-measurement system [13] has been developed to enable the precise acquisition of phase data and the subsequent experimental demonstration of the inversion technique.

It is interesting at this point to examine the range resolution of a confocal imaging system such as the reflection acoustic microscope for an ideal plane reflector; i.e., $R(\theta) \equiv 1$. Assuming an ideal lens pupil function of the form in (2), the voltage response of the acoustic microscope as a function of defocusing distance can be calculated from (25) to be

$$V(u) = C \int_2^{2\cos\theta_0} \exp\,[-j2\pi u t]\, dt$$

or

$$V(u) = -C \exp\,[-j\pi u(1 + \cos\theta_0)] \cdot \operatorname{sinc}\,[2u(1 - \cos\theta_0)]. \tag{29}$$

The 3-dB point of $|V(u)|$ is given by the relation

$$2(1 - \cos\theta_0)\, u_{3\text{dB}} = 0.45\pi$$

or

$$z_{3\text{dB}} = \frac{0.225\lambda}{1 - \cos\theta_0}$$

Therefore the 3-dB range resolution or the focal depth for a plane reflector is

$$\Delta z_{3\text{dB}} = \frac{0.45\lambda}{1 - \cos\theta_0}. \tag{30}$$

IV. Experimental Results

In the $V(z)$ measurement a special acoustic transducer is used. The piezoelectric element is a spherical shell with an air backing and a quarter-wave matching layer on the front face. The transducer radiates directly into water, and thus forms an aberration-free spherical lens that focuses the emitted acoustic beam into a diffraction-limited spot at the center of curvature of the transducer. This acoustic lens configuration is advantageous for $V(z)$ measurements because the elimination of the buffer rod removes the systematic noise due to reverberations inside the buffer rod that tend to overlap in time with the reflected signal from the object. With such a construction the acoustic lens can be translated over a wide range of z to collect $V(z)$ data in an essentially noise-free environment. The maximum limit to the vertical movement is imposed by how far the lens can be moved towards the specimen. The problem with multiple echoes in the water path between the transducer and the specimen is overcome by exciting the transducer with a short tone burst and time-gating the first arrival return signal.

Two transducers of this type with $F/1$ and $F/0.7$ apertures, respectively, are used in the experiment. The radius of curvature or focal length f_0 is 16 mm in both cases. From geometric considerations, the maximum possible negative defocusing distance is given by

$$z_{\min} = -f_1 = -f_0\sqrt{1 - 1/(2F)^2} \tag{31}$$

where F is the f-number of the lens. For the $F/0.7$ lens $|z_{\min}| = 11.2$ mm, and for the $F/1$ lens $|z_{\min}| = 13.9$ mm. The importance of $z_{\min}$ will be discussed in Section V.

Both transducers have a fundamental frequency of approximately 3 MHz. For $V(z)$ measurements, they are operated at the third harmonic frequency of 10.17 MHz for the $F/0.7$ lens and 10.7 MHz for the $F/1$ lens. Many practical considerations go into this particular choice of operating frequency range. The inversion formalism is most conveniently applied to a lossless liquid medium. The loss in water is essentially negligible at 10 MHz and so satisfies this requirement. Moreover, the wavelength in water of about 150 μm is sufficiently large to render any irregularity and instability in the vertical translation mechanism insignificant. By the same token the measurement is less subject to error as a result of surface finish imperfections in the sample.

A lead sample is used to calibrate the pupil function of the lens. With a longitudinal velocity $v_L = 2200$ m/s, the longitudinal critical angle for the water–lead interface occurs at $\theta = 43^0$, as illustrated in the theoretical plot in Fig. 2. The reflectance function is essentially flat in both amplitude and phase from $\theta = 0^0$ to 40^0. Fig. 3 shows the magnitude and phase of the $V(z)$ for lead from $z = -8$ mm to $z = +8$ mm. The phase displayed is in fact that of $V(z)$ with the linear phase term $2kz$ subtracted out. Fig. 4 shows $P^2(\theta)$ for the $F/0.7$ lens obtained by inverting the experimental $V(z)$ for lead. The pupil function is not uniform in either magnitude or phase especially near the edge

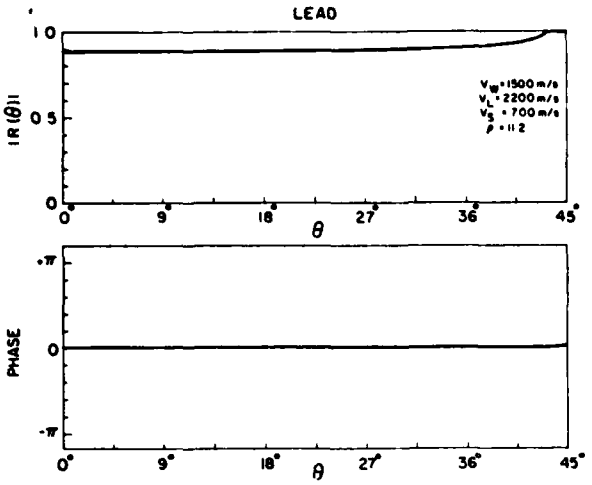

Fig. 2. Magnitude and phase of the theoretical reflectance function of a water–lead interface.

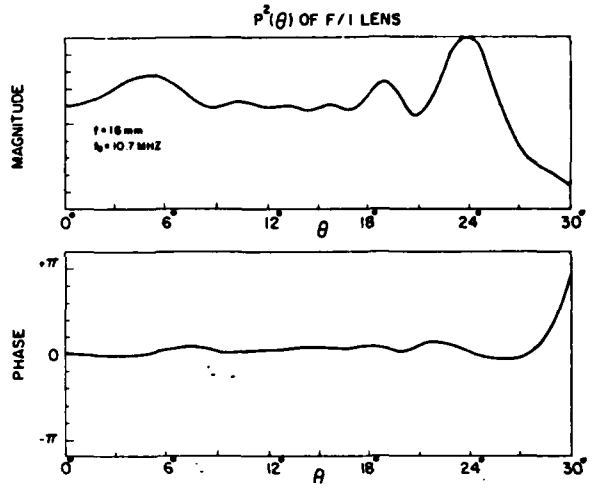

Fig. 5. Calibration of the pupil function of the 10.7 MHz $F/1$ focused transducer.

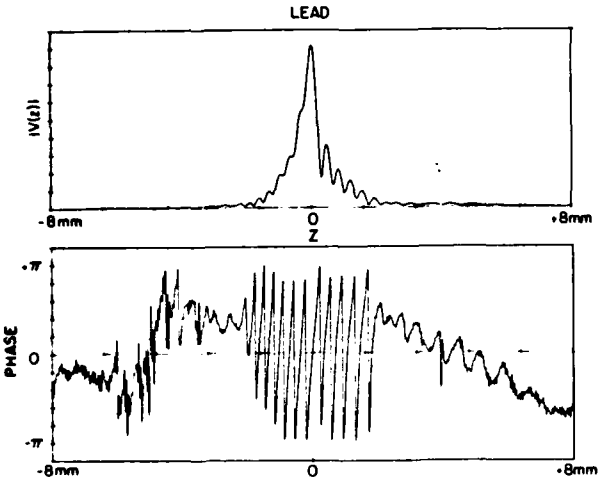

Fig. 3. Experimental $V(z)$ of a water/lead interface measured with a 10.17 MHz $F/0.7$ focused transducer.

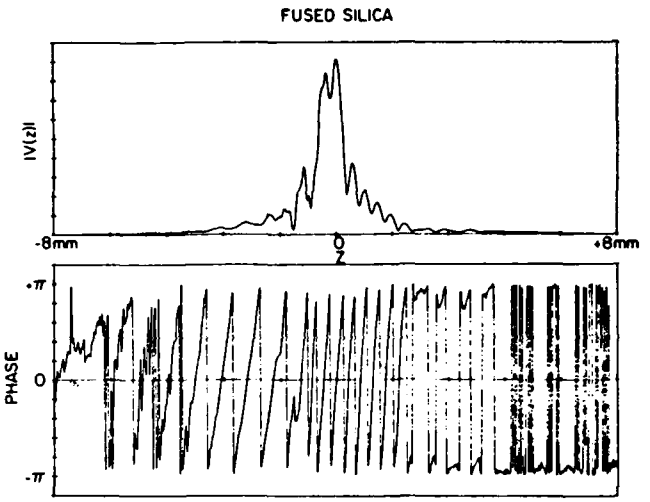

Fig. 6. Experimental $V(z)$ of water–fused-silica interface at 10.17 MHz.

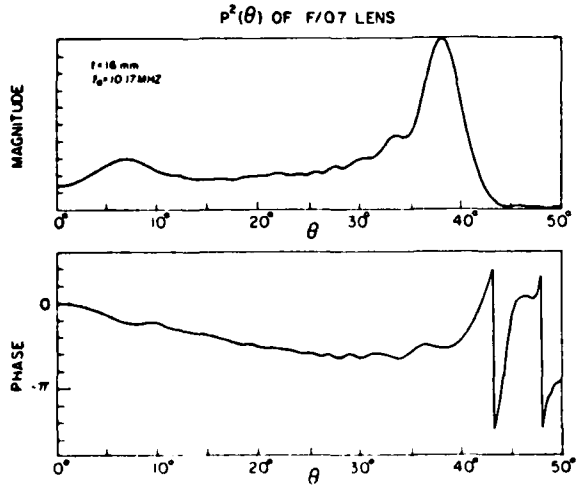

Fig. 4. Calibration of the pupil function of the 10.17 MHz $F/0.7$ focused transducer.

of the lens where an accentuated peak occurs around $\theta = 38^0$. Premature roll-off of the lens angular response is also evident, and the illumination from the outer periphery of the lens is weak. The experimental $P^2(\theta)$ for the $F/1$ lens shown in Fig. 5 exhibits a similar, though less pronounced, peak at $\theta = 23.5^0$. These anomalies in the lens response are due to nonuniformity in the thickness of the matching layer as a result of difficulties encountered in the fabrication process [23].

It should be pointed out that this simple calibration procedure can be utilized as an alternative method for characterizing and predicting imaging performance of focused systems. Instead of measuring the point spread function at the focal plane as is the case in most conventional techniques, the characterization is done in terms of the pupil function illumination. This approach has direct relevance and application in the fabrication of spherical acoustic lenses, where the sphericity of the lens and the uniformity of the matching layer are of primary concern.

Fused Silica

The experimental $V(z)$ for fused silica is shown in Fig. 6. Fig. 7 displays the corresponding $R(\theta)$, which is obtained by inverting the $V(z)$ and then dividing out the calibrated value of $P^2(\theta)$ for the $F/0.7$ lens. The theoretical

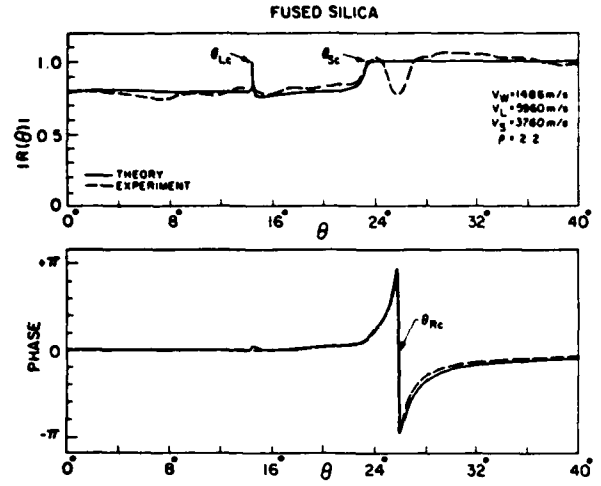

Fig. 7. Comparison of the theoretical and experimental reflectance function for a water-fused-silica interface.

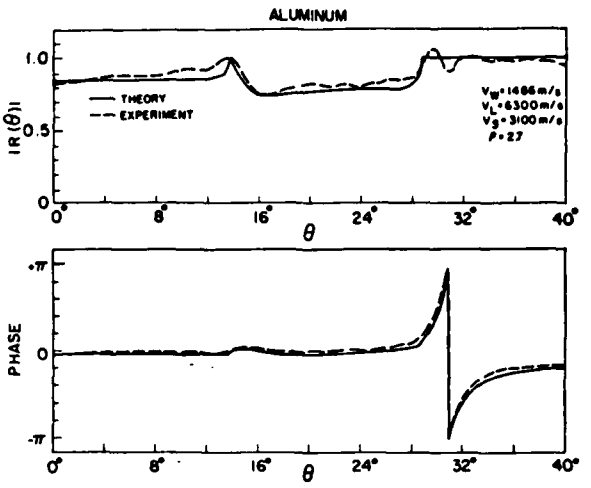

Fig. 9. Comparison of the theoretical and experimental reflectance function for a water-aluminum interface.

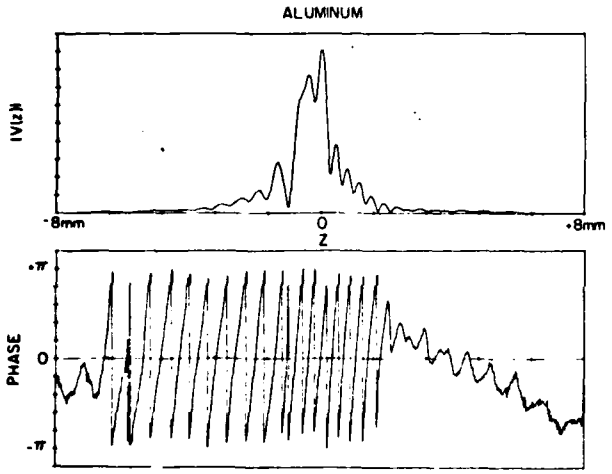

Fig. 8. Experimental $V(z)$ of a water-aluminum interface at 10.17 MHz.

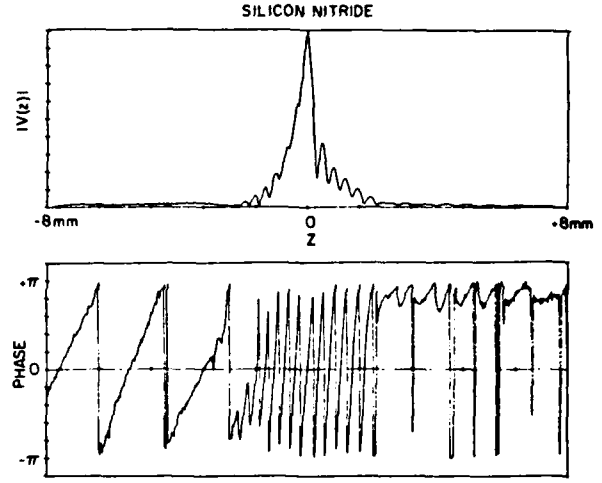

Fig. 10. Experimental $V(z)$ of a water-silicon-nitride interface at 10.17 MHz

reflectance is also shown for comparison. A value of v_w = 1486 m/s is used as the velocity in water in the inversion algorithm. There is good general agreement between theory and experiment in both magnitude and phase. The experimental shear critical angle at $\theta = 23.5^0$ and the Rayleigh critical angle at $\theta = 25.85^0$ compare extremely well with the theoretical values. The longitudinal critical angle is not reproduced in the experimental result due to the problem of degradation angular resolution caused by the spatial truncation of the $V(z)$ data. This difficulty will be elaborated upon in Section V.

Aluminum

Figs. 8 and 9 are the $V(z)$ and $R(\theta)$ for aluminum. Again the agreement between theory and experiment is very good. The longitudinal and shear critical angles show up clearly in the experimental result, in this case at $\theta = 13.64^0$ and $\theta = 28.64^0$, respectively. The Rayleigh critical angle is located at $\theta = 30.86^0$, which gives a phase velocity of 2897 m/s for the leaky surface acoustic wave.

Silicon Nitride

Figs. 10 and 11 show the $V(z)$ and $R(\theta)$ for hot-pressed silicon nitride, which is a ceramic material with high acoustic velocity. All the critical angles occur at low-incidence angles, and only the Rayleigh critical angle at $\theta = 15.0°$ is reproduced in the experimental phase curve. It should be noted that the dip in the experimental magnitude curve for silicon nitride and smaller dips at the Rayleigh critical angle in Figs. 7 and 9 for fused quartz and aluminum are only an artifact introduced by the spatial truncation of the experimental $V(z)$ data. Similar dips can occur as a result of shear loss in the solid, an effect widely known as the Rayleigh critical-angle phenomenon [14], [15]. However, the acoustic losses in all three materials are known to be negligible at 10 MHz, therefore the experimental dips cannot possibly be associated with loss. As will be shown in the following section on error analysis, this experimental artifact is well understood and in some cases can be alleviated. Hence, the inversion tech-

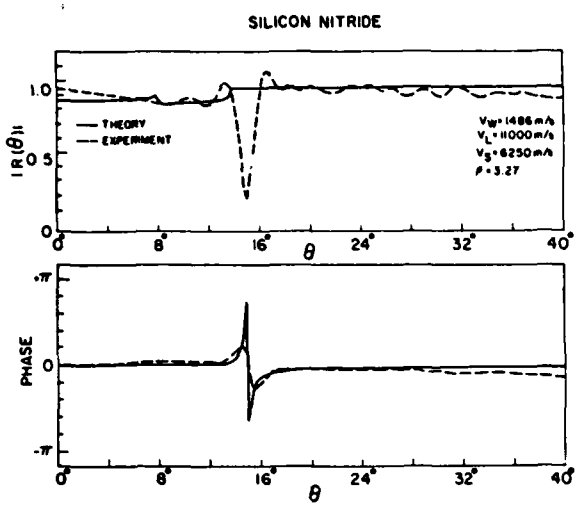

Fig. 11. Comparison of the theoretical and experimental reflectance function for the water-silicon-nitride interface.

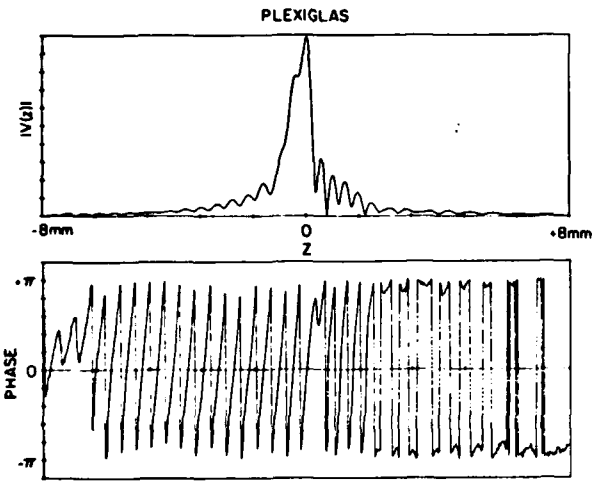

Fig. 12. Experimental $V(z)$ of a water-Plexiglas interface at 10.17 MHz.

nique does not preclude the characterization of such acoustic properties as shear loss, temperature dependence of the Rayleigh-wave velocity, and various contributing factors to the Rayleigh critical-angle phenomenon.

Plexiglas

Figs. 12 and 13 are the $V(z)$ and $R(\theta)$, respectively, for plexiglas or lucite, a low-acoustic velocity and high loss material. This example illustrates how material loss can be determined. The longitudinal critical angle is located at $\theta = 32.7°$, which corresponds to a longitudinal wave velocity of 2750 m/s. The magnitude of the reflectance peaks at 0.7 rather than one, as it would be for a lossless substrate. The amount of diminution of the peak level depends on the loss for the longitudinal mode. The theoretical curve is fitted to the experimental one by varying the longitudinal loss factor Q_L. The Q_L is found to be about 50, which translates into an attenuation coefficient of 232 Np/m or 20 dB/cm at 10 MHz, which agrees well with other published values [16].

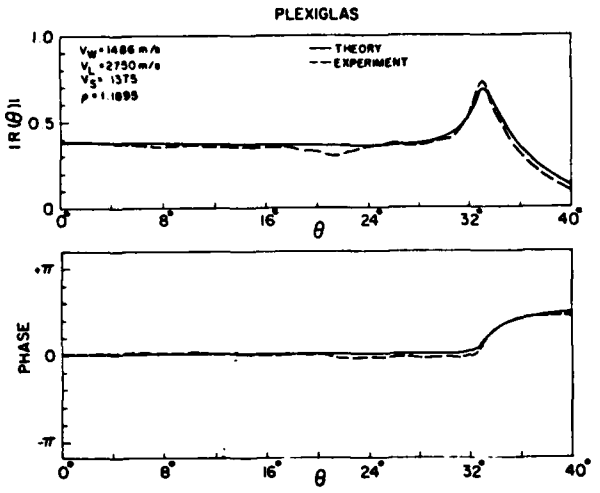

Fig. 13. Comparison of the theoretical and experimental reflectance function for a water-Plexiglas interface.

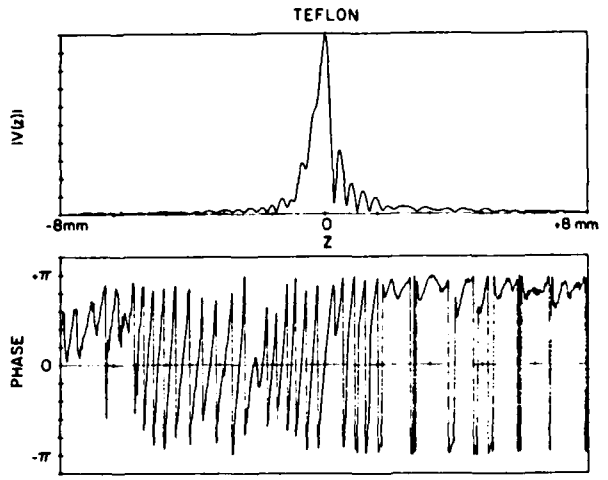

Fig. 14. Experimental $V(z)$ of a water-teflon interface at 10.17 MHz.

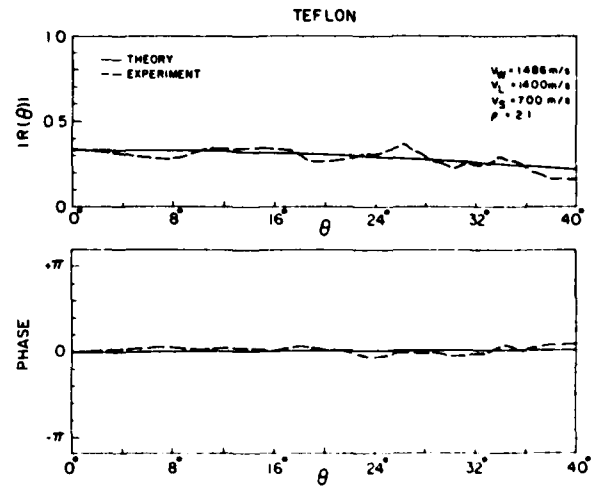

Fig. 15. Comparison of the theoretical and experimental reflectance function for a water-teflon interface.

Teflon

$V(z)$ and $R(\theta)$ for teflon are displayed in Figs. 14 and 15. As expected no critical angle is observed, since teflon

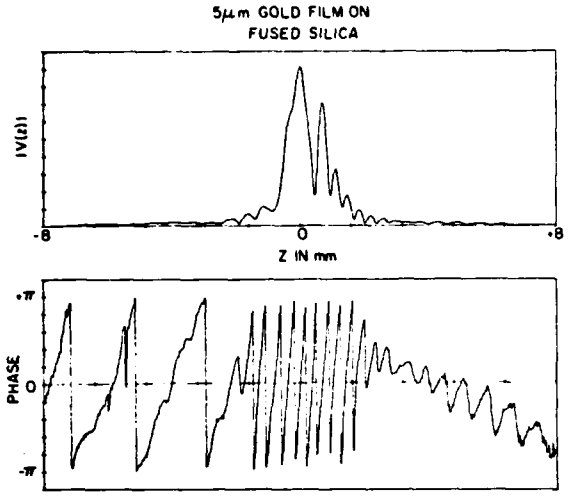

Fig. 16. Experimental $V(z)$ of a water and 5-μm gold film on a fused-silica interface at 10.7 MHz.

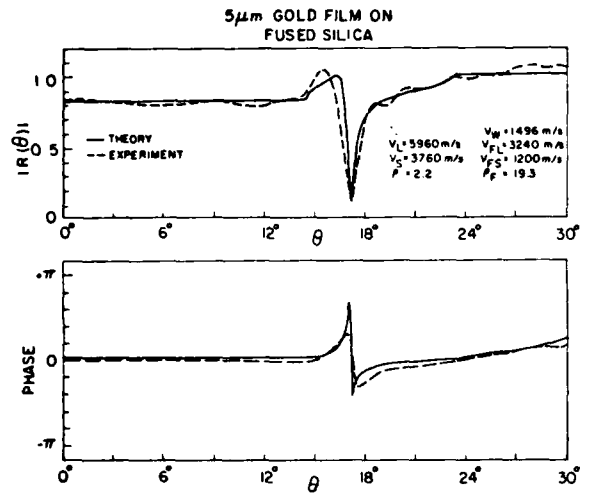

Fig. 17. Comparison of the theoretical and experimental reflectance function for a water and 5-μm gold film on a fused-silica interface.

has a longitudinal velocity of 1400 m/s, which is lower than that of water.

Thin-Film Measurement

The following example demonstrates the potential application of acoustic microscopy in thin-film characterization and also confirms a thin-film matching phenomenon predicted by numerical computation. The thin-film structure used in this example is a 5-μm-thick gold film deposited on a fused-silica substrate. At 10 MHz the thickness of the gold film corresponds to about 1.5 percent of the longitudinal wavelength. Figs. 16 and 17 are the plots of $V(z)$ and $R(\theta)$, respectively. The agreement with the theoretically generated $R(\theta)$ is good. $R(\theta)$ shows a null at $\theta = 17.23°$, an angle between the longitudinal and shear critical angles of the fused silica substrate. Physically this means that the incident longitudinal mode in water couples very strongly into a bulk propagating mode in the fused silica substrate. The physics of this coupling is not well understood, but it is believed that the longitudinal wave in water converts in the gold film to a leaky Sezawa wave, which leaks into the fused silica substrate in the form of a propagating shear wave. The coupling efficiency and the angle of incidence, at which maximum transmission occurs, have been shown to be functions of the film thickness by numerical analysis. Thus by measuring the reflectance, one can get information about the film thickness. The experimental demonstration of this thin-film phenomenon also opens up the possibility of using the thin-film matching technique in the design of acoustic transducers to improve the transmission efficiency between two media with vastly different acoustic impedances.

V. Error Analysis

The introduction of experimental artifacts in the experimental $R(\theta)$ due to the spatial truncation of the $V(z)$ curve is treated in this section. This problem arises because of the finite distance over which $V(z)$ data can be collected. Equation (26) shows that $V(u)$ and $[P^2(t)R(t)]$ form a Fourier-transform pair. It can be shown by Fourier-transform theory that since $[P^2(t)R(t)]$ is finite in the t domain, $V(u)$ has to be infinite in the u domain. Experimentally $V(z)$ can only be obtained for some finite-width data window. Therefore the actual waveform $V'(z)$ used in the inversion is a truncated version of $V(u)$. Thus

$$V'(u) = V(u) \text{ rect } (u/D) \tag{32}$$

where $u = z/\lambda$, and D is the width of the data window defined in terms of the number of wavelengths in water. Noting that multiplication in the u domain corresponds to convolution in the transform domain t, the reflectance function obtained by inverting $V'(u)$ is

$$[P^2(t)R(t)]' = [P^2(t)\ R(t)]^* D \text{ sinc } (Dt) \tag{33}$$

where * denotes convolution.

The effects of the convolution between the reflectance function and the waveform sinc (Dt) are twofold. First, the angular resolution in the t domain is degraded. Second, because of the oscillatory nature of sinc (Dt), sharp features in $P^2(t)R(t)$ tend to generate ripples in the resulting $[P^2(t)R(t)]'$. The resolution degradation effect can be estimated as follows. The full width between zeroes of the main lobe of sinc (Dt) is

$$\Delta t = 2/D. \tag{34}$$

The Δt is essentially the transition width of the response to a sharp step in $P^2(t)R(t)$ and hence can be regarded as the worst case resolution in t. Using the relation $t = 2 \cos \theta$ given in (24), we get the following expression for the angular resolution in terms of the angle of incidence θ

$$\Delta\theta = \frac{\Delta t}{2 \sin \theta}. \tag{35}$$

Combining (34) and (35), the resolution in θ in terms of the width of the data window D is found to be

$$\Delta\theta = \frac{1}{D \sin \theta}. \tag{36}$$

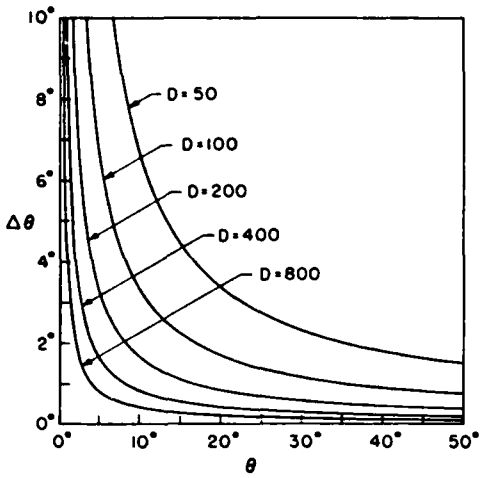

Fig. 18. Variation of angular resolution degradation as a function of the incident angle and the normalized data window width D.

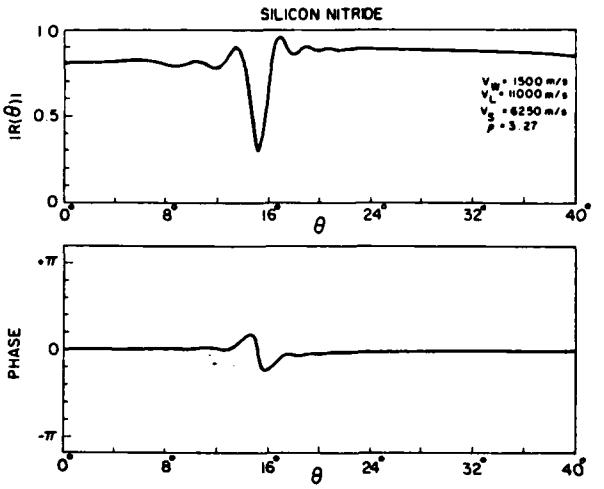

Fig. 19. Simulated reflectance function of a water-silicon nitride interface obtained by inverting spatially truncation $V(z)$ data.

Equation (36) is plotted in Fig. 18 with D as a parameter. The data window D used in the experiment is about 100. This implies angular resolution of about 3.3° at θ = 10°, 1.7° at θ = 20°, and 1.1° at θ = 30°. The experimental reflectance of silicon nitride in Fig. 11 is a pathological example of the degradation effect of this angular resolution. The Rayleigh critical angle occurs at a low value of θ = 15.0° and in the vicinity of this angle, the magnitude of the reflectance is unity but the phase goes through a rapid 2π radian change over a 2° angular range. The net result of the convolution with sinc (Dt) is a sharp dip in the magnitude of the experimental reflectance and a smoothing of the phase curve near the Rayleigh critical angle. The effect of the convolution is much less serious at angles of high incidence as shown in Fig. 18 and as evidenced by the experimental $R(\theta)$'s of fused silica and aluminum, where only a slight dip occurs in the reflectance magnitude.

A computer simulation has been carried out where the theoretical $R(\theta)$ for silicon nitride is used to generate the $V(z)$, which is truncated and then inverted in an identical manner to the experimental data. The result is shown in Fig. 19. The simulated $R(\theta)$ exhibits exactly the same behavior in both amplitude and phase as the experimental one in Fig. 11.

The locations of the critical angles are generally used to determine the phase velocities of propagating modes, which are given by

$$v_* = v_W/\sin\theta_{*_c}$$

where v_W is the velocity in water; the asterisk stands for L (longitudinal), S (shear), or R (Rayleigh); and the subscript c denotes critical angle. The percentage error in the estimation of v_* as a consequence of the truncation of $V(z)$ can be shown to be

$$\left|\frac{\Delta v_*}{v_*}\right| = \frac{1}{2}\frac{\cos\theta_{*_c}}{\sin\theta_{*_c}}\Delta\theta_{*_c} = \frac{1}{2}\frac{\cos\theta}{D\sin^2\theta}. \tag{37}$$

Equation (37) is plotted in Fig. 20 with D as a parameter.

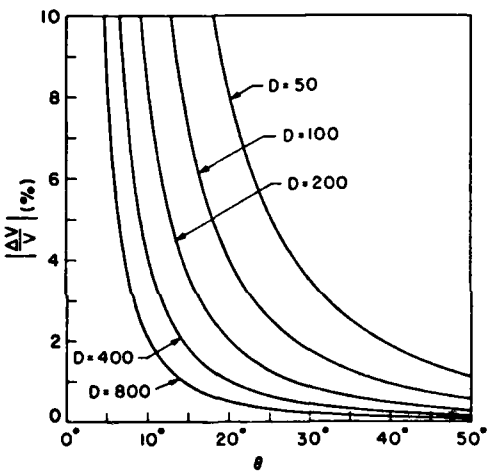

Fig. 20. Phase velocity estimation error as a function of angle of incidence due to degradation of the angular resolution.

The error decreases drastically with increasing incidence and increasing D. For D = 100, $|\Delta v_*/v_*|$ is four percent at θ = 20° and 1.75 percent at θ = 30°. One should bear in mind that (37) represents the worst-case estimation, and the actual error could well be substantially smaller, especially for the Rayleigh critical angle θ_{R_c}. The determination of θ_{R_c} involves locating the point, where the phase of $R(\theta)$ is π radians. Around θ_{R_c} the magnitude of the reflectance function for a lossless material is constant while the phase Ψ can be shown to have the form [9]

$$\tan\Psi = 2\frac{k_r - k\sin\theta_{R_c}}{\alpha} \tag{38}$$

where α is the leak rate of the Rayleigh wave. The phase function Ψ is the antisymmetric in k_r about $\Psi = \pi$ around the point $k_r = k\sin\theta_{R_c}$. It is similarly antisymmetric in k_z or t in the neighborhood of $k_z = k\cos\theta_{R_c}$. Since the sinc function with which $[P^2(t)R(t)]$ is convolved is symmetric, the phase function Ψ around the Rayleigh critical angle remains essentially unchanged by the convolution,

provided that the width of the main lobe of the sinc function Δt is smaller than the transition width of Ψ through the Rayleigh critical-angle region. For example, in the case of fused silica and aluminum, the respective leaky surface-acoustic-wave velocities calculated from the experimental phase curve are almost identical to those predicted by theory.

The second problem associated with the generation of ripples can be partly remedied, though with some further loss in angular resolution, by applying a smooth apodization function for the $V(z)$ data before inversion takes place. The apodization function used in processing the $V(z)$ data is

$$a(u) = \frac{\sin^2 (\pi u/D)}{n + \sin^2 (\pi u/D)} \tag{38}$$

where n is a free parameter for adjusting the tapering characteristics of the apodization. The $n = 0.1$ is used to process the experimental data shown here. The resulting apodization essentially leaves the data in the center of the window unchanged, but it behaves much like Hamming weighting at the edges of the data window.

The obvious solution to both the resolution degradation and ripple problems is to increase the data window width D of $V'(u)$. Equation (31) shows that this can be realized by increasing the radius of curvature f_0 or reducing the aperture size or both. Also D can be increased by increasing the frequency of operation. For silicon nitride, $R(\theta)$ can be reproduced much more faithfully if $\Delta\theta$ is reduced to $\frac{1}{3}°$, which can be achieved by using an $F/1.5$ lens with a focal length of 32 mm operating at 20 MHz.

Another important source of error is in the estimation of the velocity of water. Since

$$u = z/\lambda = zf/v$$

then

$$du = -\frac{zf}{v^2} dv = -u\, dv/v. \tag{39}$$

Suppose the wrong velocity is used in the inversion. In (25) this is equivalent to changing u to

$$u' = u + \Delta u = u(1 - \Delta v/v). \tag{40}$$

The resulting inversion is given by

$$[P^2(t)R(t)]' = \int V(u) \exp [j2\pi u(1 - \Delta v/v)t]\, du$$

or

$$[P^2(t)R(t)]' = P^2R[(1 - \Delta v/v)t]. \tag{41}$$

Therefore using an erroneous v results in a stretched reflectance function in t. Since the velocity of water has a large temperature coefficient, 4 m/s per °C, this error can be significant. It may cause enough misalignment of the inversions of the sample material of interest and the calibration lead sample to have a serious effect on the determination of $R(\theta)$. From (35) and (41) it can easily be shown that the shift distortion as a function of incidence angle is of the form

$$|\Delta\theta| = \cot\theta\ \Delta v/v \tag{42}$$

which shows that the most serious errors occur at low angles of incidence.

The problem of determining the true transform $P^2(\theta)R(\theta)$ from a finite segment $V'(z)$ of $V(z)$ is a common one in Fourier analysis and spectral estimation. Various techniques exist in the literature for extrapolating $V'(z)$ so that a more accurate determination of $P^2(\theta)R(\theta)$ can be made. Since $P^2(\theta)R(\theta)$ is a bandlimited function, the maximum spatial frequency being limited by the angular extent of the pupil function, $V(z)$ is analytic in the entire z axis [17]. In principle, an iterative algorithm proposed by Papoulis [18] can be used to improve the accuracy of the estimation of $P^2(\theta)R(\theta)$.

Conclusion

We have demonstrated that the reflectance function of a liquid–solid interface can be determined by inverting the corresponding complex $V(z)$ data from an acoustic microscope. This inversion technique represents a more complete approach to material characterization than previous $V(z)$-related work. The phase velocities of the various propagating modes in the solid medium can be obtained directly from the reflectance function. The effect of material loss can also be observed and quantified. Moreover, this measurement technique provides a means of gauging imaging performance of focused systems by directly measuring the pupil function illumination. In addition, there are useful practical applications in the area of thin-film characterization, and many interesting possibilities exist for more complex structures, such as multi-layered films. The nonparaxial formulation of the $V(z)$ integral is important in that it lays a sound theoretical foundation for the inversion measurement technique. The excellent agreement between the theoretically and experimentally obtained reflectance functions further supports the validity of the nonparaxial theory.

Although this work has been carried out and discussed in the context of acoustic microscopy, the validity and applicability of many of the underlying concepts extend to optical microscopy as well. Provided one can accurately measure the optical phase, which is not trivial but certainly realizable [22], the inversion algorithm described here can be used to obtain the optical reflectance function from the corresponding complex optical $V(z)$ function.

Acknowledgment

The authors would like to thank Dr. Simon Bennett and Dr. Ian Smith for the stimulating discussions related to this work.

Appendix

Auld and Kino [19]–[21], by using the reciprocity theorem, were able to determine the normalized reflected signal or reflection coefficient s_{11} from an object. The theory

for longitudinal waves in a liquid can be stated in the form

$$s_{11} = \frac{j\omega \int (u^i p - u p^i)\, n\, dS}{4P} \tag{A1}$$

where the integral is taken over the surface of the object, u is the displacement, and p is the pressure fields associated with an incident wave of temporal frequency ω. Here $\exp(j\omega t)$ time dependence is assumed. The superscript i denotes the incident or transmitted wave when the object is not present, and the unsuperscripted terms denote the total field at the obstacle. The parameter P is the power exciting the transducer for a given incident signal u^i, p^i.

The total fields can be written in the form

$$u = u^i + u^r \tag{A2}$$

$$p = p^i + p^r \tag{A3}$$

where the superscript r denotes the waves reflected from the object. Substituting (A2) and (A3) into (A1) yields

$$s_{11} = \frac{j\omega \int (u^i p^r - u^r p^i) n\, dS}{4P}. \tag{A4}$$

If the object is a semi-infinite plane normal to the z direction, s_{11} can be written in the normalized form

$$V(z) = \frac{\int (u_z^i\, p^r - u_z^r\, p^i)\, dS}{2 \int u_z^i\, p^{i^*}\, dS} \tag{A5}$$

where the asterisk denotes the complex conjugate. Finally it is convenient to write the pressure in terms of the potential. For a liquid with $u = \nabla\phi$, it can be shown that $p = j\omega\rho\phi$. Hence it follows that

$$V(z) = \frac{\int (u_z^i \phi^r - u_z^r \phi^i)\, dS}{2 \int u_z^i \phi^{i^*}\, dS} \tag{A6}$$

Note that for a perfect plane reflector located at the focal plane $z = 0$ of a lens, $\phi^r = \phi^i = \phi^{i^*}$, and $u_z^r = -u_z^i$; therefore $V(z) = 1$.

References

[1] A. Atalar, "An angular spectrum approach to contrast in reflection acoustic microscopy," *J. Appl. Phys.*, vol. 49, pp. 5130-5139, Oct. 1978.

[2] H. K. Wickramasinghe, "Contrast and imaging performance in the scanning acoustic microscope," *J. Appl. Phys.*, vol. 50, pp. 644-668, Feb. 1979.

[3] R. D. Weglein, "Metrology and imaging in the acoustic microscope," in *Scanned Image Microscopy*, E. A. Ash, Ed. London: Academic, 1980.

[4] J. Kushibiki and N. Chubachi, "Material characterization by line-focus-beam acoustic microscopy," *IEEE Trans. Sonics Ultrason.*, vol. SU-32, pp. 189-212, Mar. 1985.

[5] W. Parmon and H. L. Bertoni, "Ray interpretation of the material signature in the acoustic microscope," *Elect. Lett.*, vol. 15, pp. 684-686, 1979.

[6] A. Atalar, "A physical model for acoustic material signature," *J. Appl. Phys.*, vol.. 50, pp. 8237-8239, 1979.

[7] J. Kushibiki, A. Ohkubo, and N. Chubachi, "Acoustic anisotropy detection of materials by acoustic microscope using line-focus-beam," in *Proc. IEEE Ultrason. Symp.*, 1981, pp. 552-556.

[8] J. Kushibiki, K. Horii, and N. Chubachi, "FFT velocity measurement of multiple leaky waves by line-focus-beam acoustic microscope," in *Proc. IEEE Ultrason. Symp.*, 1983, pp. 637-640.

[9] H. L. Bertoni, "Ray-optical evaluation of $V(z)$ in the reflection acoustic microscope," *IEEE Trans. Sonics Ultrason.*, vol. SU-31, no. 2, pp. 105-116, Mar. 1984.

[10] P. M. Morse and H. Feshbach, *Method of Theoretical Physics*. New York: McGraw-Hill, 1953.

[11] I. J. Cox, D. K. Hamilton, and C. J. R. Sheppard, "Observation of optical signature of materials," *Appl. Phys. Lett.*, vol. 41, no. 7, pp. 604-606 Oct. 1982.

[12] J. A. Hildebrand, K. Liang, and S. D. Bennett, "Fourier-transform approach to material characterization with the acoustic microscope," *J. Appl. Phys.*, vol. 54, no. 12, pp. 7016-7019, Dec. 1983.

[13] K. Liang, S. D. Bennett, B. T. Khuri-Yakub, and G. S. Kino, "Precision phase measurements with the acoustic microscope," *IEEE Trans. Sonics Ultrason.*, vol. SU-32, pp. 000-000, Mar. 1985.

[14] G. Mott, "Reflection and refraction coefficients at a fluid-solid interface," *J. Acoust. Soc. Am.*, vol. 50, no. 3, pp. 819-829, 1971.

[15] F. L. Becker and R. L. Richardson, "Influence of material properties or Rayleigh critical-angle reflectivity," *J. Acoust. Soc. Am.*, vol. 51, no. 5, pp. 1609-1617, 1972.

[16] T. Bourbie, "Effects of attenuation on reflections," Ph.D. Thesis, Stanford University, Stanford, CA, April 1982.

[17] N. I. Akhiezer, *Theory of Approximations*. New York: Ungar, 1956.

[18] A. Papoulis, "A new algorithm in spectral analysis and band-limited extrapolation," *IEEE Trans. Circuits and Systems*, vol. CAS-22, no. 9, pp. 735-742 Sept. 1975.

[19] G. S. Kino and B. A. Auld, "Reciprocity theories for flaw analysis," ARPA/AFML annual review of progress in quantitative NDE, Cornell University, Ithaca, NY, 1977.

[20] B. A. Auld, "General electromechanical reciprocity relations applied to the calculation of elastic-wave scattering coefficients," in *Wave Motion*, vol. 1. Amsterdam: North-Holland, 1979, pp. 3-10.

[21] G. S. Kino, "The application of reciprocity theory to scattering of acoustic waves by flaws," *J. Appl. Phys.*, vol. 49, no. 6, pp. 3190-3199, June 1978.

[22] R. L. Jungerman, P. C. D. Hobbs, and G. S. Kino, "Phase sensitive scanning optical microscope," *Appl. Phys. Lett.*, vol. 45, no. 8, pp. 846-848, Oct. 1984.

[23] J. Fraser and C. Desilets, Precision Acoustic Devices, Inc., Palo Alto, CA, private communication.

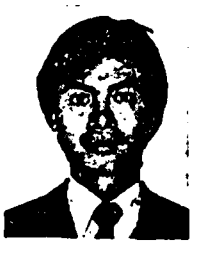

Kenneth K. Liang was born in Hong Kong in 1954. He received the B.S.E.E. degree from the University of Minnesota, Minneapolis, MN, in 1976.

He is currently finishing his doctoral dissertation in electrical engineering at Stanford University, Stanford, CA. His current interests are in the application of acoustic imaging techniques to nondestructive testing.

Gordon S. Kino (S'52-A'54-SM'63-F'66) was born in Melbourne, Australia on June 15, 1928. He received the B.Sc. and M.Sc. in mathematics at London University, England, and the Ph.D. in electrical engineering at Stanford University, Stanford, CA.

He is Professor of Electrical Engineering and Professor by Courtesy of Applied Physics at Stanford University. He has worked on microwave tubes, electron guns, plasmas, and the Gunn effect. His current interests are in microwave acoustics and acoustic and fiber optic techniques for medical instrumentation, nondestructive testing, and signal processing.

Dr. Kino was a Guggenheim Fellow in 1967 and is a Fellow of the American Physical Society, AAAS, and a member of the National Academy of Engineering.

Butrus T. Khuri-Yakub (S'70-M'76) was born in Beirut, Lebanon. He received the B.S. degree in 1970 from the American University of Beirut, the M.S. degree in 1972 from Dartmouth College, Hanover, NH, and the Ph.D. degree in 1975 from Stanford University, Stanford, CA, all in electrical engineering.

He joined the research staff at the E. L. Ginzton Laboratory of Stanford University in 1976 as a Research Associate. He was promoted to a Senior Research Associate in 1978, and to a Professor of Electrical Engineering (research) in 1982. His current research interests include thin-film deposition, surface acoustic wave devices, bulk-wave transducers and arrays, nondestructive evaluation of structural materials, acoustic imaging, and photo-acoustic interactions.

Dr. Khuri-Yakub is a member of the Acoustical Society of America.

THE EVALUATION OF V(z) IN A TYPE II REFLECTION MICROSCOPE

by

C-H. Chou and G. S. Kino

Preprint
G. L. Report No. 3964
November 1985

Submitted to IEEE Transactions on Sonics and Ultrasonics

AFOSR-84-0063B

Edward L. Ginzton Laboratory
W. W. Hansen Laboratories of Physics
Stanford University
Stanford, California 94305

THE EVALUATION OF V(z) IN A TYPE II REFLECTION MICROSCOPE

by

C-H. Chou and G. S. Kino

Edward L. Ginzton Laboratory
W. W. Hansen Laboratories of Physics
Stanford University
Stanford, California 94305

ABSTRACT

We have developed a more complete theory for the V(z) characteristic of an acoustic microscope. This theory is nonparaxial and treats the effect of finite ka , where a is the radius of the aperture. It explains well the asymmetry of the V(z) curve for a perfect reflector which has been observed experimentally and has been difficult to explain theoretically. The results obtained are also of importance to the scanning optical microscope.

INTRODUCTION

It has been known for some time that the output signal from a scanning acoustic microscope operating in a reflection mode varies rapidly with the distance of the focus z from the plane of the reflecting object. The variation of the parameter $V(z)$, the voltage output as a function of z, is the principal contrast mechanism of the scanning acoustic microscope when used to observe solid materials in a reflection mode.

The theory of this mechanism has been given by several authors,[1-3] and developed recently in a nonparaxial form by Liang and Kino.[4] Most of the attention has been devoted to the interaction of the specularly-reflected waves from a solid substrate with the Rayleigh waves that propagate along it. Recently, it has become important to consider the same type of $V(z)$ measurement for scanning optical microscopes. Surprisingly enough, there seems to have been relatively little attention paid to this phenomenon in the optical literature.[5] In this case, Rayleigh waves do not occur, but it would be useful to evaluate the resolution in the range direction (the z direction) of an optical microscope, and to understand the phenomenon fully, so that the device can be used for quantitative measurements of height.

The equivalent type of interaction in an acoustic microscope occurs, for instance, when a lead sample is examined in a water medium. In this case, the Rayleigh wave has too low a velocity to be excited. We and other authors have found that in such experiments the $V(z)$ plots do not obey the simple theory that has been developed. In particular, the $V(z)$ plots are asymmetric about the point $z = 0$ (focal point at the surface of the object), while most of the theories, with the exception of those due to Bertoni,[1,6] suggest that the function should be symmetric.

We have found that there are two basic causes of the asymmetry: phase variations at the lens surface, and the simplification of the theory to use either the paraxial approximation or asymptotic assumptions along with the use of the method of stationary phase. This is equivalent to assuming that $kr_0 \to \infty$, where r_0 is the radius of the lens aperture, and $k = 2\pi/\lambda$ is the propagation constant of the wave of wavelength λ. In this paper, we show how to modify the method of stationary phase to make a nonparaxial calculation for $V(z)$ and take account of the finite integration range, which is limited by the edge of the aperture. The results obtained agree well with experiment.

We first evaluate the cylindrical spatial frequency spectrum of the waves at the focal plane $A(k_r, 0)$, where k_r is the radial propagation constant and f_1 the distance of the focus from the plane of the lens aperture, as illustrated in Fig. 1. We then obtain $V(z)$ in the same manner as in reference 4. Second, we modify the analytical expression for $A(k_r, 0)$ by taking account of the integration limits, then use a modified form of the method of stationary phase, and compute $V(z)$ as before.

NUMERICAL COMPUTATION OF $A(k_r,0)$

We consider a spherical focused transducer and use scalar theory appropriate to acoustic waves in a liquid. This approach can be shown also to be an accurate one for calculating $V(z)$ for an optical beam. We use the notation shown in Fig. 1, taking the origin $z = 0$ at the focus. In the aperture plane $z = -f_1$, the potential field distribution in cylindrical coordinates is given by Liang et al[4] as:

$$\phi(r) = P(r) \frac{\exp\left[jk\sqrt{r^2 + f_1^2}\right]}{\sqrt{r^2 + f_1^2}} \qquad (1)$$

where $f_1 = \sqrt{f_0^2 - r_0^2}$, or $f_1 = f_0 \cos \theta_0$, f_0 is the focal length, r_0 is the radius of the transducer, θ_0 is the maximum half-angle subtended by the aperture at the focus; k is the wave number in water; and $P(r)$ is the pupil function of the lens. For the ideal lens, we assume that

$$\begin{aligned} P(r) &= 1 \qquad 0 < r < r_0 \\ P(r) &= 0 \qquad r > r_0 \end{aligned} \tag{2}$$

Since the field distribution is circularly symmetric, the cylindrical spatial frequency spectrum of $\phi(r)$ at the aperture plane P , denoted by $A(k_r, -f_1)$, can be expressed by its Hankel transform:

$$\begin{aligned} A(k_r, -f_1) &= \int_0^{\infty} P(r) \frac{\exp\left[jk\sqrt{r^2 + f_1^2}\right]}{\sqrt{r^2 + f_1^2}} J_0(k_r r)\, r\, dr \\ &= \int_0^{r_0} \frac{\exp\left[jk\sqrt{r^2 + f_1^2}\right]}{\sqrt{r^2 + f_1^2}} J_0(k_r r)\, r\, dr \end{aligned} \tag{3}$$

In the focal plane, it follows that

$$A(k_r, 0) = A(k_r, -f_1) \exp(-jkf_1) \tag{4}$$

where k_r is the radial wave number, and $k^2 = k_r^2 + k_z^2$, or $k_r = k \sin\theta$, $k_z = k \cos\theta$, and θ is the angle of the wave propagation direction to the z axis.

The parameter $A(k_r, 0)$ can be obtained by numerical integration. For this integration, the steps in k_r, $\Delta(k_r)$ must be chosen small enough in order to keep the phase variation of the integrand reasonably small over each step. Therefore, when kr_0 is very large (e.g., $kr_0 > 1000$), the computation time tends to be inordinately long.

The amplitude and the phase of the numerically-computed function in the focal plane $A(k_r, 0)$ are shown in Figs. 2a and 2b for an aperture radius $r_0 = 10.3$ mm , a focal length $f_0 = 16$ mm , frequency $f = 10.7$ MHz , and a wavelength $\lambda = 0.14$ mm with water as the propagation medium; this corresponds to a value of $kr_0 = 462$. For comparison, the dashed lines show the corresponding results obtained by using the asymptotic form of the Bessel function and the method of stationary phase to integrate Eq. (3).[4] This latter result can be expressed analytically as follows:

$$A(k_r,0) = \frac{jk}{k_z} = \frac{j}{\sqrt{1 - k_r^2/k^2}} \qquad k_r < k \sin \theta_0$$

$$A(k_r,0) = 0 \qquad k_r > k \sin \theta_0 \tag{5}$$

This simple expression predicts an average value of $A(k_r,0)$ both in amplitude and phase, but does not predict the rapid variations (the Fresnel ripple) of $A(k_r,0)$ with k_r . The simplifying approximation yields an expression for $V(z)$, which is symmetric around $z = 0$ because of the constant phase with k_r , and does not always agree with experiments.

A MORE ACCURATE ANALYTICAL EXPRESSION FOR $A(k_r,0)$

When $kr_0 > 1000$, the numerical integration of Eq. (3) is very time consuming. Therefore, it is advantageous to work out a more accurate analytical expression for $A(k_r,0)$ than that given by the direct application of the method of stationary phase. Following the analysis by Liang et al,[4] we use the asymptotic form of $J_0(k_r r)$ and obtain the approximate expression:

$$A(k_r, -f_1) = \int_0^{r_0} \frac{\exp[j\psi_1(r)]}{\sqrt{2\pi k_r r(r^2 + f_1^2)}}\, r\,dr \tag{6}$$

where

$$\psi_1(r) = k\sqrt{r^2 + f_1^2} - k_r r + \frac{\pi}{4}$$

Following the method of stationary phase, the main contribution to the integral in Eq. (6) comes from the region $\psi_1'(r) = 0$, or where

$$r' = \frac{k_r}{k_z} f_1 = f_1 \tan \theta \tag{7}$$

Therefore, $\psi_1(r)$ can be expanded in the region near r' as:

$$\psi_1(r) = \psi_1(r') + D(r - r')^2 \tag{8}$$

where

$$D = \frac{1}{2}\psi_1''(r') = \frac{1}{2}\frac{k^2 \cos^3 \theta}{kf_1} \tag{9}$$

It follows that

$$A(k_{r,} - f_1) = B(r') \frac{r' \exp [j \psi_1(r')]}{\sqrt{2\pi k_r r'(r'^2 + f_1^2)}} \tag{10}$$

where

$$B(r') = \int_0^{r_0} \exp [jD(r - r')^2 dr \tag{11}$$

In reference [4], following the standard approach to the method of stationary phase, the integration limits were taken from $-\infty$ to ∞, but this is

not a valid assumption for $k_r \to 0$ and $k_r/k \to \sin\theta_0$. Here we retain the limits of integration of r as 0 and r_0. Although the expansion of Eq. (8) is not accurate over the whole region, it is still adequate since the rapid phase variation of the integrand causes the main contribution to the integral still to come from the region where $D(r - r')^2$ is relatively small. Thus, we can evaluate Eq. (11) with finite limits and write

$$B(r') = \int_{-\sqrt{D}r'}^{0} \frac{1}{\sqrt{D}} \exp(jx^2)\, dx + \int_{0}^{\sqrt{D}(r_0 - r')} \frac{1}{\sqrt{D}} \exp(jx^2)\, dx$$

$$= \sqrt{\frac{\pi}{2D}}\, [C(X) + jS(X) + C(Y) + jS(Y)] \tag{12}$$

where $C(z)$ and $S(z)$ are the Fresnel integrals defined as

$$C(z) = \int_0^z \cos\left(\frac{\pi}{2} t^2\right) dt \tag{13}$$

$$S(z) = \int_0^z \sin\left(\frac{\pi}{2} t^2\right) dt \tag{14}$$

and

$$X = \sqrt{\frac{2D}{\pi}}\, r' = \sqrt{\frac{2 f_1 \cos\theta}{\lambda}}\, \sin\theta \tag{15}$$

$$Y = \sqrt{\frac{2D}{\pi}}\, (r_0 - r') = \sqrt{\frac{2f_1 \cos\theta}{\lambda}}\, \cos\theta\, (\tan\theta_0 - \tan\theta) \tag{16}$$

Therefore, it follows that

$$A(k_r, -f_1) = \frac{1}{\sqrt{2}\cos\theta}[C(X) + jS(X) + C(Y) + jS(Y)] \exp j[k_z f_1 + \pi/4] \quad (17)$$

In the focal plane, the complex amplitude of the cylindrical wave spectrum is

$$A(k_r,0) = \frac{1}{\sqrt{2}\cos\theta}[C(X) + jS(X) + C(Y) + jS(Y)] \exp\left(\frac{j\pi}{4}\right) \quad (18)$$

Figures 3a and 3b show the amplitude and phase of $A(k_r,0)$ in the focal plane predicted by Eq. (18) for the same case shown in Figs. 2a and 2b. In the region near $k_r/k = \sin\theta_0$, where it dominates $V(z)$, the result is similar to that obtained from the numerical integrations shown in Figs. 2a and 2b.

THE RESULTS FOR V(z)

Using our numerical computed and analytical results for $A(k_r,0)$ shown in Figs. 2 and 3, we have computed $V(z)$ the same way as that given in [4]. In Fig. 4a, we show the theoretically-predicted value of $V(z)$ for lead, obtained from the numerical calculation of $A(k_r,0)$. Figure 4b uses the more accurate analytical expression for $A(k_r,0)$ [Eq. (18)], and Fig. 4c uses the simple expression given in Eq. (5), as derived by Liang.[4] Fig. 4d shows the corrsponding experimental result. It is clear that the predictions given in this paper (Figs. 4a and 4b) agree with experiments carried out by Liang much better than the simpler theory given in ref. [4] (Fig. 4c).

Both Figs. 4a and 4b show very good agreement for the locations of the maxima and minima with the experimental data.

We believe that the remaining disagreement between the theoretical and experimental data of the $V(z)$ comes from the nonuniformity of the spherical

transducer (or lens) excitation, amplitude and phase weighting of the excitation of the transducer or lens. To show the effect, we tried Gaussian tapering of both the amplitude and the phase of the transducer output signal. Figures 5a and 5b show the tapering functions used and the corresponding V(z) for the same case as in Fig. 4a. Our reasonable guess for tapering yields results in Fig. 5b which agree even better with experiments.

CONCLUSION

This paper gives a better theoretical evaluation of V(z) in the reflection acoustic microscope by dealing with the evaluation of $A(k_r,0)$ more carefully. We have postulated that the remaining disagreement between the theoretical and experimental data is mainly due to the nonuniformity of the excitation of the lens (or spherical transducer) and shown that slight and reasonable changes in this excitation give still better agreement with experiments.

ACKNOWLEDGMENT

This work was was supported by the Air Force Office of Scientific Research under Contract No. AFOSR-84-0063B.

REFERENCES

1. H. L. Bertoni, "Ray Optical Evaluation of V(z) in the Reflection Acoustic Microscope," IEEE Trans. on Sonics and Ultrasonics SU-31 (2), 105-116 (March 1984).
2. A. Atalar, "An Angular Spectrum Approach to Contrast on Reflection Acoustic Microscopy," J. Appl. Phys. 49, 5130-5139 (October 1978).

3. R. D. Weglein, "Acoustic Microscopy Applied to SAW Dispersion ad Film Thickness Measurement," IEEE Trans. on Sonics and Ultrasonics SU-27, 82-86 (2 March 1980).

4. K. K. Liang, G. S. Kino, and B. T. Khuri-Yakub, "Material Characterization by the Inversion of V(z)," IEEE Trans. on Sonics and Ultrasonics SU-32 (2), 213-225 (March 1985).

5. J. Cox, D. K. Hamilton, and C. J. R. Sheppard, "Observation of Optical Signatures of Materials," Appl. Phys. Lett. 41 (7) (1 October 1982).

6. H. L. Bertoni and M. G. Somekh, "Ray-Optical Analysis of Spherical Focusing Transducers for Acoustic Microscopy," presented at the IEEE Ultrasonics Symposium, San Francisco, CA (October 1985).

FIGURE CAPTIONS

Fig. 1. Schematic of spherical focused transducer.

Fig. 2. Cylindrical spatial frequency spectrum of wave excited by a spherical focused transducer (r_0 = 10.3 mm , f_0 = 16 mm , λ = .14 mm) at focal plane.
(a) amplitude; (b) phase. Solid line: Predicted by numerical computation. Dashed line: Predicted by the simple expression in [4].

Fig. 3. Cylindrical spatial frequency spectrum of wave excited by the same focused transducer as in Fig. 2, at focal plane predicted by the more accurate analytical expression (Eq. 18). (a) amplitude; (b) phase.

Fig. 4. The comparison of the theoretical V(z) for lead by using A(k,0) shown in Figs. 2 and 3 and the experimental results. (a) A(k,0) corresponds to the solid line in Fig. 2. (b) A(k,0) corresponds to that in Fig. 3. (c) A(k,0) corresponds to the dashed line in Fig. 2.

Fig. 5. (a) Gaussian tapering function of transducer output signal.
(b) The corresponding V(z) for the same case as in Fig. 4a.

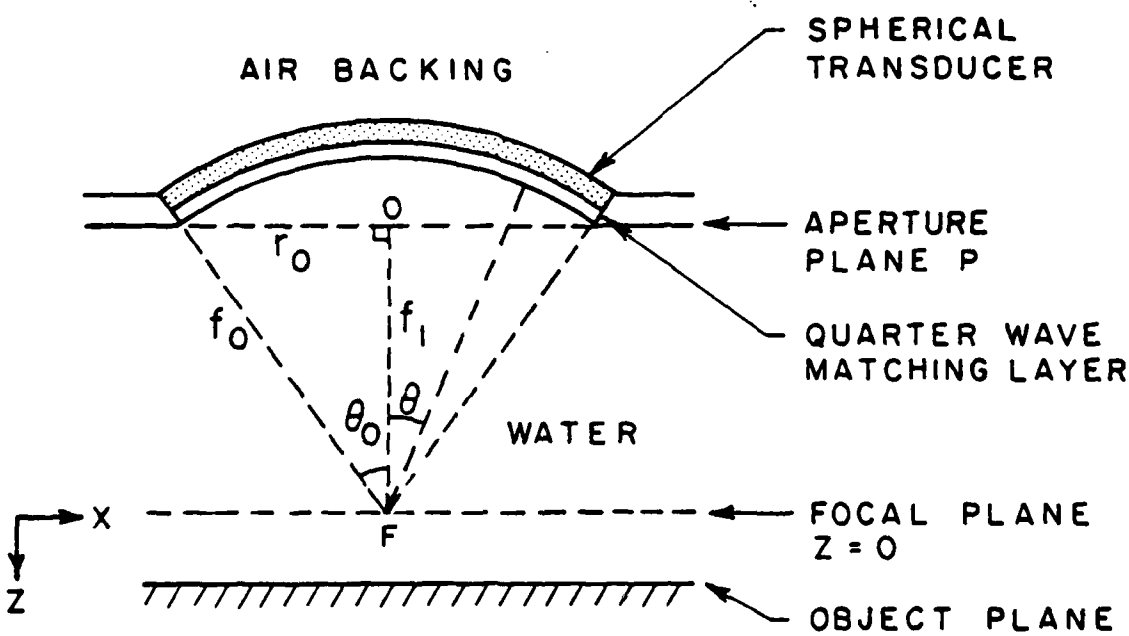
AIR BACKING
SPHERICAL TRANSDUCER
APERTURE PLANE P
QUARTER WAVE MATCHING LAYER
WATER
FOCAL PLANE Z = 0
OBJECT PLANE
O
F
X
Z
r_0
f_0
f_1
θ_0
θ

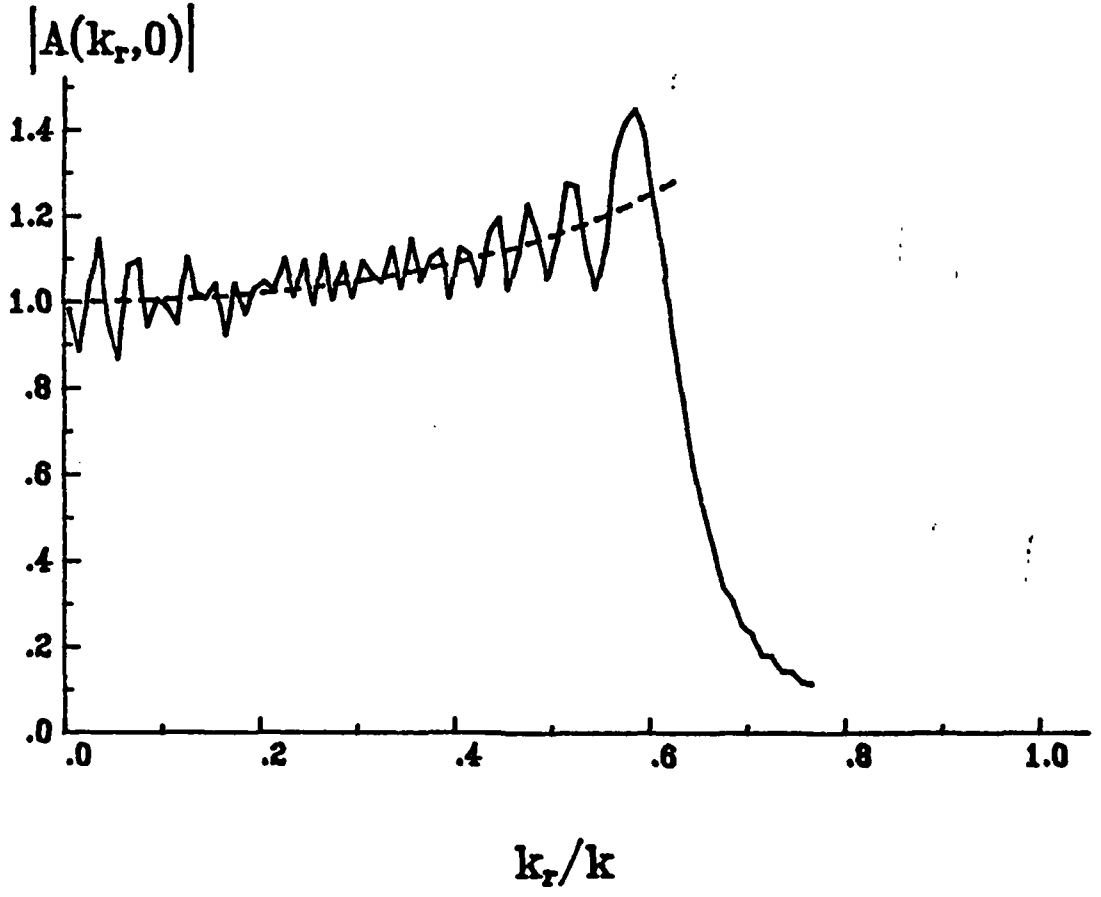

Fig. 2a

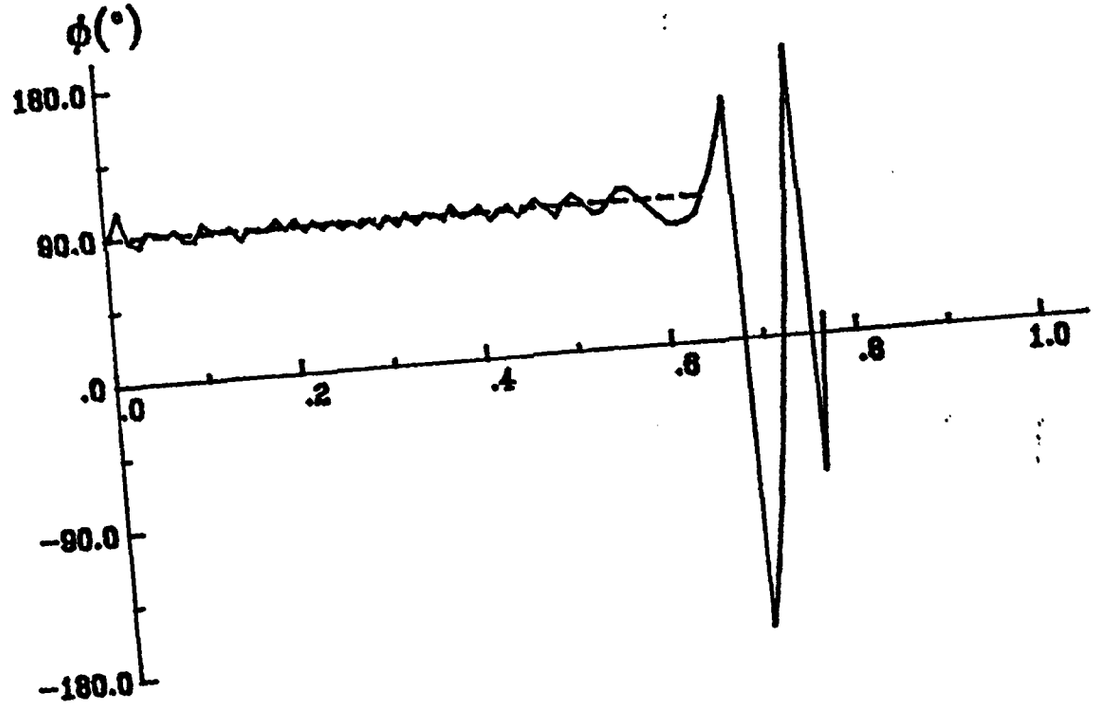

Fig. 2b

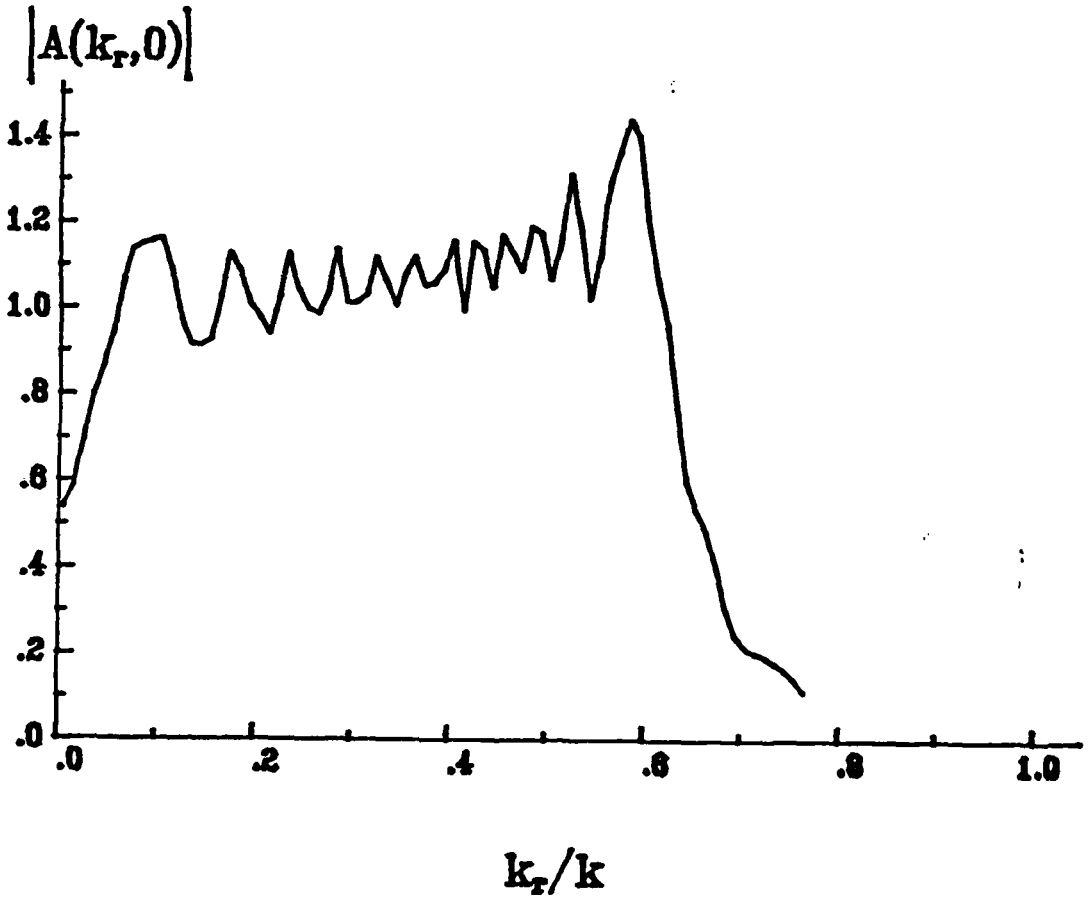

Fig. 3a

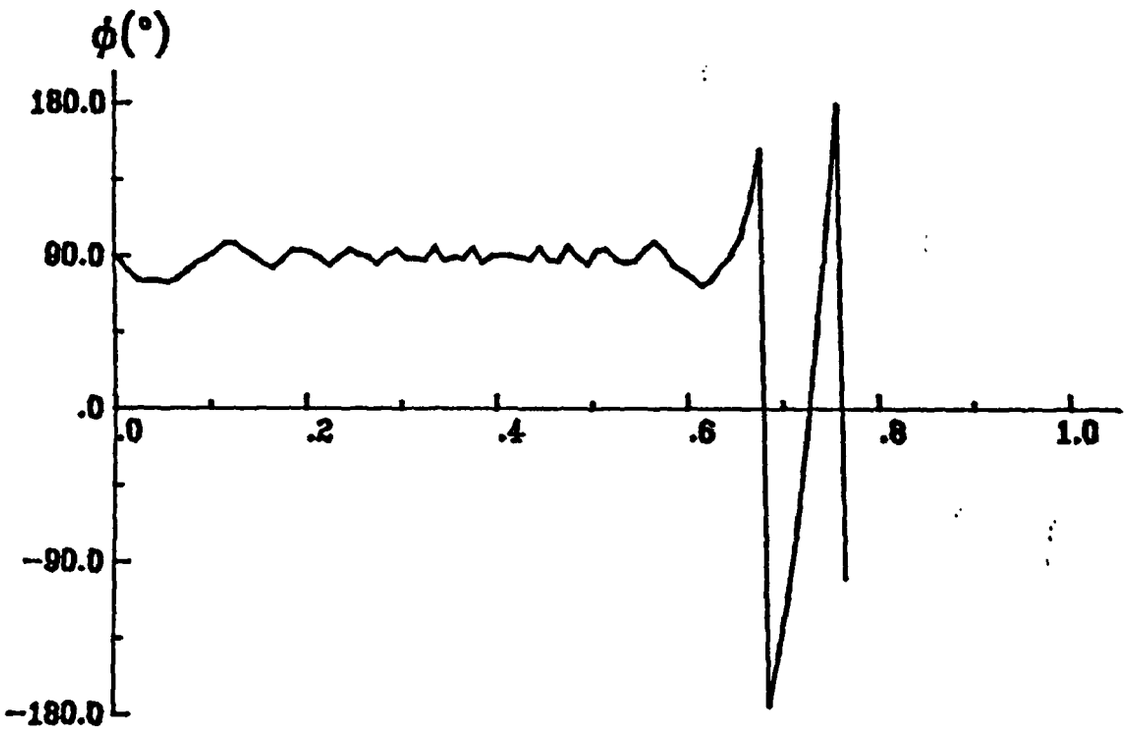

Fig. 3b

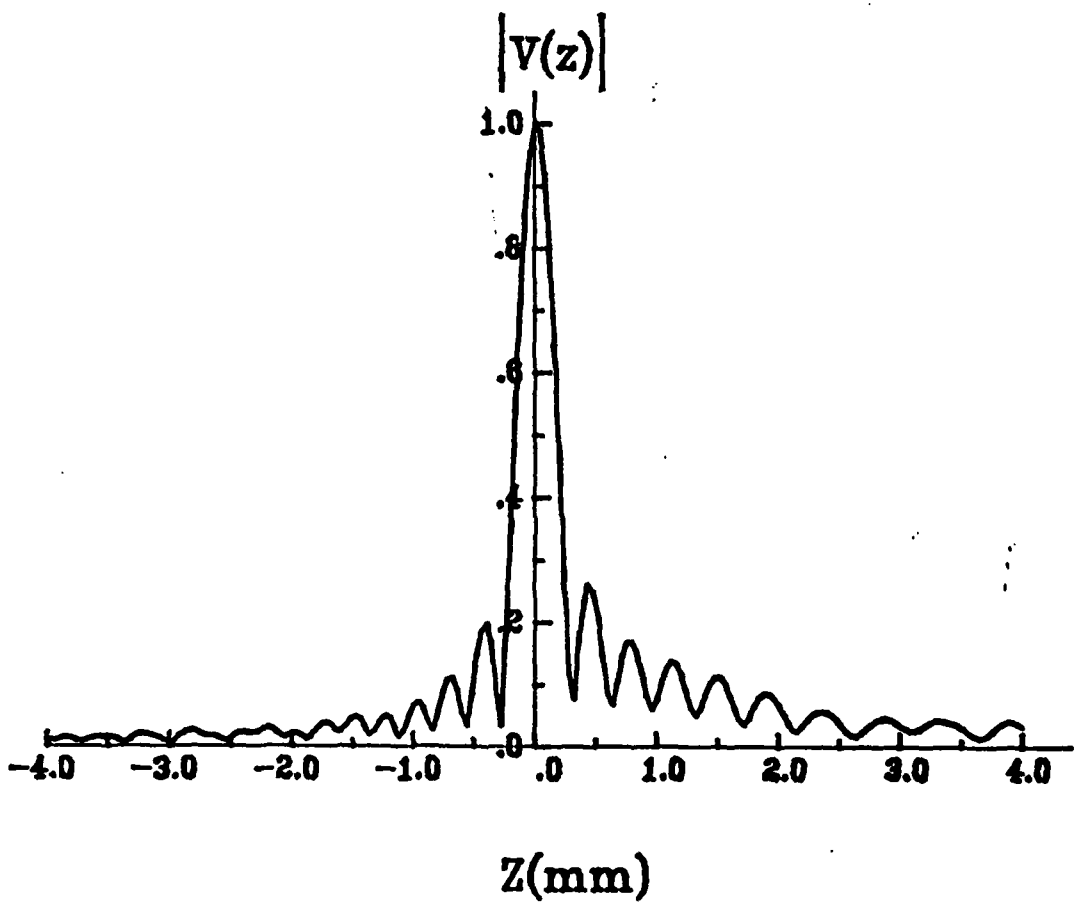

Fig. 4a

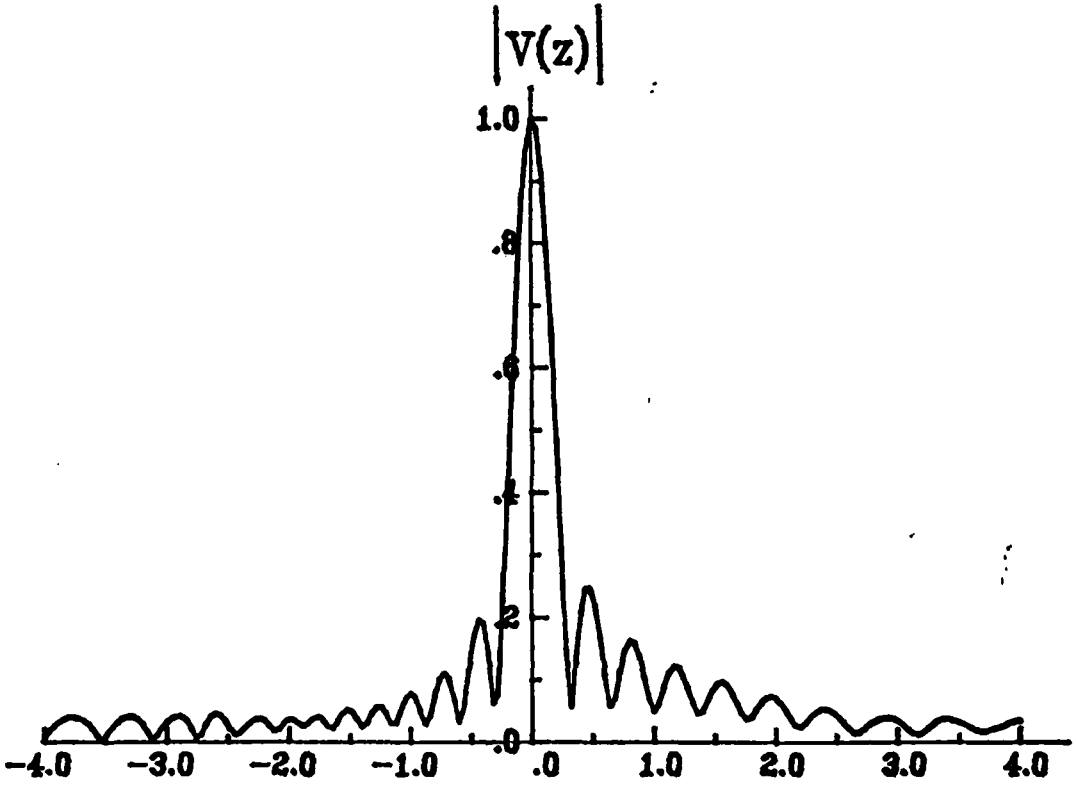

Fig. 4b

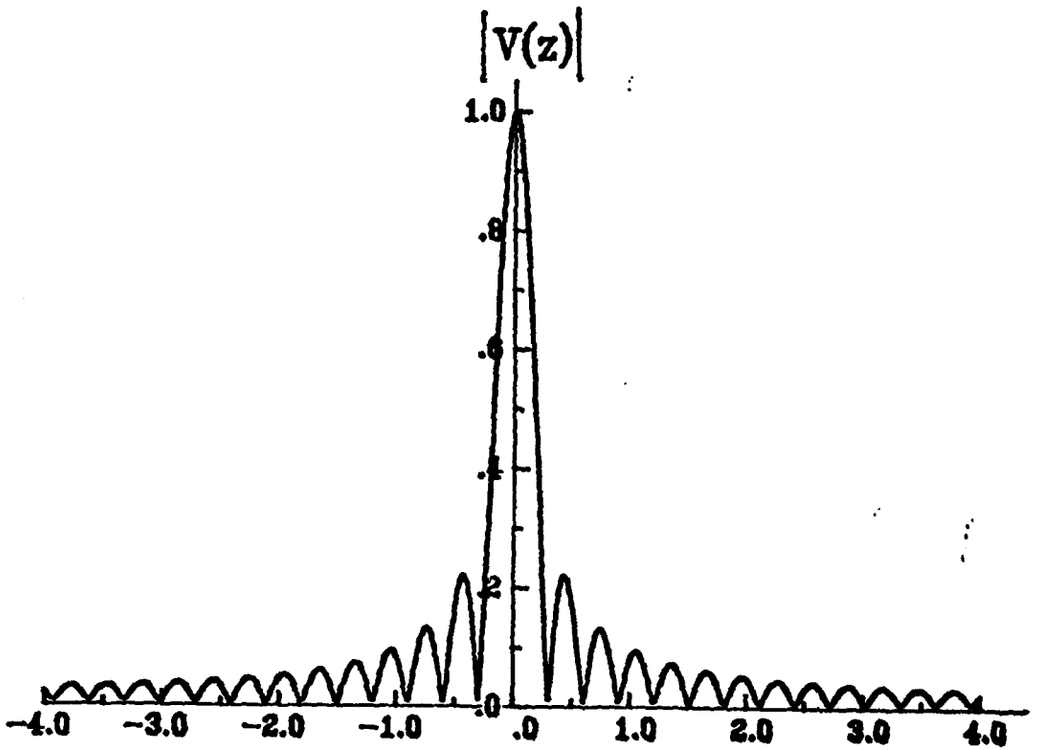

Fig. 4c

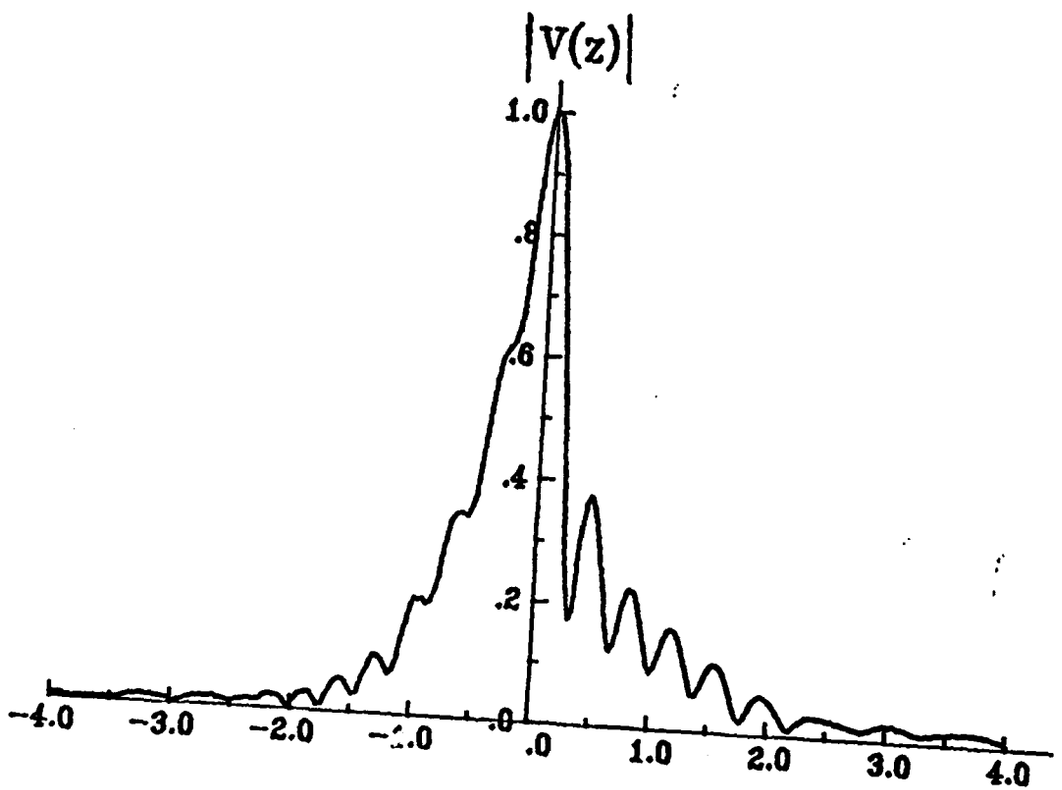

Fig. 4d

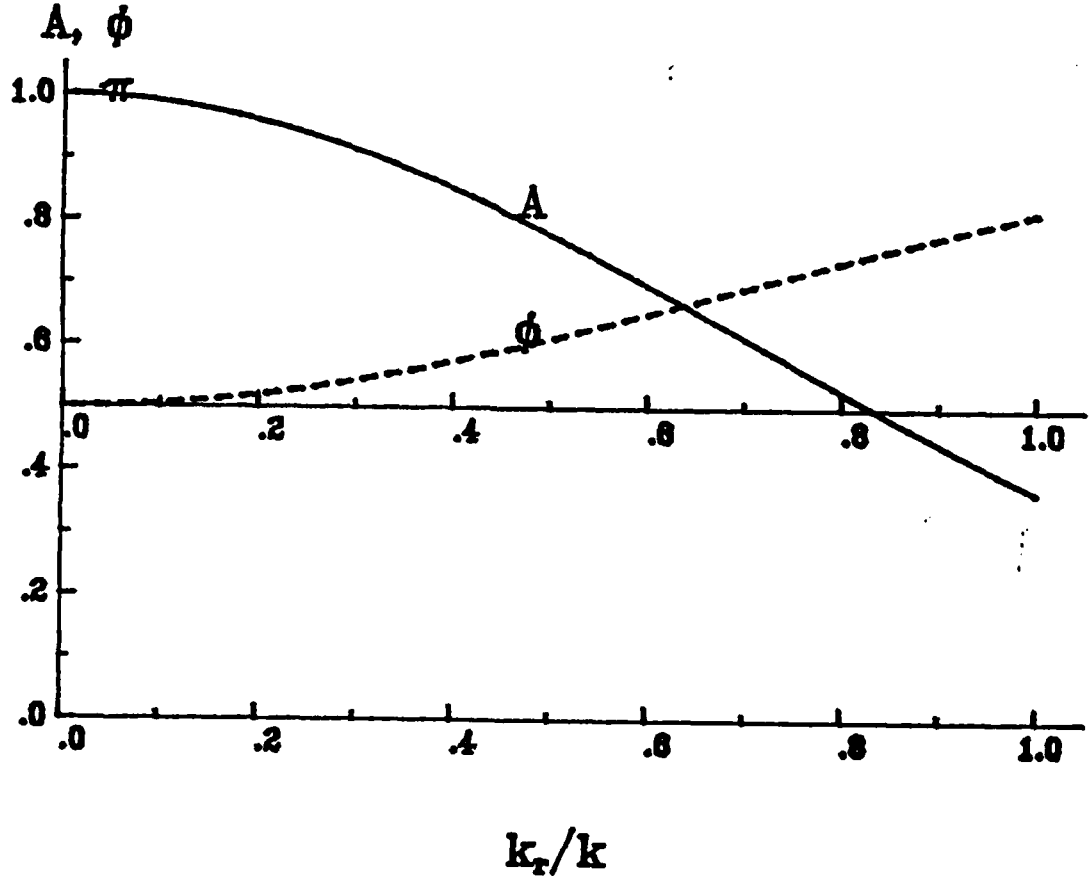

Fig. 5a

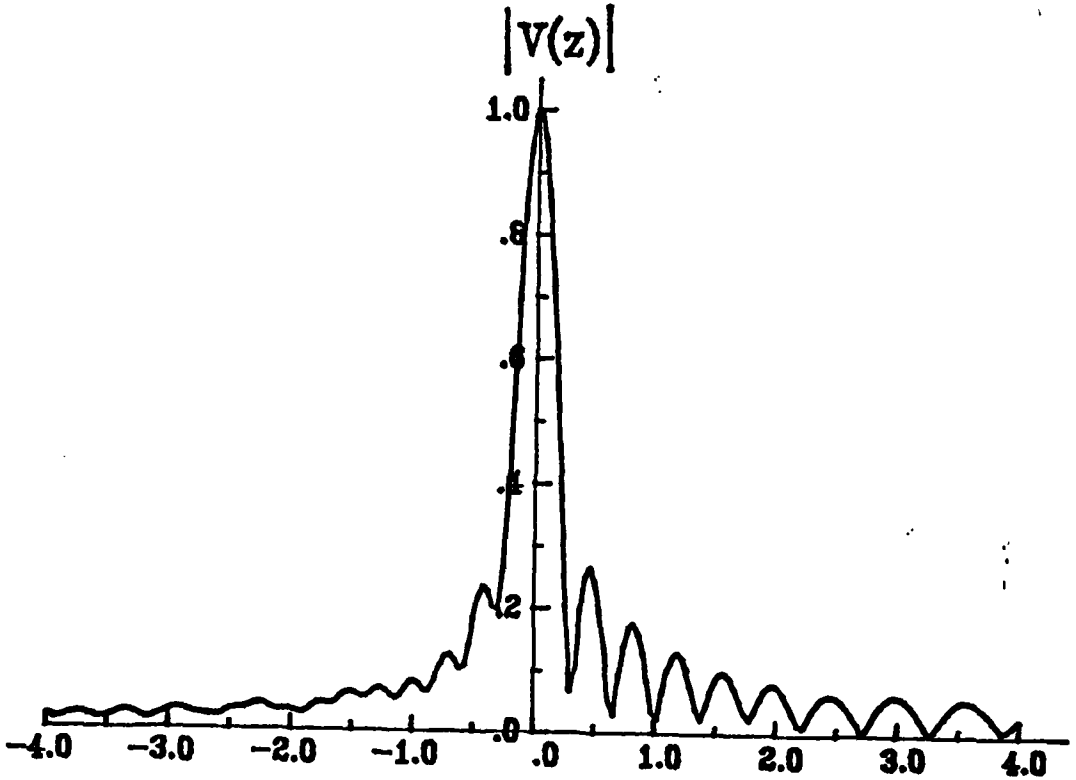

Fig. 5b

END

10-86

DTIC